LBNE Case Study Report

Liquid Argon TPC Far Detector

The LBNE Science Collaboration

DRAFT Version 1.4

November 1, 2011

Contents

1 Executive Summary: Liquid Argon TPC Far Detector for LBNE

The Long-Baseline Neutrino Experiment (LBNE) represents a unique and compelling program for the exploration of key questions at the forefront of particle physics. Chief among the discovery opportunities it will enable are searches for violations of CP symmetry in neutrino oscillations, searches for nucleon decay signatures, and studies of neutrino bursts from locally occurring supernovae. To fulfill these and other goals as a world-class facility, LBNE relies on three distinct components: (1) a new intense neutrino source and Near Detector facility, (2) an underground facility located at a distance and depth satisfying oscillation and other physics requirements, and (3) a large Far Detector housed in the underground facility.

The properties and capabilities of the Far Detector are critical for pursuing the transformative physics goals mentioned above. Long discussed as an ideal detector technology for low-rate experiments, the Liquid Argon Time Projection Chamber (LArTPC) concept has advanced in recent years, thanks to vigorous R&D efforts in Europe, Japan and the United States that have now reached a culmination. With the development of conceptual designs for large-scale detector modules, the LArTPC is a "game-changer" for LBNE:

- The millimeter-scale measurement of position and energy deposition on 3-D space point coordinates along the full length of charged-particle trajectories underly the exquisite event reconstruction and calorimetric capabilities of the LArTPC. Signatures from processes of interest, such as inclusive ν_e interactions and exclusive proton decay channels, can be studied in detail, and even pernicious backgrounds can be identified and rejected.

- With the combination of high efficiency and low background rates, significantly less target mass is needed relative to other detector technologies. In addition, the highly localized nature of signatures for signal and background processes within the large LArTPC volume enables active rejection of cosmogenic backgrounds with low loss of fiducial mass times livetime, even at relatively shallow sites. Both considerations lead to lower costs for comparable physics sensitivities.

- With an arrangement of modular TPC drift cells within two cyrostats, the LAr TPC design for LBNE is scalable. The construction of cost effective larger modules for future

1

additions is possible.

- Together, the unique strengths of exceptional detector resolution and calorimetry, large target mass, and underground location also open the possibility of discovery of entirely unanticipated phenomena. Nature occasionally rewards versatile detectors that happen to be well positioned to observe unexpected signatures of new physics.

This document presents an abbreviated description of the LBNE LAr TPC Far Detector, with a focus on aspects that bear on detector operations and science capabilities. The key findings are:

- A detector configuration consisting of two 16-kt fiducial LAr TPC modules satisfies the science goal for oscillation physics sensitivity at the level of "two 100-kt (fiducial) Water Cherenkov Module equivalents". Relative sensitivities to other physics goals vary.

- The Homestake Mine, at a distance of 1290 km from Fermilab, provides an optimal baseline for the oscillation physics goals.

- The 1 kton prototype, LAr1, will provide the assurance that detector sub-systems are integrated and will demonstrate that the performance requirements can be achieved by tracking cosmic rays.

- The detector would perform well for proton decay at a depth of at least 160 meters below the surface. The design of the veto system that enables proton decay studies at this depth is based on the more conservative model of the cosmic ray spallation background. Cosmic ray data acquired in LAr1 can be used to validate the models, reduce the background uncertainty and potentially the cost of the veto system.

- The use of two detectors in two cryostats greatly mitigates commissioning risks, allowing the qualification of both cryostats and one detector without relying on temporary LAr storage. Nine months of operating experience with one detector will be obtained before the second detector is filled with LAr.

- The engineering challenge of containing large volumes of ultra-pure LAr has been met by the use of a membrane cryostat technology that has 1600 tank-years of service in more demanding applications. A major concern has been eliminated by demonstrating the ability to achieve a hard vacuum in a membrane tank without altering the industrial design.

- The detector energy sensitivity will be ∼0.5 MeV; the endpoint energy of Ar^{39} decays. An energy threshold of 5 - 10 MeV is feasible. System noise will be monitored and mitigated during detector installation ensuring that the energy threshold requirement is met before the cryostat is filled with LAr.

- Finally, all R&D to support the LAr TPC conceptual design has been completed - technically sound conceptual designs exist for all elements of the detector.

Table 1–1 provides a snapshot of the primary physics program, sensitivities and corresponding detector location/depth requirements. Additional physics measurements are possible; these are also described in the report.

Parameter	Sensitivity	Depth Requirement	Comment/Assumption
Primary Objective 1.1. Beam measurements using ν_e appearance $\mathbf{5+\bar{5}}$ years livetime			
$\sin^2 2\theta_{13}$	$> 0.008\ (3\sigma)$	minimal	all δ_{CP}
Mass Hierarchy	3σ for $\sin^2 2\theta_{13} > 0.05$	minimal	all δ_{CP}
CP Violation	3σ discovery for 50% δ_{CP} range	minimal	$\sin^2 2\theta_{13} > 0.03$
Primary Objective 1.2 Beam measurements ν_μ disappearance $\mathbf{5+\bar{5}}$ years livetime			
$\delta(\Delta m^2_{32})\ (\nu/\bar{\nu})$	$\pm 0.016/0.025 \times 10^{-3}\,eV^2$	minimal	1σ, $\sin^2 2\theta_{23} = 1.0$
$\delta(\sin^2 2\theta_{23})\ (\nu/\bar{\nu})$	$\pm 0.006/0.009$	minimal	1σ, $\sin^2 2\theta_{23} = 1.0$
Primary Objective 1.3. Nucleon Decay, 33 kt, 10 years livetime			
$\tau/BR(p \to K^+\nu)$	0.4×10^{35} years	160m	6–7 $\times$ beyond exp. SK limit
$\tau/BR(p \to e^+\pi^0)$	0.2×10^{35} years	16m	probably not competitive
Primary Objective 1.4. Supernova Burst, 33 kt, 10 years livetime			
Neutrino Yield	3,000 events at 10 kpc	160m	

Table 1–1: Summary of physics sensitivities for primary physics objectives with the LAr40 Far Detector configuration described in this report.

2 Introduction

2.1 Goals of this Case Study Report

A system of large Liquid Argon TPC modules has been proposed to serve as the Far Detector for the Long-Baseline Neutrino Experiment (LBNE). The reference design for this Far Detector option calls for a liquid argon fiducial (active) mass of 33 (39) kilotons housed in two detector vessels located at the 800-foot level (800L) of the Homestake mine. We refer to this configuration as "LAr40". This LBNE Case Study Report aims to describe aspects of the LAr40 reference design that bear on its scientific capabilities.

Because of the fine granularity and excellent event reconstruction capabilities of LAr TPC detectors, a compact design is possible, with less neutrino target mass than is required by other detector technologies for comparable physics reach. The performance characteristics of these detectors also provide input with regard to choice of siting conditions (geographic location and depth), and these aspects are also discussed in this report. These considerations point to several practical benefits of the LAr TPC technology as a choice for LBNE. From the standpoint of scientific capability, in addition to the quantitative discussions presented here, it is also emphasized that the overall quality of event information provided by the LAr TPC adds value, especially when considering studies involving rare processes such as nucleon decay.

LAr40 utilizes the same technology successfully used in ICARUS and ArgoNeuT - single phase LAr TPC. At the same time, construction and operation of LAr40 represents a significant scale-up relative to current planned and operating LAr TPC's. At this point in time, all R&D has been completed - conceptual designs exist for all elements of LAr40. The elements of the development plan described in chapter 7 can be characterized as preliminary design activities.

The overall goal of this report is to (1) highlight the physics capabilities of the LAr40 Far Detector, (2) describe the mechanisms for acquiring, analyzing and understanding the data, and (3) describe the means for managing the scale-up risks.

2.2   Physics Goals of the LArTPC Far Detector

The proposed LArTPC Far Detector configuration for LBNE offers especially strong capabilities for the study of neutrino oscillation physics. This includes the primary goal of precisely measuring the parameters governing $\nu_\mu \rightarrow \nu_e$ oscillations via detection of ν_e and $\bar{\nu}_e$ interactions in the LBNE ν_μ and $\bar{\nu}_\mu$ beams. Considerable gains in sensitivity to θ_{13}, the CP-odd phase δ, and especially the neutrino mass hierarchy (characterized as the sign of the squared mass difference Δm_{32}^2) relative to current and near-future experiments are achievable with LAr40 at Homestake. The physics questions to be addressed by these measurements are profound and far-reaching. Observing CP-violating effects, the most striking of which would be an asymmetry between $\nu_\mu \rightarrow \nu_e$ and $\bar{\nu}_\mu \rightarrow \bar{\nu}_e$ oscillation rates, is a key step toward establishing lepto-genesis as a viable scenario for generation of the baryon asymmetry of the universe. Resolving the mass hierarchy ambiguity will have dramatic implications, both for other experimental programs such as the search for neutrino-less double beta decay as well as for our basic understanding of fermion masses and mixing.

Additionally, the high statistics and excellent resolution/background-rejection capabilities of LAr40 will permit detailed study of ν_μ disappearance parameters. Most notably, θ_{23} is observed by several experiments to be consistent with maximal mixing (45°). Either outcome – placing a tighter lower bound on $\sin^2 2\theta_{23}$, or observing a deviation from unity would constitute an exciting result.

While the main focus of LBNE is neutrino oscillation phenomena, the overall physics program becomes much broader with the exploitation of opportunities generated by placing a large detector underground. LAr40 is uniquely sensitive to a number of nucleon decay channels, satisfying another primary objective of LBNE. Notably, it will make a qualitative impact on the SUSY-favored mode $p \rightarrow \nu K^+$ within the first three years of running. Rounding out the list of primary LBNE objectives, a core-collapse supernova at a distance of 10 kpc will result in several thousand detectable neutrinos in LAr40, permitting detailed studies of questions in particle physics, astrophysics and cosmology.

LAr40 will also have interesting capabilities with regard to studies of atmospheric neutrinos, searches for slow-moving magnetic monopoles, and other physics goals comprising a secondary tier within the LBNE program.

In summary, LAr40 will cover all of the primary objectives of LBNE. With the unprecedented combination of large mass, underground location, and exceptional performance characteristics envisioned for LAr40, the most interesting results may well arise from the observation of unexpected phenomena – much in the same way that the discovery of neutrino oscillations originated with detectors that were designed to search for proton decay or study how the sun burns.

3 Detector Reference Design

3.1 Overview and General Layout

The basic components of the liquid argon detector include a cryostat and associated cryogenic system. A time projection chamber (TPC) and readout electronics are housed in the cryostat. The cryostat contains the liquid argon target material and the cryogenic system keeps the liquid argon at a cryogenic temperature of 89K, and maintains the required purity through pump and filter system. A uniform electric field is created within the TPC volume between cathode planes and anode wire planes. Charged particles passing through the TPC release ionization electrons that drift to the anode wires. The bias voltage is set on the anode plane wires so that ionization electrons drift between the first several (induction) planes and is collected on the last (collection) plane. Readout electronics amplify and continuously digitize the induced waveforms on the sensing wires at several MHz, and transmit these data to the DAQ system for analysis. The wire planes are oriented at different angles allowing a 3D reconstruction of the particle trajectories. In addition to these basic components, a muon veto system and a photon detection system are also included in the reference design to enable the LAr40 to study proton decay and be sensitive to galactic supernova neutrinos at a moderate depth.

The LAr40 reference design detector system consists of two cryostats in a single cavern, oriented along the beam direction, and located at the 800 level of the Homestake mine. Each cryostat contains one TPC with a fiducial mass of 16.3kt (active mass of 20kt). Figures 3–1, 3–2 and 3–3 shows the proposed layout of the detector cavern at the 800L on the Homestake site. The layout includes drive-in access via the Kirk Road portal and a tie-in to the existing facility for alternate egress or access. Although some elements of the design are specific to the Homestake site, the general LAr40 design is site-neutral and to a large extent depth-neutral.

The decision to site the detector at the 800L was based on a cost comparison with a 4850L site. The depth decision is being reconsidered since the basis for the cost comparison has changed. This issue as described in Chapter 6.

7
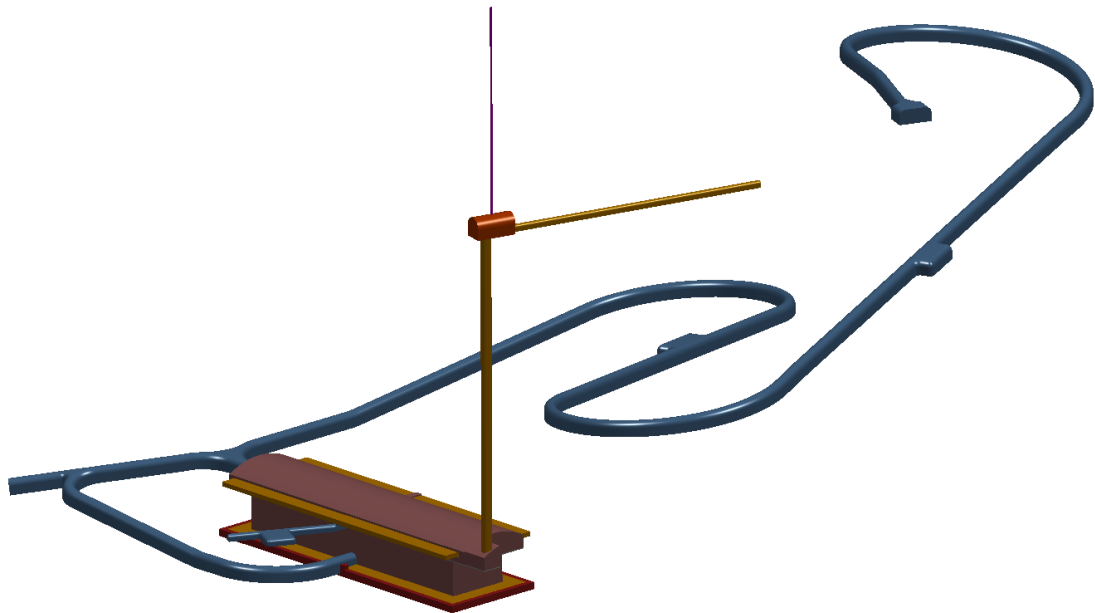
Figure 3–1: Access to the LAr40 cavern is through a 1.2km decline tunnel that reaches the surface in the Kirk valley at the 300L (North Portal). Two bump-outs on the tunnel will house areas of refuge. The decline tunnel enters the cavern at the floor level and at the lower veto level. A small secondary egress tunnel extends to the existing 800L drifts. Cryogenic piping is routed through a vertical shaft that enters a small enclosure at the 300L and then through a horizontal drift to the South Portal where the cryogenic plant is located. The small vertical shaft above the small enclosure contains an argon gas vent line.
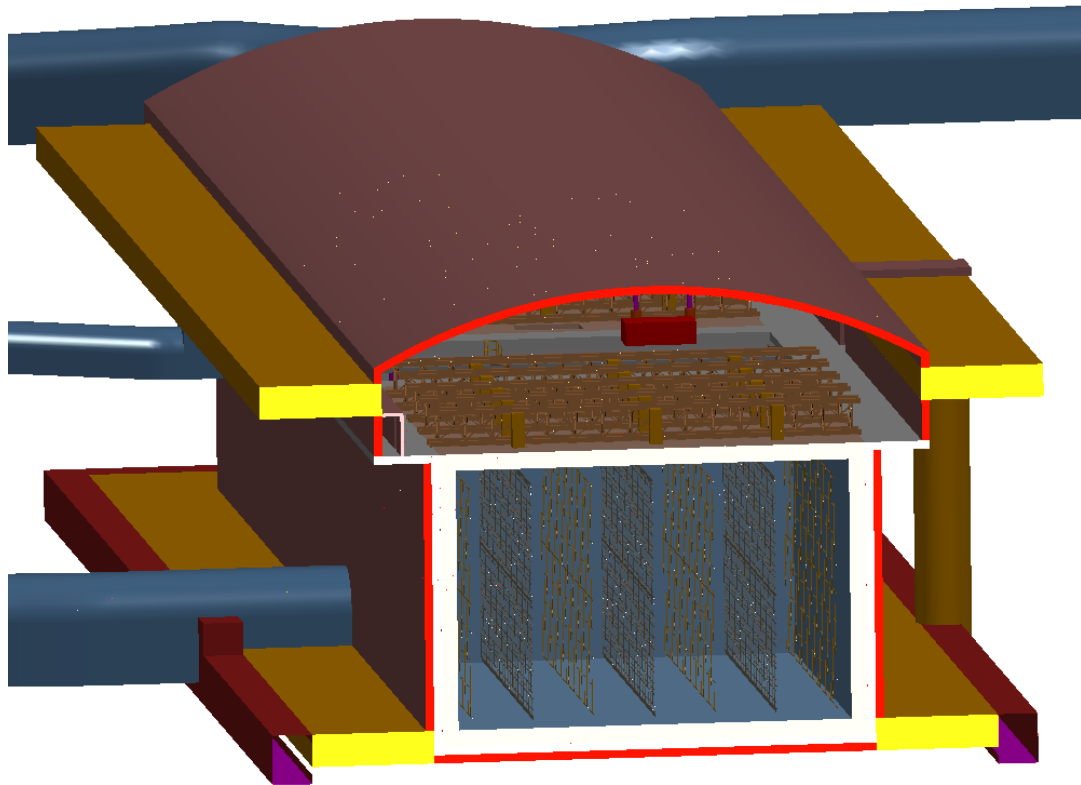
Figure 3–2: Detector configuration within the cavern. The TPC is located within a membrane cryostat, shown in white. The interior dimensions of the cryostat are 24m wide x 16m high. The TPC consists of three transverse APA rows, shown in blue, and four transverse CPA rows, shown in brown. The roof of the cryostat consists of steel plate supported by a series of trusses that span the cryostat pit. Upper and lower level veto galleries are shown in yellow. The veto galleries are excavated spaces filled with concrete. Steel veto tubes are embedded in the concrete. Personnel access to the lower level veto gallery is made via the decline tunnel, shown in blue on the left, or via the upper level veto gallery by a stairway in the shaft shown in dark yellow on the right. The upper level veto tubes, not shown, will extend over the top of the detector.
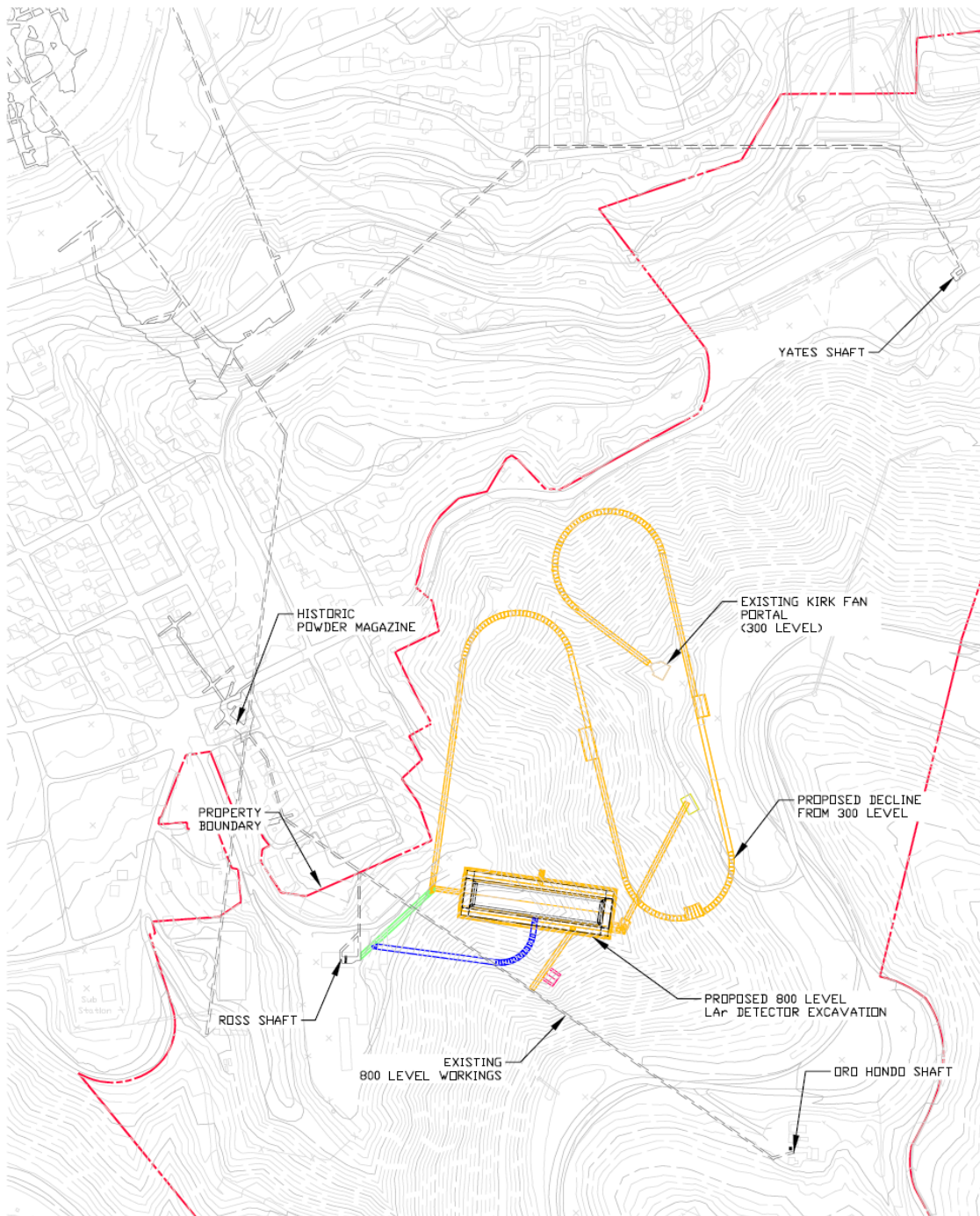
Figure 3–3: Local layout of the LAr40 cavern at the selected location on the 800L Homestake campus, with access shown.

3.2   Design for Scalability

The design of the LAr TPC described here has been developed and refined over the past 3 years. The starting point was the ICARUS T600 system, and the process was informed and guided by the experience with small LArTPC's in the US, particularly ArgoNeuT, the development of designs for MicroBooNE, and by the success of the ATLAS LAr calorimetry. The LAr TPC detector concept described in detail in this chapter is the result of an effort to assemble every major part of the detector from small, independent, elements (modules) which can be arrayed to relatively unrestricted degree in any dimension to form the entire assembly within a cryostat of any reasonable size and in which each of the elements (modules) provides an independent mechanical structure to support the sub-elements it contains. To a large extent, scaling from detector volumes containing from a few to several hundred of such modules should be straightforward with small and predictable risk.

The scalability depends on finding optimal solutions in five areas of the LAr TPC detector technology: cavern construction, cryostat construction, LAr purification, sub-system modularity and electronics readout. These solutions are described in the follow sub-sections.

### 3.2.1   Cavern Construction

The cavern span and volume chosen in this design are in a range that is well understood, requires no scaling from existing construction, and is not far from the size and geometry for minimum cost per unit excavated volume. This minimizes cost and time for cavern construction. The optimum design proposes two separated 20kt cryostats in one cavern. Any scaling to larger volumes would scale the number of caverns.

3.2.2   Cryostat Construction

The cryostat construction uses commercial stainless steel membrane technology engineered and produced by industry and widely deployed in liquefied natural gas tanker ships and tanks. It is an inherently clean, high vacuum technology with passive insulation. Sizes of LNG tanker cryostats are typically twice that contemplated here; numbers in service are approximately 50 times larger. The unit of construction is a panel 1m x 3m or 3m x 8m consisting of foam insulation containing a secondary containment barrier and a primary containment liner of 1.2mm or 2mm stainless steel sheet. These units are tiled to form a cryostat inside any reasonably smooth, reasonably rectilinear supporting volume, such as the hold of a ship or a cavern lined with poured concrete. Since these membrane cryostats are used to store LNG, used as fuel, they are known to have no leaks sufficient to cause explosion hazards, however LNG storage does not require the purity levels needed for a LAr TPC.

The insulation space behind the primary membrane is typically purged with nitrogen gas in LNG storage tanks. The insulation space in the LAr40 cryostats will be purged with argon gas so that even if a microscopic leak evades detection and repair, no contaminants will enter the cryostat. The standard leak testing methods used in the LNG industry are several orders of magnitude more sensitive than required ($\sim$10^{-5} atm-cc/sec) to detect a leak that could compromise the argon purity, even if the insulation space were filled with pure oxygen:

- Introducing helium into the insulation space and sniffing the welds inside the cryostat. The sensitivity of this test is 5x10^{-6} atm-cc/s

- Spraying the welds with a paint that changes color when exposed to ammonia. Ammonia vapor is introduced into the insulation for one or more days. This is an ASTM standard test with a sensitivity of 1x10^{-7} atm-cc/s.

A 35 ton membrane cryostat prototype will operate in 2012 to validate the use of the membrane cryostat for high purity operation.

3.2.3   LAr Purification

The purification of LAr is accomplished with standard industrial equipment, using molecular sieves and chemically reducing materials, which are scalable within the contemplated range to accommodate the estimated irreducible material outgassing from warm materials in the vapor space above the liquid argon. Since outgassing rates scale with surface area and impurity concentrations scale with volume, volumetric flow through the purifier should scale as the 2/3 power of the detector volume. Since argon is an inert gas, there are no chemical effects to consider in scaling to large volumes. Extensive properties (such as electron and light attenuation) do not increase with total detector volume, since each fixed size TPC module, as described below, is an independent detector.

3.2.4   Sub-system Modularity

The units of construction of the active detector are anode plane assemblies (APAs), cathode plane assemblies (CPAs), and field cage panels. These are modular elements of a size optimized so as to simplify the manufacture, simplify commercial transport, and facilitate handling and the assembly in the detector cryostat. These elements are assembled inside the cryostat into TPC modules (TPMs). Each modular element is independent of the others; only the number of elements is scaled to instrument the total detector volume. Each element will be tested in LN (or LAr) after manufacture, again at the detector site before installation, and finally will be monitored continuously to detect any failures due to damage occurring during installation. The volume of each TPC module is in a range that is well developed and understood at present: it is about 0.5 times that of the ICARUS T300 unit and 1.4 times that of the MicroBooNE TPC.

3.2.5 Electronics Readout

The entire electronic signal processing chain is located at the sense wires in the LAr (hence "cold electronics"). This removes any constraints on how the TPC modular units can be sized and arrayed, removes constraints on detector scalability, and enhances the reliability of the detector at any scale. Since charge sensing is done at the sense wires, there is no increase in charge noise that would occur with the capacitance of long cables connecting sense wires to electronics outside the cryostat: the resolution for sense wires deep within the cryostat is as good as for sense wires near the periphery. All signal feedthroughs can then be placed at the top of the cryostat, where they are easily installed, are always accessible, are at low hydrostatic pressure, and pose no risk of LAr leakage. The cold electronic system will include digitization, buffering, and a high level of digital output multiplexing (ranging from 1/128 to 1/1024). Output data links will include redundancy to eliminate the effect of any single point failure. The multiplexing will result in a large reduction in the number of feedthroughs and cable connections that must be made during installation, minimizing installation complexity, signal interconnect failures and cryostat leakage, which otherwise would grow to become dominant risks in a very large system. Perhaps the most significant benefit of local digital multiplexing is the reduction that it offers in the volume of cable (the "cable plant") inside the cryostat. Routing many cables through the liquid would create inactive volumes and complicate the assembly. Most significantly, the reduction of the cable plant in the gas ullage reduces correspondingly the outgassing of electronegative impurities, the primary source being water, into the LAr. It is accepted that in a stainless steel lined cryostat as described above, cable outgassing is the dominant source of impurities.

Sixteen channels of the electronic signal processing chain will be fabricated on one ASIC, eight ASICs will be mounted on a single motherboard, and 20 motherboards will process all of the signals for one APA. Each channel is independent of the others except for programming registers, common power supply lines, and a common output multiplexer and transmission line. Programming logic will be designed to fail in a state that leaves the channel functioning in a default running mode. Common power supply and output lines and the common multiplexer can be replicated to reduce a single point failure from causing the loss of an entire APA. However, it should be noted that the failure of a single APA reduces the efficiency of the 20kt LAr TPC by 0.1%. The ASICs have been designed to make the performance of the electronics signal processing independent of temperature, except that the noise decreases with decreasing temperature. The charge gain, shaping time, zero suppression thresholds, and charge calibration capacitors are all temperature independent to better than 1% from room temperature to 89K. This feature makes it easy to verify the performance of an individual ASIC or an entire APA at room temperature with confidence that it will behave identically in LAr.

3.3   Summary

In summary, the entire LAr40 detector system has been planned and designed so that performance and risks are relatively insensitive to the size and geometric configuration of the final detector. A few prototypes will be sufficient to verify the success of this design, before a commitment to the construction of the full 20 kiloton detectors. Proving the concept of the TPC modules requires one moderately sized cryostat (e.g., 1kt).

3.4   Cavern Layout

The LAr40 Detector cavern will be excavated in a "mailbox" cross section. The long axis of the cavern will point towards Fermilab, parallel to the neutrino beamline. The pit, the rectangular prism portion inside of which the end-to-end cryostats fit tightly, will have the inner dimensions equal to the outer dimensions of the two cryostats end to end separated by a 20m septum. Considering that the cryostat has insulation and concrete liner, the pit will be 27m wide by 19m high by 130m long. The cavern roof, located above the pit, will be 33m wide by 142m long, and its rounded "mailbox top" upper surface will provide a clearance of 6m in the center and ∼3m on the sides. The curved upper surface will extend 10m beyond each end of the detector along the long axis to provide additional space (33m wide by 10m long) for ancillary equipment. The liquid argon purification system will reside within the 20m septum between the cryostats. Walkways will run the entire length of the cavern on each side of the detector to provide personnel access. A separately ventilated emergency-egress passageway will be located on one side of the cavern. The cryostat cover will be designed to allow easy access to the the emergency passageway from the other side of the cavern. One walkway is wider, which provides clearance to transport equipment from one end of the cavern to the other.

3.5   Detector vessel

The reference conceptual design for the LAr40 Detector cryostat specifies two identical cryostats placed end to end in one long cavern. Each cryostat is a rectangular vessel measuring 24m in width, 16.0m in height and 49.0m in length, and containing a total inventory of 25kt of LAr. It employs a membrane cryostat technology used in Liquid Natural Gas (LNG) shipping and for LNG storage on land and in caverns (as shown in Figure 3–4). A membrane tank uses a 1.2mm or 2mm thick, stainless-steel liner to contain the liquid cryogen. The membrane cryostat relies on external support from the surrounding rock to resist the hydrostatic load of the contents. In order from innermost to outermost layers, the side walls of the membrane tank consist of the stainless-steel primary membrane, 30cm of insulation, a secondary, thin aluminum membrane that contains the LAr in case of any leaks in the primary membrane; 70cm more insulation; a barrier to prevent water-vapor ingress; concrete; shotcrete and rock. See Figure 3–5.

This in-ground tank arrangement (ie. offering access only from the top) makes optimum use of the excavated cavern and minimizes safety concerns. The roof of the cryostat is constructed of truss-reinforced steel plate. All cryostat penetrations will be made through the roof. Relay racks containing the DAQ components will be located directly above each cryostat signal feedthrough.
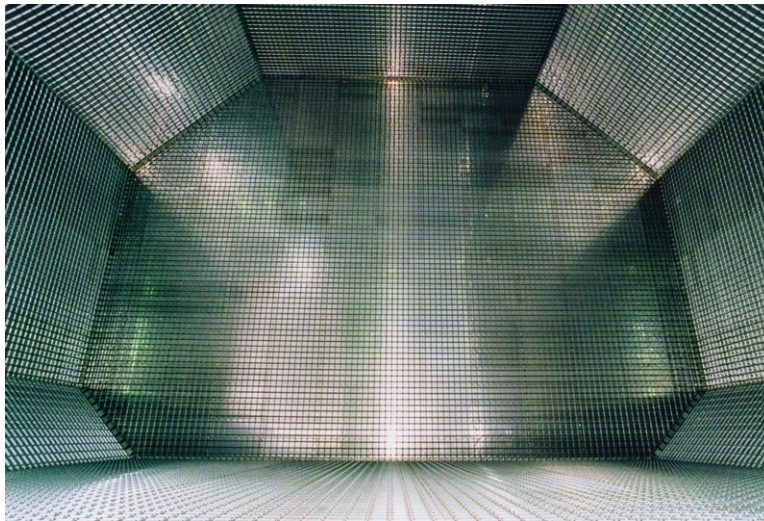
Figure 3–4: Interior hull of a LNG ship tanker. A typical tank is made of four $40,000\text{m}^3$ compartments, 35m high by 45m wide. The interior grid-like corrugations are on 0.34-m pitch. The above tank scales to 24m high by 35m wide. By comparison, each LAr40 cryostat is $19,000\text{m}^3$.

The membrane cryostat is a robust design with a proven record spanning more than 1600 tank-years of marine service, predictable cost, and known installation time. This design has been used to construct 48 in-ground storage tanks over the past 25 years.

LAr TPCs that have operated to date have achieved good argon purity after vacuum pumping the cryostat prior to filling with LAr. Vacuum pumping is an effective means of removing oxygen and water from materials within the cryostat but purging with dry argon gas is equally effective in principle. The purging approach is being tested in the Liquid Argon Purity Demonstrator (LAPD). Vacuum pumping of the LAr40 cryostats will be required if LAPD is a failure. A 3m x 3m membrane cryostat wall section was constructed at Fermilab to gain experience in the construction techniques. Vacuum tests on this wall section have shown that a membrane cryostat can be vacuum pumped down to a hard vacuum without any design changes to the vendor supplied components. Changes to the cryostat support structure would be required if the insulation space is evacuated however. Additional rock bolts would be need to be installed in the walls of the cryostat pit. The reinforcing steel in the concrete cryostat liner would be attached to the rock bolts to transfer the vacuum load to the rock bolts. Lastly, the height of the truss on the cryostat roof would need to be increased to 2m. These changes would add ~$10M to the cost of the project.
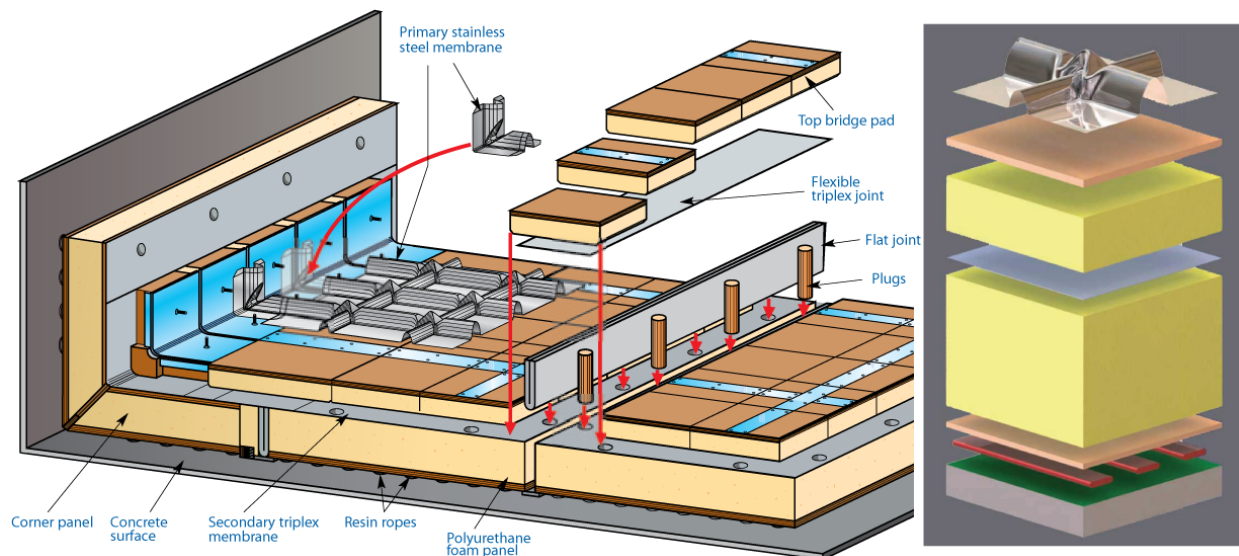
Figure 3–5: Illustration of the GTT membrane cryostat construction, courtesy GTT

Parameter	Value
Cryostat Volume:	19,000m^3
LAr Total Mass:	25kt
Inner/Outer Height of the Tank:	16m/19m
Inner/Outer Width of the Tank:	24m/27m
Inner/Outer Length of the Tank:	49m/52m
Insulation:	Reinforced Polyurethane
Primary Membrane:	1.2mm - 2mm thick type 304L corrugated stainless steel
Secondary Containment:	Aluminum and fiberglass sandwich
Outer Concrete Layer:	0.5m thick with embedded electric heaters, Ufer ground, inner surface treated with a vapor barrier.
LAr Temperature:	89 ± 1K
Depth of the Liquid (Liquid Head):	15.0m
Design Operating Pressure:	0.013MPa, above liquid 0.222MPa, Bottom of liquid
Rated Pressure Capacity of Tank:	0.52MPa (calculated according to BS EN 14620)

Table 3–1: Design parameters for the LAr40 Cryostat

Property	Reference Design Cryostat
Access to cavern	Drive-in
Construction access to pit	Through temporary construction opening in end wall at base of septum
In-cavern crane	Mobile with central monorail
Base slab	Reinfoced concrete
Side walls	Reinforced / post-tensioned concrete
Heating system	Redundant / replaceable Electric system
Roof	Pre-fabricated steel truss modules with lower steel plate
Vapor barrier	Polymeric on concrete surfaces / steel plate on roof
Insulation / Secondary barrier / Membrane	Vendor supplied
LAr containment system	Full containment: Stainless Steel Membrane / Secondary Barrier / Concrete Liner
TPC	Individual 2.5m x 7m x 9cm frames lowered through 2m x 4m roof hatch. Assembled within cryostat and suspended by hangers passing through the roof.

Table 3–2: Summary of parameters for the 800L membrane cryostat for reference design (non-evacuable, relying on a room-temp argon purge of the cryostat to remove oxygen and water from the interior prior to filling with LAr).

3.6   Cryogenic Systems

The choice of the cryogenic system's layout and location is intended to optimize safety and efficiency. It will:

- Minimize the risk of personnel injury to any Oxygen Deficiency Hazard (ODH),

- Minimize heat ingress to the cryogenic system (by minimizing piping length and pump power),

- Minimize the volume of the argon system external to the cryostat and hence minimize the potential for argon escape or contamination, and

- Provide safe access to refrigeration equipment that requires periodic third-party mainte-nance.

The re-condensers and purifiers will be located underground, adjacent to the cryostat. A surface facility will be located immediately outside the new 300L drift near the existing Kirk portal. The surface facility will include a 50m^3 LAr receiving dewar, three 75kW liquid nitrogen (LN) refrigerators (two operating and one spare) and a 50m^3 LN dewar.

Experiment	LAr Vol (m^3)	Liquid Purification Rate (kg/hr)	Gas Purification Rate (kg/hr)	LAr Volume Change Rate (days)	Electron Lifetime (ms)
ICARUS T600	550	2766	168	10.8	7
ICARUS prototype	10	692	0.69	0.8	1.1
Material Test Stand at FNAL	0.25	167	5.56	0.1	>5
ArgoNeuT	0.55	0	4.3	7.3	0.75
MicroBooNE	123	6875	83	1.0	TBD
LAr Purity Demonstrator (LAPD)	22.2	3791	46.7	0.3	TBD
LBNE LAr40 (1 module)	18600	188000	1100	5.7	1.4 req'd

Table 3–3: Purification comparision data for LArTPCs

Risers and other pipework linking the cavern to the surface will be routed through a 4.0m diameter vertical exhaust-ventilation shaft. The shaft will contain LN supply and return pipes, an LAr pipe, vent piping and control-system wiring.

Each cryostat will hold an inventory of 25kt of liquid argon. We will need to procure approximately 55kt of liquid argon. Total argon production, considering all suppliers within the United States is currently 3.6kt per day. Argon is normally co-produced along with large volumes of oxygen, so any demand that requires large oxygen quantities may also spur additional argon production, enhancing the supply capacity. A 2013-2018 market-forecast report indicates that the demand for argon will increase at a rate of 3.4% per year whereas the demand for oxygen will increase 4.8%. Nitrogen production is expected to increase due to above-average growth in health-care markets and food-packaging applications. We conclude from the report that the availability and pricing for argon gas will be on par, or more favorable than, current market conditions. The estimated 2010 cost for liquid argon is $1M per kt.

The required flow rate of liquid argon to be sent for purification is expected to decrease over time. The initial maximum flow rate will be 136m^3/hr (600 gpm)from each cryostat. The liquid-argon volume will turn over every five days at this initial maximum rate. Longer term, the rate will decrease to 34m^3/hr with a turn-over rate of 20 days. As point of comparison, ICARUS T600 has a maximum turn-over rate of eight to ten days. See Table 3–3 for a comparison of purification rates among experiments and LBNE. To achieve the turn-down required between the short-term commissioning flow rate (600 gpm) and the long-term operational flow rate (150 gpm) through the purifiers, four 150 gpm pumps will be located in the cryostat. The purification plant will consist of a duty stream and an identical standby stream, each consisting of a molecular-sieve column and an activated copper column.

3.6.1 Cryogenic Safety

An ODH analysis has been completed for the cavern. One hundred and thirty six different failure scenarios were considered and a resulting oxygen concentration and fatality rate was calculated. The overall fatality rate is the sum of the fatality rates for all scenarios. The result of the calculation was $2x10^{-7}$/hr if no precautions are taken. This is similar to the Dept. of Labor fatality rates for farming and ranching [1]. The major contributors to the fatality rate are cryogenic piping and small tanks; not the membrane cryostat. This rate is just above the threshold of ODH Class 0 where no precautions are required. We will use Class 1 measures including warning signs, ventilation, medical approval, ODH training, use of personal oxygen monitors and air-packs. The fatality rate, after these measures are included, is $2x10^{-9}$/hr, similar to the fatality rates for office workers.

A cryogenic spill and venting analysis was completed to check for environmental effects at the surface using the ALOHA plume modeling software. The analysis showed that the Michelson Trail and the public would not be affected even in the worst case scenarios.

3.7   Time Projection Chamber Elements

The TPC is located inside the cryostat vessel, completely submerged in liquid argon at 89K. The TPC consists of a rectangular array of 3 wide x 2 high x 18 long TPMs for a total of 108 APAs and 144 CPAs in each cryostat. See Figure 3–6 for a cross section of the cryostat. The maximum electron-drift distance between a cathode and an adjacent anode is 3.7m. A total of 6 such drift regions form the 22.4m active width of the TPC. Both the cathode and anode plane assemblies are 2.5m long (in the beam direction) and 7m high.

On each anode plane assembly, four planes of wires cover each side of the stainless steel APA frame as shown in Figure 3–7. These four planes of wires are, along the direction of electron drift: a vertical grid plane, two induction planes at $\pm45°$ angles, and the final vertical collection plane. Each plane of wires has its specific bias voltage to guarantee complete electron transmission through the outer three wire planes and complete collection on the inner most plane. On the three inner planes, each wire is connected to a front-end readout channel. The wires on the outer grid plane are biased but not read out. They form a electrostatic shield to improve the signal strength of the first induction plane and also to provide electrostatic discharge protection for the front end electronics during handling. At a nominal wire pitch (center-to-center separation) of 5mm, the total number of instrumented wires in an APA is 2560, making 276,480 in each detector.

This wire plane configuration provides N+1 redundancy. Two instrumented wire planes are required to reconstruct a three dimensional track in the detector. Detector performance would be unaffected if, for example, all electronics channels in one plane failed. Another ben-

two sets of
G,U,V,X wire planes

cold electronics boards

7m

14m

detail cross section of the
electronics enclosures

concept of the APAs, and
wire wrapping arrangement

2.5m

installation of APAs inside the crypstat

Cryostat access
hatch,
plugged when
cryostat is filled

Wire and Cathode
frames are transported
in halves which are
joined in cryostat

Cathode Plane Assemblies   Anode Plane Assemblies

Field Cage

14m

22.4m

Foam Insulation

Concrete Liner

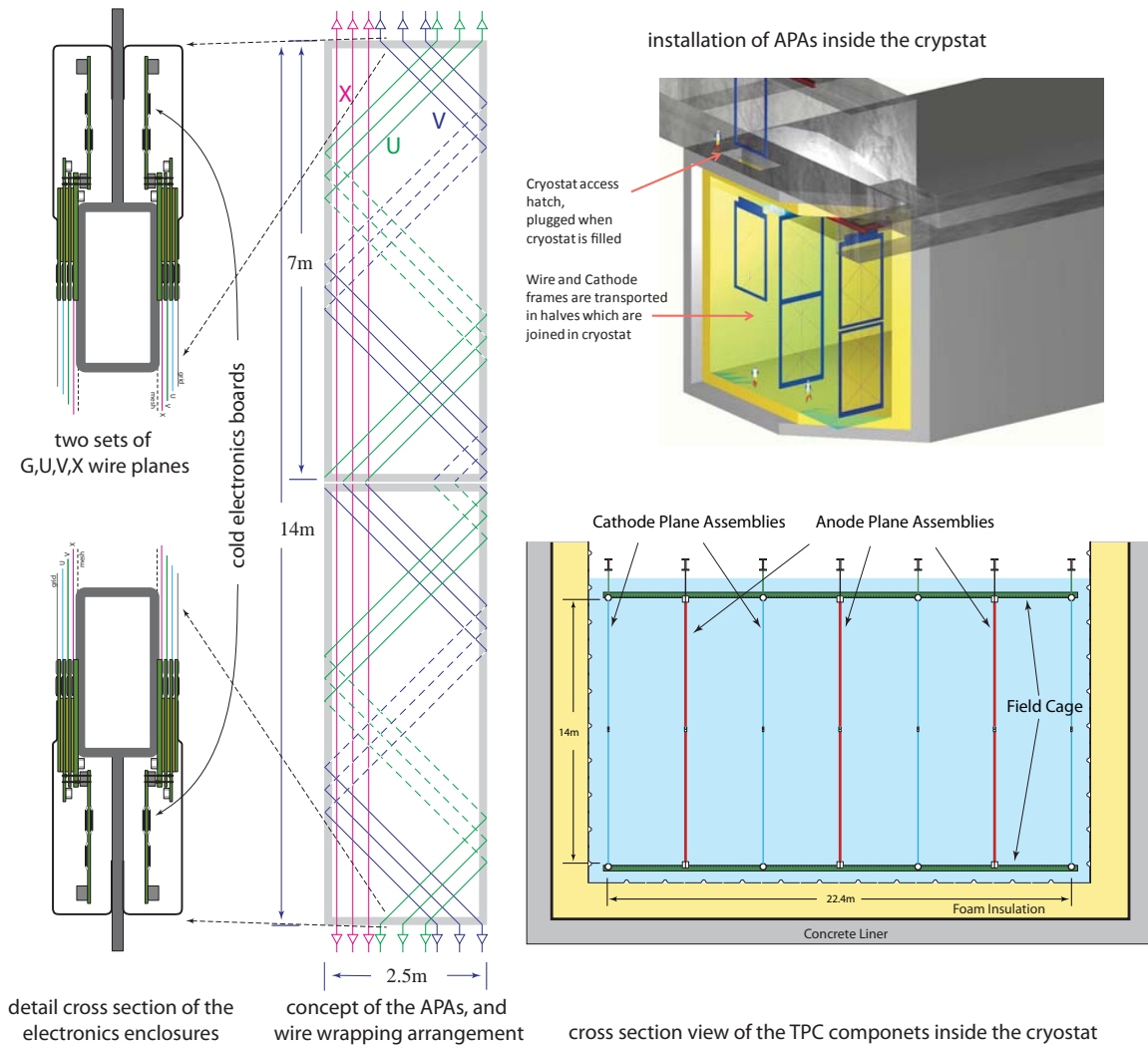cross section view of the TPC componets inside the cryostat

Figure 3–6: TPC modular construction concept

efit of having a redundant readout plane (at a different angle) is that it should in principle result in a small improvement in the efficiency of discriminating electrons from photons near the interaction vertex.
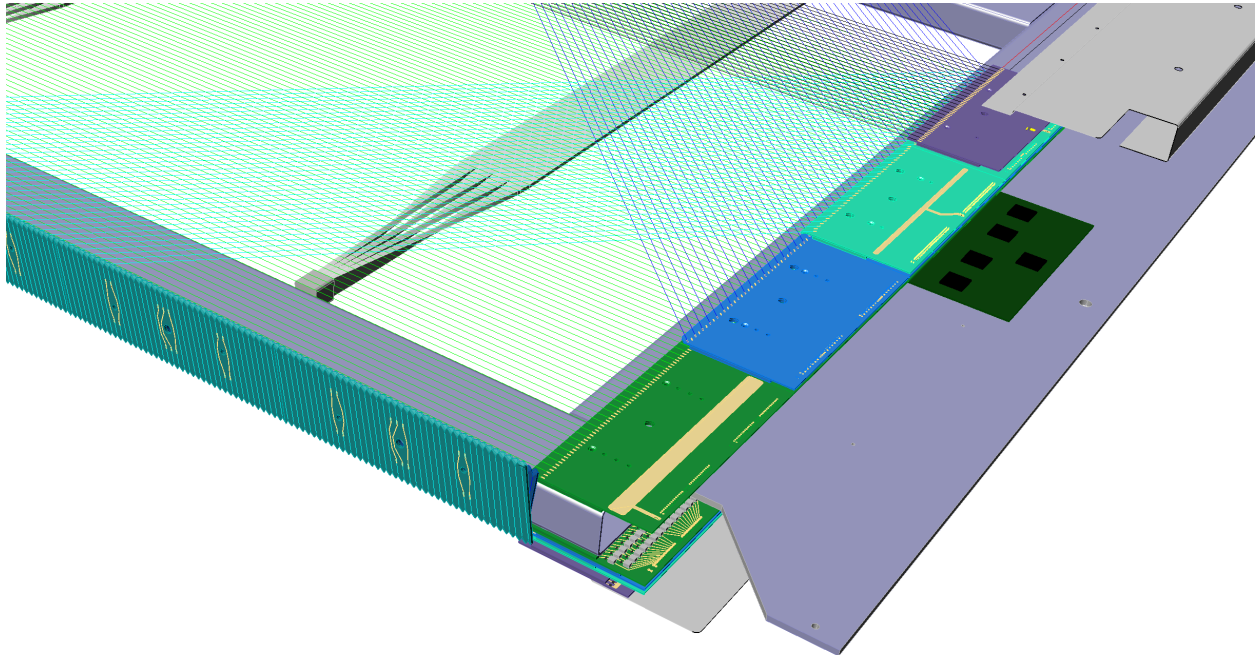

Figure 3–7: Corner view of an APA. Wires strung at 0°, 45° and -45° are attached to circuit boards at the sides and ends of the APA. One of the 10 photon detection system "paddles" that reside in each APA is shown. One readout board is shown in dark green. A metal cover encloses the readout boards.

150 μm diameter hardened Cu-Be wire is chosen due to its strength, good solderability, and low cost. The wire has a break strength of about 30 N. A 5 N nominal wire tension is planned to provide sufficient safety margin against accidental wire breakage. SS wire would appear to be a logical alternative, but is not suitable due to the high cost of wire termination. Intermediate wire support structures are places at specific intervals on the wire frame to maintain the wire pitch and prevent excess wire deflection. The wires will be both soldered and glued onto printed circuit boards mounted at all four edges of the wire frame to ensure both electrical connection and mechanical attachment.

The wire wrapping scheme allows the readout electronics to be placed at only one edge of the wire frame and allows joining APAs at the 3 non-readout edges to form a large sensitive plane with very little dead space at the joints. The front-end readout electronics are installed along the top edge of the upper APAs and the bottom edge of the lower APAs. All signal and power cables to the lower APAs are routed through the vertical hollow frame members of the APAs.

The central element of the photon detection system is an acrylic light-guide that is coated with a wavelength shifting fluor. The light-guides are coupled to a small PMT. This assembly, or

"paddle", resides within the APA frame as shown in Figure 3–7.

Each cathode plane assembly is also made of a stainless-steel frame, with a layer of stainless-steel wire mesh stretched over one side of the frame. To reduce drift-field distortion, all surfaces that rise significantly above the mesh, including the stainless-steel frame structure on the other side of the mesh, are covered with field-shaping electrodes biased at appropriate voltages.

Each pair of facing cathode and anode rows forms an electron-drift region. A field cage completely surrounds the four open sides of this region to provide the necessary boundary conditions to ensure a uniform electric field within, unaffected by the presence of the cryostat walls. The field cage needs to be constructed from a set of parallel conductors at a uniform pitch. Each conductor is biased at a specific voltage, through a resistor divider network to form a linear voltage gradient. The field cage is made in sections 2.5m x 3.7m in size. Field cage sections will be delivered already attached to the CPAs with hinged connections at the top (for top CPAs) and bottom (for bottom CPAs). After each CPA is hung in place in the cryostat, the field cage sections will be swung to the horizontal position and attached to the APA frames, forming a rigid mechanical structure. The field cage tubes are held at the appropriate voltage by a resistor network.

The nominal drift field is 500 V/cm. Over a 3.7m drift distance the maximum bias voltage required on the cathode plane is -185 kV. Eight custom high voltage feedthroughs will be built and installed through the cryostat roof to provide the required voltage to the CPAs.

The entire TPC is suspended under the cryostat ceiling. This configuration eliminates the need for complex mechanical structures to keep the TPC stable. The finished cryostat has rows of anchor feedthroughs distributed along the ceiling. The TPC mounting rail is supported by stainless steel rods to each row of the anchor points.

3.8   Electronics, Readout and DAQ

The large number of readout channels required to instrument the LAr40 TPCs dictates the use of CMOS ASICs for the electronics. Requirements of low noise and for extreme purity of the LAr demand that the front-end electronics be located at the signal wires in LAr, which reduces the signal capacitance (thereby minimizing noise) and, because signal multiplexing can then be implemented, minimizes the number of cables and feedthroughs in the ullage gas (minimizing the risk of contamination from outgassing of cables and leaks from the atmosphere). This electronics architecture, combined with the modular TPC elements, also leads to a TPC implementation that can be readily scaled to any detector size or geometry.

Fig.3–8 shows the conceptual architecture of a front-end electronics design that meets the requirements for LAr40. The entire electronics chain is immersed in the LAr and operates at 89K. It is composed of a 16-channel front-end implemented as a mixed-signal ASIC providing

amplification, shaping, digitization at 2MHz, zero suppression, buffering, a 16:1 multiplexing stage, a driver and voltage regulators. Eight such front-end ASICs plus a single digital ASIC implementing an 8:1 multiplexer, clock and control circuitry comprise a single 128-channel front-end readout board. 20 such readout boards provide complete coverage of an APA. The output from each of the readout boards are mirrored and connected to two redundant digital ASICs containing a multiplexing stage (20:1) and driver. The data from all 2560 channels on an APA are ultimately multiplexed into a few redundant serialized output links connected through signal feedthroughs on the cryostat ceiling to the DAQ system outside of the vessel. Data rate estimate for the current detector configuration is within the capability of either a twisted copper pair or an optical fiber. The choice between twisted-pair copper and optical fiber will be postponed until further work is completed to evaluate the long-term reliability of optical drivers at LAr temperature.
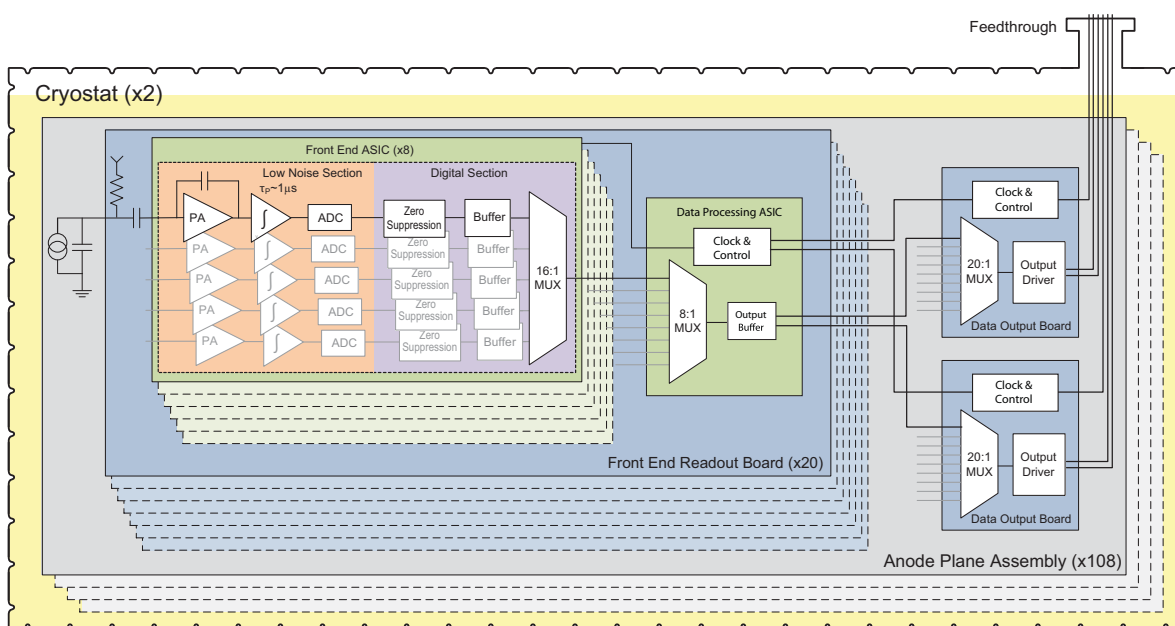
Figure 3–8: Conceptual front-end electronics architecture

S

At the 800L, the electronics occupancy in an APA in a full drift time is very low. An efficient zero-suppression scheme can greatly reduce the total data volume. One scheme can be implemented with a dedicated buffer for each channel having a write-enable consisting of the OR of that channel and its two nearest neighbors. A few samples before and after the write enable would also be recorded to capture the below-threshold leading and trailing edges of the signal waveform. This mode provides maximal zero-suppression that is insensitive to localized low energy events and noise.

The in-vessel electronics will sample data continuously. The data rate will be dominated

by backgrounds due to cosmic rays and radionuclides, predominantly naturally occurring Ar^{39} which has a Q value of 565keV $\approx$0.5 MIP. Table 3–4 shows the data rate estimates for the major sources of background at the 800L. The total data rate, with zero suppression, is $\approx$13Mb/s per APA. The Ar^{39} decay rate is 122kHz/APA. The rate of sampled decays for a 0.5 MIP threshold will be 34kHz. The mean range of the decay β is 30μm, so each point ionization will appear in the data as 8 ADC samples above threshold. The two adjacent wires will also be sampled in the same time window.

Source	Event Rate	Data Rate
Ar^{39}	122 kHz	9.8Mb/s
Kr^{85}	28 kHz	2.3Mb/s
FE series noise	1 kHz	0.02Mb/s †
cosmic muons	7.2 Hz	0.3Mb/s
Co^{60} gammas	2.5 kHz	0.2Mb/s
Total		12.9Mb/s

Table 3–4: Major contributors of the data rate in an APA at 800L. † For noise = 600 electrons, 3000 electron threshold and 1μs shaping time.

To successfully design CMOS circuits to operate at cryogenic temperatures, two critical aspects must be considered and resolved. The first is the need for realistic models of active devices, interconnects and passive components in order to reliably predict operating points, signal response, and noise during the design process. The second is the requirement that the design must ensure a long operational lifetime, since once the TPC is filled with LAr the detector must operate for over 20 years with only rare access to the electronics for repair or replacement.

Our preliminary results from the cryogenic characterization (down to 40K) of a complete mixed-signal ASIC in a commercial CMOS 0.25μm technology, developed for room-temperature applications, indicated that the models are reliable to first order, although they may need minor adjustments.

Concerning reliability, the most relevant failure mechanisms in CMOS, i.e., electro-migration (EM), stress migration (SM), time-dependent dielectric breakdown (TDDB), thermal cycling (TC), and negative bias temperature instability (NBTI), all scale such that cryogenic operation is favored [2][3]. The only mechanism that could affect the lifetime at cryogenic temperature is gradual degradation due to impact ionization, which causes charge trapping in the MOSFET gate oxide at large drain-current densities. Results from one of our collaborators[4] provide general design guidelines (for device geometry, bias, and current density) that should guarantee a lifetime well in excess of 20 years for continuous cryogenic operation. These design guidelines also provide information for designing test conditions to observe the deterioration mechanism and to estimate deterioration rates within practical measurement times. Such tests will be conducted on prototype samples throughout the development process to verify the long-term reliability of the ASICs.

In order to begin the process of refining the circuit-design models and guidelines, we have designed and fabricated in a commercial CMOS process (0.18μm and 1.8V, a process expected to be available for at least another 10 years) a 16-channel ASIC implementing the complete analog front-end section of the readout chain [5]. It has been characterized at room (300K) and liquid nitrogen (77K) temperatures. During these tests the circuit was cycled 30 times between the two temperatures and operated without any change in performance. Figure 3–9 shows the measured pulse response, along with details on the adjustability of the gain, peaking time, and baseline. These results are in close agreement with the simulations and indicate that both the analog and the digital circuits and interface operate as expected in cryogenic environment. The charge calibration capacitors implemented on each channel have been found to be stable within 0.5% between room temperature and in LN. This will enable us to perform calibration of charge signal to the precision of about 1%.

The reference design for the DAQ system is guided by recent experience gained in the development of relevant systems for the NOvA and MicroBooNE experiments, as well as from running experiments with comparable channel counts and/or experimental conditions, such as D-Zero, CDF, MINOS and ICARUS. The DAQ system will be located external to the cryostat vessel, with components in the detector hall and in an on-site control room. It consists of the following components:

- Custom 'Data Concentrator Modules' (DCM) located in racks that sit directly above the signal feedthroughs on the roof of the cryostat. The NovA DCM is suitable for LAr40 with minor modification. These connect to:

- A network consisting of commercial Ethernet switches located in the detector hall and a commercial router located in the counting house/control room, for the transmission of data to:

- A local farm of commodity computers that provide data storage, trigger, event-building and real-time processing/event reconstruction functions,

- A custom timing system consisting of a master unit that locks onto a GPS clock and distributes timing signals to the data concentrator modules via slave units, and

- Dedicated computer nodes that host run control, routing control, node supervisor and slow controls processes.

The reference design of the data acquisition system is summarized in block diagram form in Figure 3–10. The design strives to minimize the impact of single-point failures, and maximize the use of commercial components.

The data rate into the DAQ is modest, $\approx$13Mb/s per APA (or 2.8Gb/s for both TPC modules). Approximately 12Mb/s is due to Ar^{39} and K^{85} β decays that produce a point ionization on
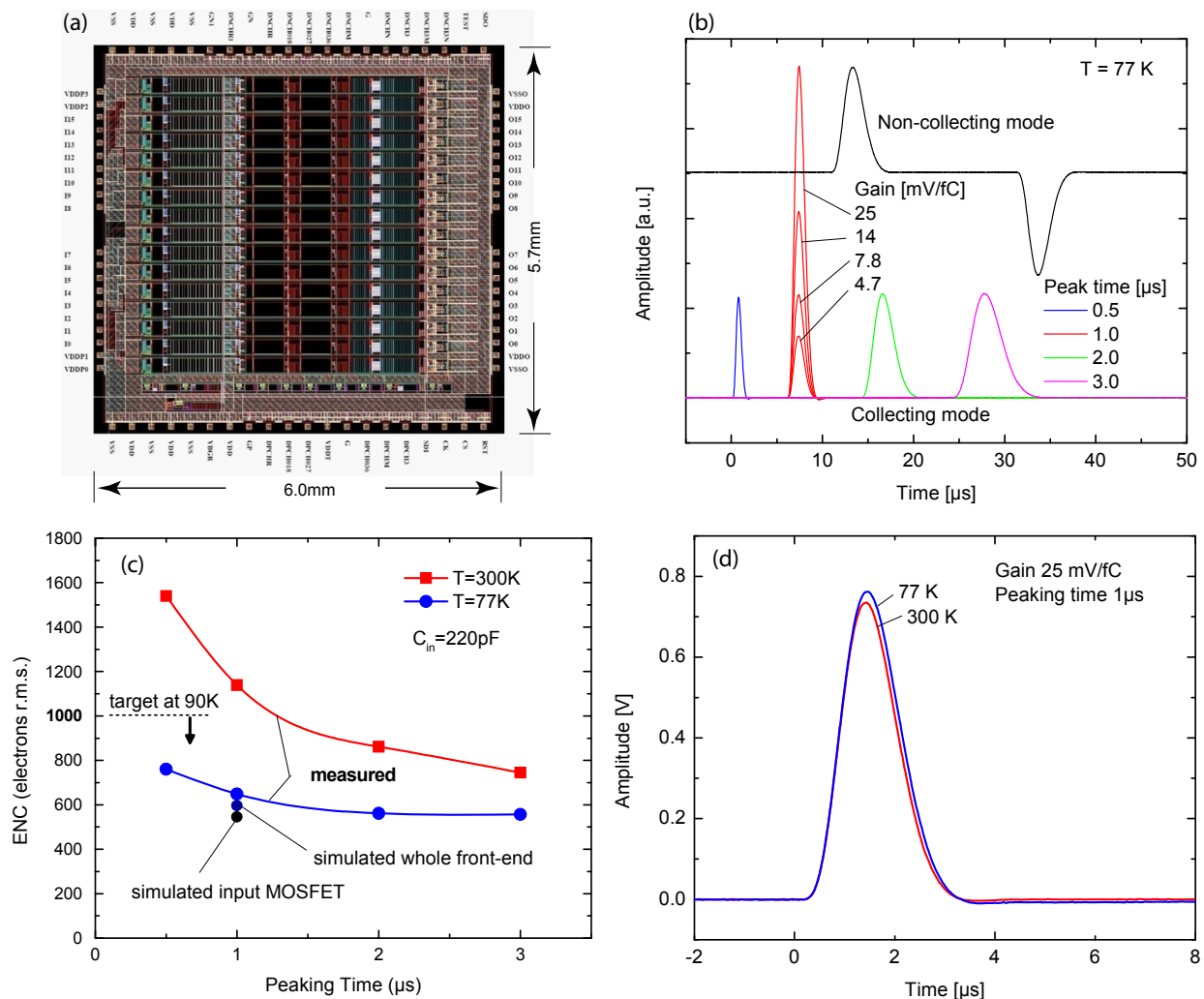
Figure 3–9: (a): Physical layout of the first analog ASIC.(b): Measured impulse responses of the ASIC demonstrating the adjustable gain, shaping time, and baseline offset features of the chip. (c): Measured ENC (Equivalent Noise Charge) for the analog ASIC at 300K and 77K at the four peaking times. (d): Measured impulse responses at 300K and 77K with $1\,\mu$s peaking time.
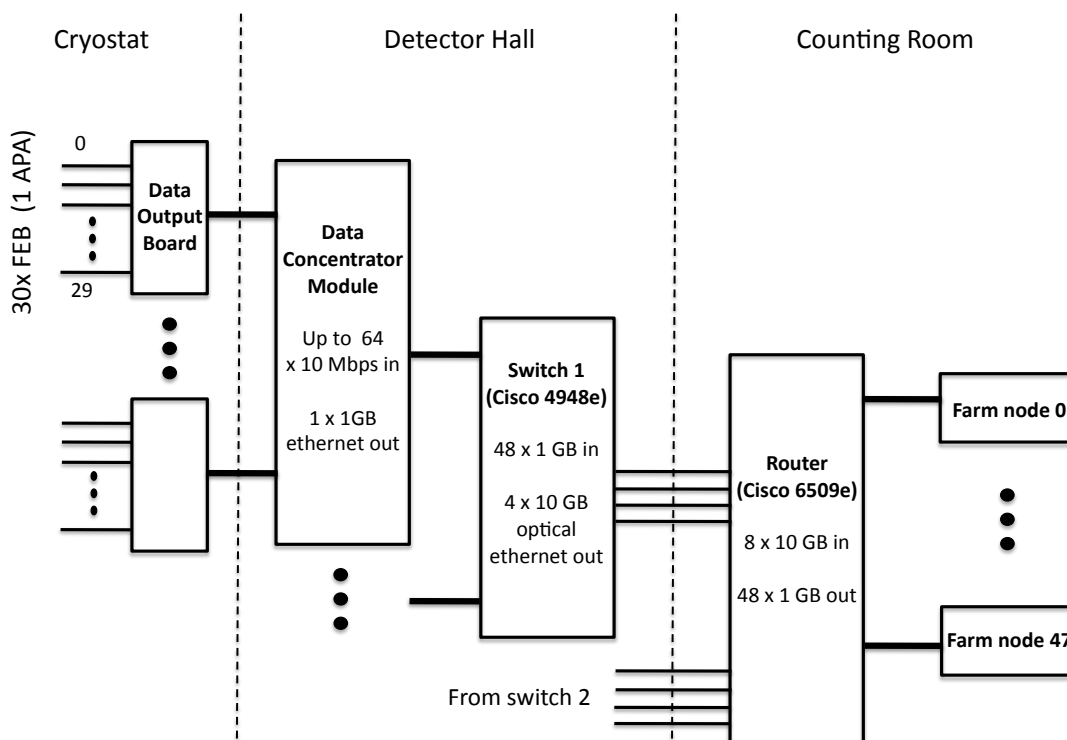
Figure 3–10: Block diagram depicting the DAQ reference architecture

a single wire. The first stage of data filtering will be to remove these isolated hits since all physics processes of interest produce particles that deposit more than a few MeV in LAr. The filtered data will be stored for a time period sufficient to capture supernova burst neutrinos.

3.9   Auxiliary Systems

3.9.1   Muon Veto System

The most challenging source of nucleon-decay background to reject for the SUSY-favored $p \rightarrow \nu K^+$ decay mode is production of K^0_L mesons by interactions of cosmic-ray muons in the rock surrounding the detector. These neutral kaons may enter the detector and produce a K^+ via charge-exchange, thereby mimicking the nucleon decay signal. The cosmic muons that pass through the rock near the cavern wall at small zenith angle produce the largest contribution to the K^0 background. Muons traveling at a larger zenith angle are unlikely to produce a forward-going K^0 that is unaccompanied by the interacted muon.

The effective interaction length of these K^0's in liquid argon is 86cm. A simple fiducial cut requiring candidate proton-decays to occur several interaction lengths away from the sides of the LAr40 detector would result in a very significant loss in fiducial volume. Instead, the LAr40 veto-system reference design calls for approximately 12,000 veto tubes embedded at two depths in the cavern walls.

The veto system provides veto counters for insertion into each veto tube. The design and the cost estimate are adapted from the NOνA detector. Each veto tube consists of a 4" square steel tube that extends 7m beyond the perimeter of the cavern. The veto tubes are provided by the conventional facilities sub-project. The veto system has two levels, one above the detector and one near the bottom. The top veto level covers the top of the detector in addition to the sides.

At each level, three layers of veto counters are arranged parallel to each other, and are offset to provide full geometric coverage for cosmic rays at all angles as shown in Figure 3–11. Veto counters will be inserted in two of the three layers. The third layer of veto tubes is provided to allow for a future upgrade if two instrumented layers is found to be inadequate. This configuration does not provide stereo angle information to determine the distance from the cavern wall to the cosmic ray. Pulse-height information can conceivably be used for this purpose with an accuracy of a few meters.

The 7m length was chosen based on the results in Reference [4] in Chapter 4. The interaction length of rock is roughly half the interaction length of liquid argon, so each meter of rock should provide twice the neutral-kaon attenuation as each meter of liquid argon.
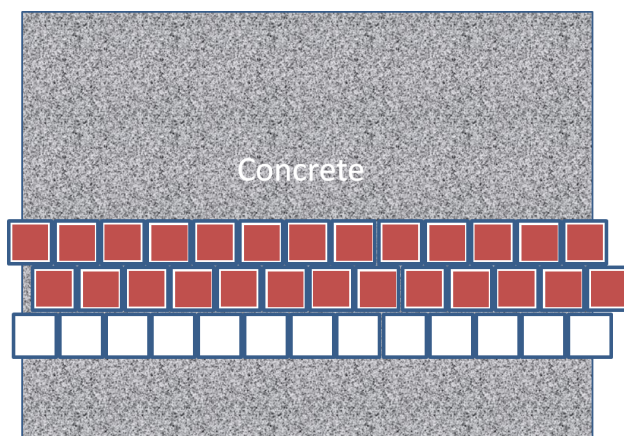
Figure 3–11: Veto tube layer configuration. Veto tubes consist of 4" square steel tubing embedded in the concrete wall of the cavern. Veto counters are inserted in the top two rows.

Each LAr40 veto counter will consist of a 9m long × 8.4cm square PVC extrusion containing liquid scintillator and a loop of wavelength-shifting (WLS) fiber. The 9 meter long PVC extrusions in the lower level array will be installed in shorter length sections and glued together with couplings. The interior dimensions of the PVC extrusion are 7.8cm square. Both ends of the WLS fiber are attached to a single-channel Avalanche Photo-Diode (APD) mounted on the extrusion end-cap. Scaling the performance and geometry of a NOνA cell to the proposed LAr40 veto cell, a minimum ionizing particle passing through the far end of the cell is expected to produce 67 photo-electrons at the face of the APD. A conservative threshold at 15 photo-electrons would result in an inefficiency of $\approx 10^{-8}$. Since the LBNE LAr detector will have a much larger overburden than the NOνA Far Detector, it is likely that the threshold could be set even lower than 15 photo-electrons.

The veto will be implemented in the data acquisition as an additional system. The veto detectors will be sampled by ADCs operating at 2MHz and merged with the TPC data stream. The veto system will be used to reject a reconstructed K^+ as a proton-decay candidate if a nearby veto counter has a pulse height consistent with a minimum-ionizing particle.

3.9.2   Photon Detection System

Identification of the different possible charged-particle types depends on accurate measurements of ionization along tracks. The measured ionization charge, Q, is related to the true ionization charge, Q_0, by $Q = Q_0 e^{-t_{drift}/\tau}$ where $t_{drift} = t_{arrive} - t_e$ is the drift time, t_{arrive} is the measured arrival time of electrons at the anode plane, and τ is the lifetime of the drifting ionization electrons measured by purity monitors in the cryostat. Determination the absolute location of the event along the drift axis, and hence Q_0, depends on the time of interaction t_e.

For non-accelerator physics events, a priori knowledge of t_e is not guaranteed through the

measurement of ionization alone. However, liquid Argon is an excellent scintillator, generating of order 10^4 128nm photons per MeV of deposited energy. Detection of scintillation (and accompanying Cherenkov) photons provides a prompt signal that would allow unambiguous location of particle positions along the drift axis, as well as a means to infer the actual ionization loss of particles from the measured charge.

As an example, photon detection in the LArTPC offers high efficiency for the "golden" proton-decay channel $p \rightarrow \nu K^+$. A significant background for this channel results when a cosmic-ray spallation event occurring just outside of the TPC produces a charged kaon that enters the drift volume. Without knowledge of the time at which it enters, the detected partial kaon track could be mis-reconstructed as having a starting location within the TPC fiducial volume, and could be mistaken for a proton-decay candidate. This background can be eliminated by measuring the time at which the kaon first enters the detector. Although it is possible to infer t_e in some cases through other means – for example by calibrating to the energy loss of the minimum-ionizing muon produced when the kaon decays to $\mu^+ \nu$, a photon detection system would work for other cases as well.

The central element of the photon detection system is an acrylic light-guide coated with the wavelength shifting fluor tetraphenyl butadiene (TPB). Scintillation light produced by re-combining ionization electrons is emitted at 128nm - in the vacuum ultraviolet region. The TPB coating on the light-guides efficiently converts the scintillation photons to 428nm. Approximately 5% of the converted photons are captured within the light guide and travel to a small PMT. Ten light-guide and PMT assemblies, or "paddles", will be installed within each APA frame prior to wire winding. The PMT signals will be read out by the same electronics used to read out the wire signals. The PMT signals will be used to form a software "trigger" in the DAQ to define the event time, t_o, for non-accelerator events. This system provides a t_e signal throughout the entire detector in contrast to a system similar to that used in MicroBooNE and ICARUS, where light is detected outside the detector volume.

The photon detection system should also enable a measurement of the neutrino velocity if the raw PMT signals are routed out of the cryostat.

3.10   Detector Installation and Operation

LAr40 construction and installation will occur in several distinct phases:

- Installation planning and prototyping.

- Surface storage identification and operation.

- Excavation and outfitting of the cavern. This activity is the responsibility of the conventional facilities sub-project.

- Construction and installation of the cryogenics system and cryostat by a construction management firm.

- Construction of detector components at collaborating institutions and shipment to the far site.

- Installation of detector components

- Cryostat and detector commissioning

An installation and integration detector mock-up will be constructed at Fermilab to confirm that interfaces between detector systems are well defined and to refine installation procedures. A mechanical mock-up of several APA's will be constructed. The APA mock-ups will include all mounting points and interface points such as optical fiber readout cables and power cables.

3.10.1   Cavern, Cryostat & Cryogenics Construction

The cavern excavation, construction and infrastructure are mostly conventional. One notable difference is our plan to utilize the cryostat pit rock bolts as part of the grounding scheme. In our case, the rock bolts in the pit will extend through the shotcrete that lines the cavern. The rock bolts will be attached to the reinforcing steel network within the cryostat concrete liner, forming an "Ufer ground". The reinforcing steel will be connected to the steel truss cover. The Ufer ground will be connected to the "detector ground" (the cryostat SS liner) through a single low impedance connection. The design and construction of the power distribution system is equally important. "Quiet power" for the detector electronics will be supplied by a transformer at some distance from the cavern to take advantage of the inductance of the power lines. The quiet power transformer will be double Faraday shielded. The primary shield will be connected to the main substation via a grounded feed wire and the secondary shield will be connected to the Ufer ground.

The first activity after beneficial occupancy of the completed cavern from the conventional facilities sub-project will be to validate the functioning of the ventilation system. This will be accomplished by explicitly testing the ability of the ventilation system to remove argon vapor from the cavern. Oxygen monitors will be temporarily located in the cavern and in the ventilation shaft. A large dewar of LAr will then be placed in the cavern and the contents allowed to spill on the floor. The ventilation system design will be validated by comparing the time dependence of the oxygen concentration throughout the cavern with the ODH analysis calculations. Remedial action will be taken if required during cryostat and cryogenics construction.

Cryostat and cryogenics construction will then be performed by a construction management firm that has experience with large cryogenics systems. Careful oversight is required during construction to ensure that the power distribution and grounding scheme is maintained.

3.10.2   Detector Installation

Detector components will be shipped in sealed containers to the far site by truck and delivered to the cavern. Shipping containers will be moved to a clean area over the septum between the two cryostats. Components will be lowered through an access hatch into the cryostat using a local monorail. A bottom APA will be temporarily set on fixture that sits on a temporary floor in the cryostat. A top APA will next be be lowered into the cryostat and attached to the bottom APA. The APA pair will next be transferred to the mounting rails that span the length of the cryostat and the pair will be rolled into their final position. Pairs of CPAs will be installed in similar fashion. The field cage sections that were attached to each CPA are then swung into position and attached to the adjacent APAs. Each APA pair is next connected to the DAQ system. Wire integrity will be confirmed by measuring the Equivalent Noise Charge (ENC) of each electronics channel and comparing it with the expected noise for a properly connected wire. A properly connected wire provides an input capacitance of 240 pF to the front end amplifier resulting in an ENC at room temperature of 1100 electrons.

The wire integrity test also ensures that coherent noise sources are discovered promptly when they are created. A likely cause would be someone making a mechanical connection between the detector ground and the Ufer ground. Error budgeting, regular noise monitoring and mitigation will ensure that the TPC reaches and maintains the required noise performance before the cryostat is cooled down.

Wire integrity testing will continue during cool-down of the cryostat. The cool-down rate will be significantly lower (300K to 89K in ~20 days) than the cool-down rate used during APA post-construction testing (300K to 77K in several hours). This will ensure that the temperature induced stresses in the APA frames and wires are kept well below the level experienced during testing. In the unlikely event that wire breakage occurs during cool-down, the cryostat would be warmed to room temperature and repairs made to the detector.

There is an opportunity for a cryostat leak to be created during detector installation. This activity will by necessity occur after cryostat construction and leak checking. Two measures will be instituted to mitigate this possibility: 1) a temporary floor will be installed in the cryostat to protect the membrane against dropped objects and 2) the insulation vacuum will be monitored and connected to an alarm that will sound if the pressure rises, indicating that a leak has developed.

3.10.3   LAr Filling Sequence

Both cryostats will be qualified using the methods described above before installation and liquid filling begins. One cryostat will be filled with liquid argon while detector installation proceeds in the second. Filling one cryostat is estimated to take 4 - 6 months. LAr purification will begin when the liquid level is high enough to start the recirculation pumps. Installation of

the TPC in one cryostat is estimated to take 9 months allowing ∼3 months for initial purification without any delay in the installation schedule.

The argon purity in the first cryostat will be monitored during filling using in-vessel purity monitors. If the drift electron lifetime is found to be inadequate, the argon will be transferred into the second cryostat after TPC installation is completed. Repairs to the first cryostat would be made. The argon purity in the second cryostat will be measured by tracking cosmic rays in the newly commissioned detector. The argon would be returned to the first cryostat and the purity test repeated. When completed, the argon would be transferred back to the second cryostat. Operation of the detector in the second cryostat would commence while installation proceeds in the first.

There is an opportunity to optimize in the last phase; during detector installation in the first cryostat. Useful experience will be gained from the previous detector installation and will be applied to the second.

3.10.4   Operations

The TPC in the second cryostat will have been in operation for 9 months when detector installation is completed in the first cryostat. The opportunity exists to effect repairs if unforeseen problems arise in this time period in the operating detector module, since the first cryostat has not yet been filled with LAr. It is for this reason that we have elected not to include a tank for the temporary storage of the LAr inventory of one module. The cost of an above-ground 19,000 m^3 tank is roughly equal to the cost of the LAr (∼$50M) and it is highly unlikely that it would ever be used. It is also highly unlikely that immediate access to a cryostat would be necessary during operations, considering the staging sequence for detector installation and filling. Serious problems that might occur would likely result in a gradual degradation of detector performance over time. If this occurred early in the program, a decision would be made to invest in a storage tank. Detector operations would more likely be extended to achieve the science goals if degradation occurred later in the program.

One should note that the environment inside a cryostat containing purified LAr is benign compared to a detector operated at room temperature; a pertinent observation regarding prospects for reliable long-term operations. The rate of chemical processes, which could affect component lifetime, is a factor 10^{17} lower at LAr temperature compared to 300K. Mechanical creep, which could affect the long term reliability of the TPC, is also lower by many orders of magnitude. All deleterious effects in electronics devices are greatly reduced at low temperature, with the exception of impact ionization, described in the previous section. Lastly, the temperature in the LAr is extremely stable since it is in a saturated-liquid state.

Under normal operation, two LN refrigeration plants will be in operation while one is on standby. The cryogenic system includes two storage dewars - a 50m^3 LN dewar and a 50m^3 LAr

dewar. Under normal conditions, 1.8m^3/hr of LN is required to re-liquefy the boil-off argon gas. If a power outage occurs, the LN dewar will provide 28 hours of backup before argon gas begins to vent. The argon gas would be released through a surface stack located near the cryogenics building.

Bibliography

[1] "Bureau of Labor Statistics", http://www.bls.gov/iif/oshcfoi1.htm/#rates

[2] J. Srinivasan, S. V. Adve, P. Bose, and J. A. Rivers, "The impact of technology scaling on lifetime reliability," IEEE The International Conference on Dependable Systems and Networks (DSN-04), June 2004.

[3] M. A. Alam, S. Mahapatra, "A comprehensive model of PMOS NBTI degradation," Microelectronics Reliability, vol. 45, no. 1, pp. 71-81, 2005.

[4] T. Chen, et al "CMOS device reliability for emerging cryogenic space electronics applications," IEEE International Semiconductor Device Research Symposium, 2005.

[5] G. De Geronimo, et al. "Front-end ASIC for Liquid Argon TPCs," 2010 IEEE Nuclear Science Symposium Conference Record, in press.

[6] See "Description and Estimates for the LBNE Experiment using a Liquid Argon Far Detector", LBNE Project Office, April 3, 2011, and other documents archived in LBNE docdb # 3547, v12.

4 Detector Performance

4.1 Calibration

One of the great advantages of the LAr TPC is the simplicity of the detector technology. The signal is generated by a well known electromagnetic process (the generation of ionization electrons by the passage of particles through LAr). The trajectory of the electrons is determined by the electric field in the drift region. Unlike room temperature TPCs, a LAr TPC does not rely on gas amplification to generate the signal so there are no gain variations in the detection medium. Signals generated on the induction plane wires are created by the nearby passage of ionization electrons. The gain stability of induction plane signals therefore depends on the stability of the bias voltage power supplies. Signals generated on collection plane wires are due to the charge deposited by ionization electrons and are not dependent on small variations of the collection plane voltage.

The recombination of ionization electrons is an important effect. The fraction of electrons that recombine depends on the electric field. This has been studied by the ICARUS collaboration [1] using stopping cosmic ray muons. The LAr40 drift field is the same as that used in ICARUS so the factor that scales the ionization at the wire to the energy deposited is the same. The ICARUS results can be confirmed by analyzing cosmic ray data in LAr1.

Calibration of a LAr TPC must therefore accomplish three things: 1) measure any distortions in the electron trajectories, 2) measure the loss of ionization electrons in the LAr, and 3) measure the gain of the electronics chain.

Electron trajectory distortions could be caused by defects in the field cage construction. A one-time calibration with through-going cosmic ray muons will be sufficient to determine if corrections are required.

The loss of ionization electrons depends on the LAr purity and is expected to vary over a several day time scale during the first few months of operation until the argon purity reaches a plateau. The calibration factor is $e^{-t/\tau}$ where t is the drift time and τ is the drift electron lifetime. The most accurate value of τ comes from the regular analysis of through-going cosmic

ray muons. A 0.3% uncertainty in τ will be achieved each day given the cosmic ray rate at the 800' level. It is unlikely that τ will vary throughout the drift volume considering the convective flow velocities in the LAr ($\sim$10 cm/s).

Changes in the electronics gain will be negligible considering the precision of ASIC devices and the temperature stability of the LAr ($<$0.1K). Each electronics channel can be tested by pulsing a charge calibration capacitor formed within the ASIC. The capacitor stability has been measured to be less than 0.5% between room temperature and 77K.

4.2   General Performance Metrics

Liquid Argon TPCs combine fine grain tracking with total absorption calorimetry to enable precision neutrino event detection in scalable neutrino detectors. The mm scale spatial resolution combined with recordable dE/dx provides excellent signal efficiency and background rejection for both beam and non-beam neutrino physics. This section outlines the assumptions used to determine the efficiencies and backgrounds for a variety of physics including neutrino oscillations, nucleon decay, and supernova searches.

4.2.1   Cosmogenic and Radioactive backgrounds

Unlike Cherenkov detectors, the imaging capabilities of LAr TPCs make it possible to build experiments much closer to the surface. For beam physics, a LAr TPC can collect data on the surface given the small time window in which the beam arrives (see, for example [2]). In order to use LAr detectors to search for nucleon decay, some overburden is necessary. Reference [3] calculates that a minimum overburden of 158m in an "under-the-hill" configuration is sufficient to retain an active fiducial mass of 28 kt for nucleon decay searches [5]. It is this physics goal which drives the location of LAr40 in the Reference design. This overburden also provides adequate coverage for supernova detection [5]. Radioactive backgrounds such as those produced from the decay of ^{39}Ar are too low in energy ($\sim$0.5 MeV) to impact the physics program reported here. For example, in Reference [5], the capabilities of detecting a supernova in LAr40 are determined based on a low energy threshold > 3 MeV, above the energy produced by such radioactive backgrounds.

4.2.2   Nuclear Effects

Some generic differences are expected between neutrino scattering in LAr vs a water Cherenkov detector (neglecting differences in detector efficiencies and acceptance):

- a 20% larger neutron content in LAr vs water

- a 10% free scattering component (H_2) component present in water that will have different kinematics due a lack of nuclear effects

- 5% differences in initial state nuclear effects in oxgyen vs. argon for inelastic interactions with the significant Q^2 dependence appearing in the regions x < 0.1 and x > 0.5

- 5 - 15% differences in initial state nuclear effects in oxygen vs. argon for QE scattering in different kinematic regions

- roughly a factor of two larger hadron final state interaction effects (e.g., pion absorption, charge exchange, etc.) in argon than in oxygen

To set the scale of final state interaction effects, approximately 30% of π^o's are estimated to be absorbed in oxygen and roughly 10% will charge exchange ($\pi^o p \rightarrow \pi^+ n, \pi^o n \rightarrow \pi^- p$). If a π^o does not leave the target nucleus intact, it cannot be mis-identified as an electron, thus removing such events as potential backgrounds in the ν_e appearance data. The π^o background is therefore expected to be smaller in argon vs. oxygen.

Similarly, pion absorption can create additional complications for ν_μ disappearance measurements, obscuring the ability to precisely measure the true energy of the event (especially if energy is 'lost' due to absorption or through rescattering to multiple final state particles with lower energies). The near detector will provide a very high statistics sample of ν_μ interactions that will provide a detailed understanding of final state interactions on argon. The MINOS experiment has successfully employed this technique on a target nucleus heavier than argon (iron).

4.3   Performance Metrics for $\nu_\mu \rightarrow \nu_e$ Oscillations

The main assumptions that drive the physics sensitivity for ν_e appearance physics are the signal efficiency for detecting electrons and the background rejection of NC π^0 events. As is the case with water Cherenkov detectors, intrinsic ν_e's in the beam remain an irreducible background.

The strength of the LAr TPC technique is not only the ability to use topology to differentiate ν_e from NC π^0 event classes, but also the unique ability to differentiate photons from electrons using the dE/dx capability of the detector. Using dE/dx, a single electron is distinguishable from a single photon by analyzing the first 2.5cm of each track before the shower has evolved. A single converted photon will have twice the deposited energy of a single electron as shown in Figure 4–1.

Other event categories are also distinguishable via their topology and dE/dx. Figure 4–2 shows an event with a distinct topology. Different particle tracks deposit dE/dx signatures according to their particle type (Figure 4–3). The calorimetry technique shown here was developed
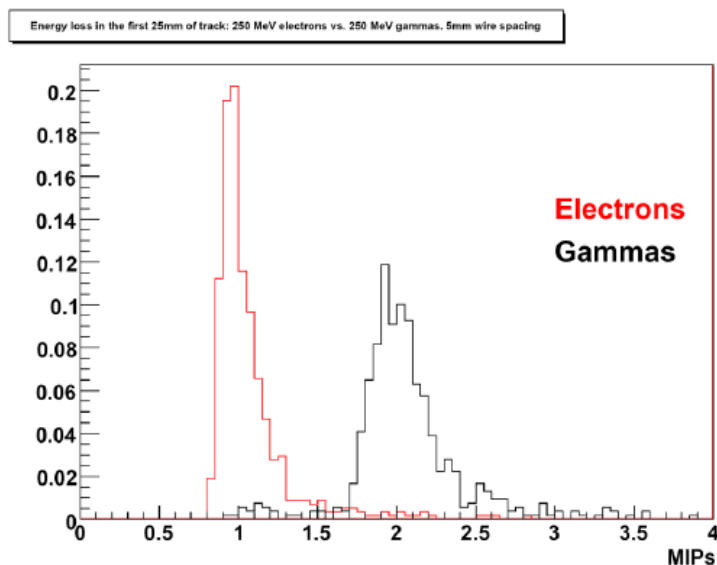
Figure 4–1: Energy deposited by simulated 250 MeV electrons and photons on a TPC with 5mm wire spacing. The gamma purity is 96%.

using LArSoft (Section 5.1) and can be applied on an event-by-event basis. Such calorimetry is being further developed for analysis of multiple event classes at a time.
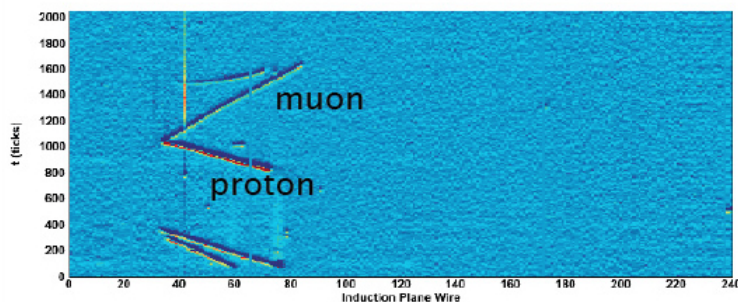

Figure 4–2: A candidate neutrino event from exposure of the ArgoNeuT LAr TPC in the NuMI beam at Fermilab.

The LArSoft fully automated simulation and event reconstruction is still under active development. Thus, the assumptions that have entered the neutrino oscillation sensitivity calculations (Section 5.2) are derived from existing Monte Carlo information and handscans, described next. These assumptions have also been tested to see how they impact the ultimate sensitivity of LBNE (Section 4.3.3).

4.3.1   Hand-Scanning Exercises

Tufts Hand-Scan: In developing a proposal presented to the NuSAG committee in 2005
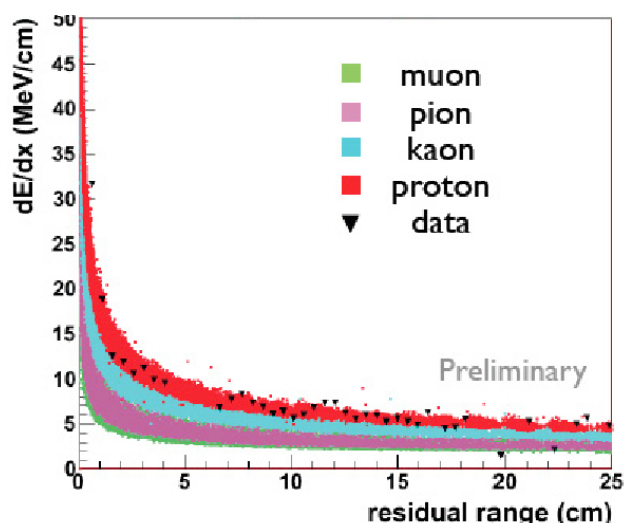
Figure 4–3: Estimated energy deposition versus range for various particle types in a liquid argon TPC. Overlaid in black is the response from proton tracks identified in ArgoNeuT neutrino events.

and 2006, a group of undergraduates, under the guidance of Hugh Gallagher, performed a hand-scan to determine efficiencies and background rejection for v_e appearance searches in LAr using the off-axis ME NuMI neutrino beam planned for NOvA. The analysis was based on a blind scan of 450 events. The events were generated using NEUGEN3 followed by a GEANT3 Monte Carlo which traced outgoing particles through a homogeneous volume of liquid argon. The students trained themselves on samples of 50 individual and mixed events. The individual event samples included v_e CC, v_μ CC, and v_μ NC events.

The students scored the events in the blind scan ranging from 1=background to 5=signal. The results of the hand scan are shown in Table 4–1 which summarizes the overall efficiencies and rejections for signal v_e's and NC backgrounds. The results of the study are described in more detail in Reference [6].

FNAL Hand-Scan: A second hand-scan was performed at Fermilab in the summer of 2009 to study v_e signal efficiency and background rejection using the NuMI low-energy off-axis beam at a distance of 800 km from FNAL. The Monte Carlo simulated a TPC with a 5mm wire pitch. The NEUGEN3 event generator was biased to increase the number of NC events in the scan data sample. A total of 5997 events were generated; 4468 NC, 1171 v_μ CC and 358 v_e CC. Events for scanning were pre-selected to require: 1) 10 MeV $< E_{visible} <$ 3.5 GeV, 2) at least one true electron within 2 (or 5) cm of the true interaction vertex, and 3) 100 MeV $<$ true electron energy $<$ 5 GeV. These cuts were chosen to reduce the scanning load and improve the statistical significance of the results. The hand-scan was performed by an undergraduate student who identified events as v_e CC, v_μ CC or NC.

Table 4–2 shows the results of the hand-scan of a total of 407 events. These yield an electron

Event Type		# events	# passing	selection efficiency	rejection efficiency
NC		290	4	-	0.99 ± 0.01
signal ν_e	CC	32	26	0.81 ± 0.07	-
Beam ν_e	CC	24	14	0.58 ± 0.10	-
Beam ν_e	NC	8	0	-	/
Beam $\bar{\nu}_e$	CC	13	10	0.77 ± 0.09	-
Beam $\bar{\nu}_e$	NC	19	0	-	/
ν_μ	CC	32	0	-	/
$\bar{\nu}_\mu$	CC	32	1	-	/

Table 4–1: Scan results for various event categories from the Tufts hand scan. The / symbol indicates samples where the event size was too small to draw meaningful conclusions.

	CC ν_e	CC ν_μ	NC
true CC ν_e	223	4	15
true CC ν_μ	1	21	6
true NC	25	11	101

Table 4–2: Scan results for various event categories from the FNAL hand-scan.

efficiency of 92%. Of the 137 NC events scanned, 18% were erroneously classified as ν_e CC. A NC rejection of 99.5% is implied if one makes the assumption that the NC identification efficiency is 100% if there are no photon conversions within a few cm of the interaction vertex.

4.3.1.1   Analysis from the T2K 2 km Proposal

An analysis of signal and background rejection was performed using the T2K beam analyzed for the proposed LAr TPC detector at the 2 km location [7]. Samples of 1,000 events of ν_e and NC π_0 interactions at energies of 250 MeV, 500 MeV, and 2 GeV were analyzed for electron efficiency and surviving pion fraction. The dE/dx in the first 2.4cm of each electron and gamma track left 90% of the ν_e events with a surviving pion fraction of 6.5% (3%) at 250 MeV (2 GeV). Folding in the results of a hand scan using event topology for further separation left a 0.2% surviving pion fraction with 90% ν_e efficiency.

4.3.1.2   Single Particle Energy Resolutions

Studies from ICARUS have estimated and measured single particle energy resolutions in liquid argon. The energy of an electromagnetic shower is shown to be $3\%/\sqrt{E(GeV)}$. Below

50 MeV, the energy resolution of electrons is $11\%/\sqrt{E[MeV]} + 2\%$ [8]. Figure 4–4 shows the reconstructed mass of π^o's collected during the ICARUS surface run at Pavia. The muon momentum resolution in LAr TPCs measured via multiple scattering is $\sim 12\%$ for muons with energies greater than 1 GeV [9].

Preliminary LArSoft results from 3D electromagnetic shower reconstruction is shown in Figure 4–5.
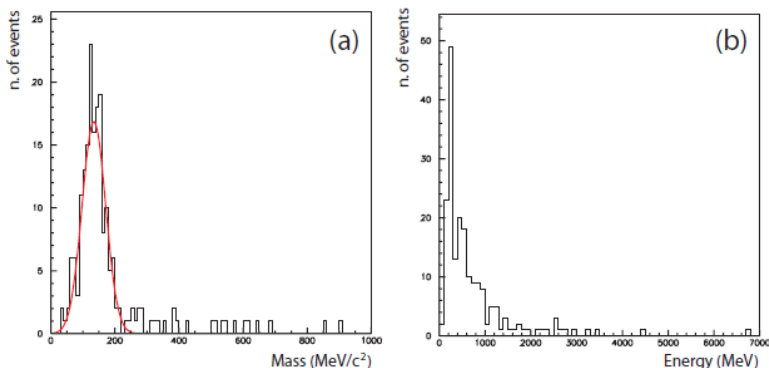

Fig. 9. (γ,γ) invariant mass (a) and energy (b) distributions for the sample of 196 real π^0 candidates. The average mass is $m_{\gamma\gamma} = 134.4 \pm 3.0$ MeV/c^2 ($\sigma = 36.7 \pm 3.4$ MeV/c^2). The mean value of the π^0 energy is $E = 707.7$ MeV.

Figure 4–4: Reconstructed mass of π^o's in the ICARUS detector, from Ref. [4].
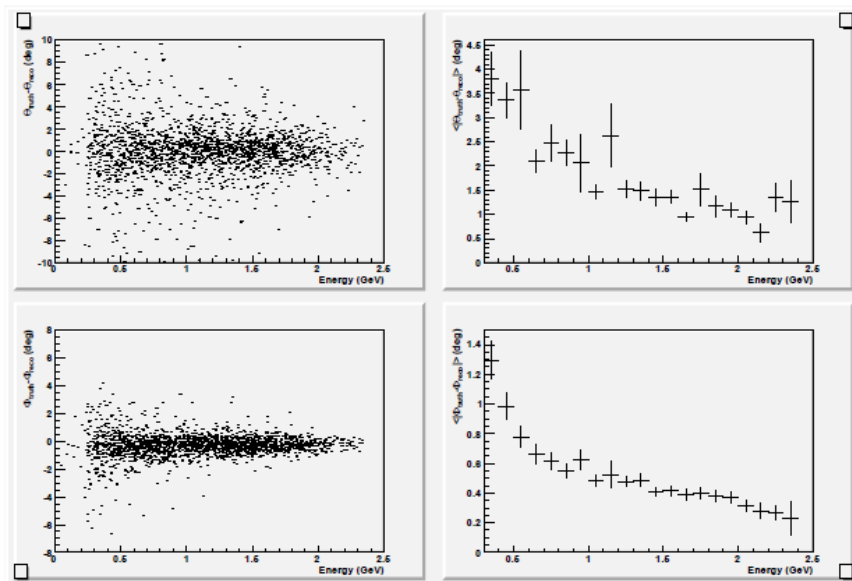
Figure 4–5: LArSoft reconstruction of the direction of simulated showers in ArgoNeuT. Upper left: Plot of $\theta_{truth} - \theta_{reco}$ vs true energy of the electron. Upper right: Profile histogram $|\theta_{truth} - \theta_{reco}|$ vs the true energy of the electron. Lower left: Plot of $\phi_{truth} - \phi_{reco}$ vs true energy of the electron. Lower right: Profile histogram of $\phi_{truth} - \phi_{reco}$ vs true energy of the electron.

channel	range	value chosen for LBNE sensitivities
ν_e CC efficiency	80-95%	80%
ν_μ NC π^0 surviving fraction	0.2-0.5%	1%
ν_μ CC mis-identification rate	0-0.3%	1%
other channels	0%	0%
electron energy resolution	$3\%/\sqrt{E(GeV)}$	$15\%/\sqrt{E(GeV)}$
muon energy resolution	$10-20\%/\sqrt{E(GeV)}$	$20\%/\sqrt{E(GeV)}$ (for E_ν)

Table 4–3: Estimated or measured range of efficiencies, backgrounds, and resolutions from the studies described above (middle column) and the value chosen for the LBNE neutrino oscillation sensitivity calculations described in Section 5.2 (last column).

4.3.2   Assumptions for Long-Baseline Oscillation Sensitivity Calculations

For the neutrino oscillation sensitivity calculations, information from the exercises reported above are used to set the detector efficiencies and background rejections. Table 4–3 shows the efficiencies, background rejection ranges, and single particle resolutions from the above studies along with the specific values chosen for the long-baseline oscillation sensitivity projections described in Section 5.2. The values chosen are conservative and reflect the uncertainties in the above studies. Reasonable variations in these efficiencies and background rejection values have been shown to have minimal impact on long-baseline oscillation physics sensitivity (Section 4.3.3).

These studies will be re-done when the LArSoft fully-automated simulation and event reconstruction is available. Nevertheless, the above studies taken in combination with the results from Section 4.3.3 give confidence in the detector performance values used in the LBNE ν_e appearance and ν_μ disappearance sensitivity calculations.

4.3.3   Dependence of Neutrino Oscillation Sensitivities on Efficiency Assumptions

In order to gauge how reliant the LBNE long-baseline neutrino oscillation performance is to assumptions to the level of signal and background achievable in a LAr TPC, a range of values were studied (Table 4–4). The assumed efficiency for selecting ν_e CC events was varied from a pessimistic value of 70% to an optimistic value of 95%, and the background levels correspondingly varied from 0.4% to 2.0%. This large span was chosen to represent varying degrees of LAr detector performance ranging from the most pessimistic to the most optimistic.

Figure 4–6 shows the 3σ sensitivity of a 34 kt fiducial LAr detector to θ_{13}, the mass hierarchy, and CP violation under these varying levels of signal and background. Varying the signal efficiencies and background levels by these amounts appears to have little impact on the oscilla-

ν_e efficiency	NC background	ν_μ CC mis-identification
70%	0.4%	0.4%
80%	1.0%	1.0%
95%	2.0%	2.0%

Table 4–4: Combinations of LAr reconstruction efficiencies and background rejection levels studied. The middle row represents the default values assumed for the projections presented in Section 5.2.

tion sensitivities given the already high level of ν_e efficiency and low NC background levels inherent in a LAr detector. Also note that the configuration with the best sensitivity appears to be that with the lowest signal efficiency and therefore lowest background levels (70% ν_e efficiency, 0.4% NC background). This suggests the potential for further optimizing the LAr oscillation sensitivities beyond those that are presented in Section 5.2. This will be the subject of future work.

4.4   Performance Metrics for Baryon Non-Conservation

Our studies addressing the capabilities of LAr at observing nucleon decay and other baryon number non-conservation processes have focused so far on two: $p \to \bar{\nu}K^+$ decay and $N\bar{N}$ oscillation. Based on decades of prior null-result searches, we know that these processes must be very rare. Since sensitivity is directly impacted by detection efficiency and the number of expected background events, the goal of these studies is to determine the ability of a LAr detector to distinguish signal from backgrounds. The work presented here is based on LArSoft (Section 5.1). Another early and important source of information on potential backgrounds will come from MicroBooNE, since measured backgrounds at the surface can be accurately extrapolated to greater depths.

The backgrounds to searches for baryon number violation will consist mostly of cosmic rays and atmospheric neutrinos. The minimum overburden required for a LAr detector will be determined by the detector's background rejection capability; note that the minimum overburden will not necessarily be the same for each decay mode. One of the advantages of a LAr TPC is that its tracking capability allows rejection of cosmic ray tracks with negligible loss of fiducial mass.

4.4.1   Proton decay to $\bar{\nu}K^+$

Sensitivity to the $\bar{\nu}K^+$ decay mode relies on the unambiguous identification of the 340 MeV/c K^+ and on rejection of backgrounds that mimic it. A simulation of a K^+ decay is shown in Fig-
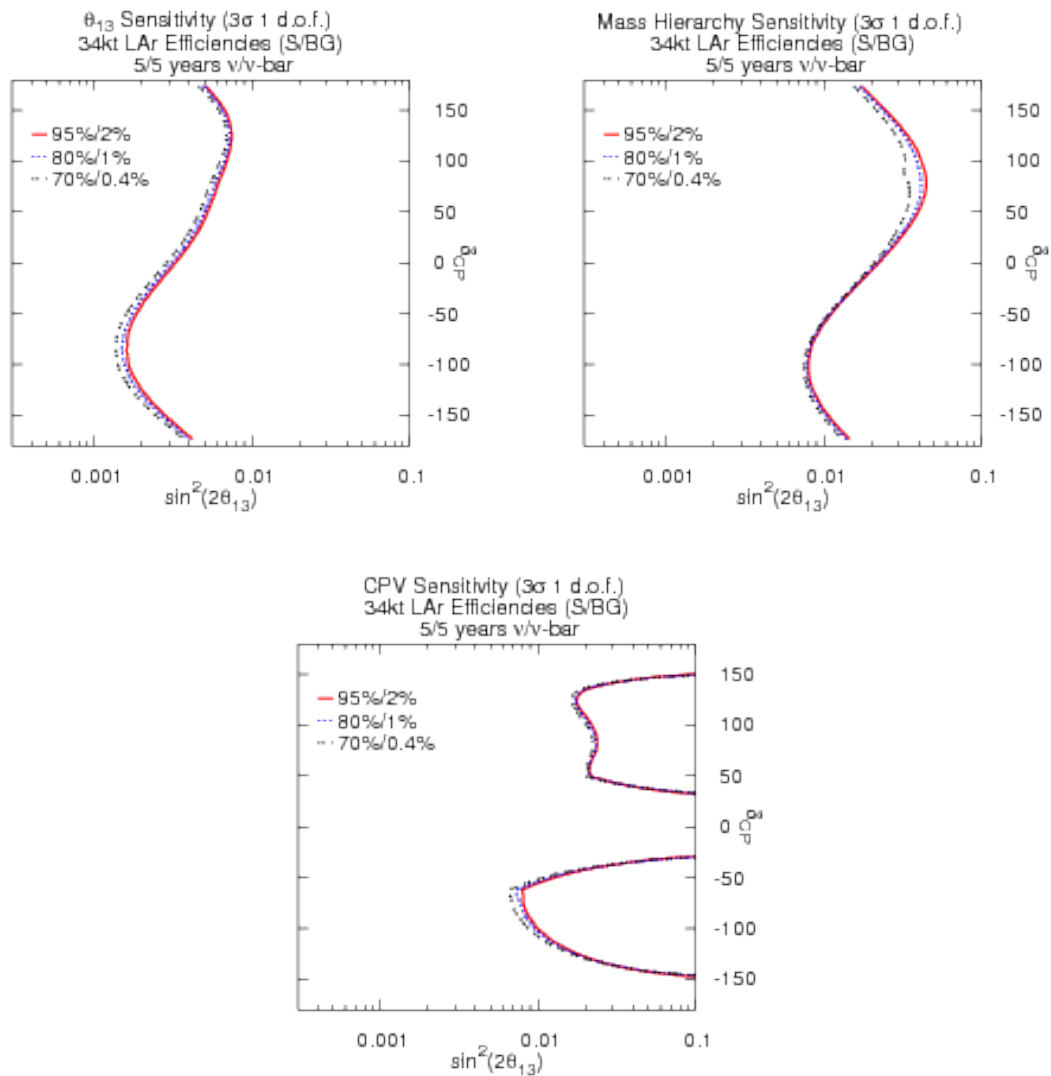
Figure 4–6: 3σ sensitivity of a 34 kt LAr TPC to $\theta_{13} \neq 0$ (left), the mass hierarchy (middle), and CP violation (right) for various detector performance assumptions (Table 4–4) assuming a normal mass hierarchy. Similar results are obtained for an inverted mass hierarchy.

ure 4–7, where the three individual particle tracks are clearly visible. The kaon deposits the equivalent energy deposition of ~2.5 MIPs at the beginning of its travel and ~9 MIPs as it comes to rest. The muon is a MIP at the beginning of its travel, providing a convenient in-event calibration. Calibration of the K^+ in other decay modes will rely on a signal generated by the photon detection system.

After the kaon is identified, the momentum will be determined by range (14cm at 340 MeV/c). The momentum uncertainty (~5%) will be largely dominated by the wire spacing of 5mm.

Using LArSoft simulations, a likelihood to distinguish K^+ from protons of similar range was constructed using the measured ionizations of tracks that were subdivided into segments. The clean separation of K^+ from protons can be clearly seen from Figure 4–8.
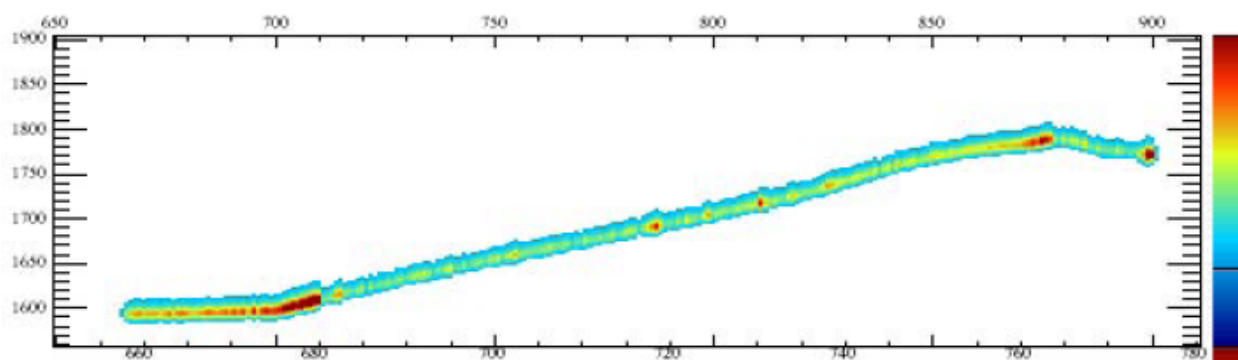

Figure 4–7: LArSoft simulation of $K^+ \to \mu^+ \to e^+$ decay in the MicroBooNE geometry. The drift time is along the vertical axis. The wire number is along the horizontal axis (3mm wire spacing).

The most serious background for this decay mode will result from cosmic muons undergoing deep inelastic scatter in the rock surrounding the detector and producing a neutral kaon that charge exchanges to a K^+ in the sensitive volume. At shallow depths, it will be necessary to have an active veto region that extends beyond the LAr detector to achieve sufficient rejection of this background, likely in conjunction with a fiducial mass reduction to eliminate candidates near side walls.

Two methods are proposed in Reference [3] to reject this background. Both Fluka and GEANT4 generators were used in the study. The results from Fluka and GEANT4 agreed within a factor of 1.3 when comparing the muon rates at ~200m underground. The neutron yields from Fluka and GEANT4 for cosmic ray spallation agreed within a factor of 2. The disagreement was a factor of 10 for the production of K^o's. The study authors used the higher Fluka yields in most of the analysis. A second conservative simplification in the study was that correlations between neutral particles entering the detector in time with charged particles were neglected. In practice, isolated K^o's would be rejected if they were near any charged tracks.

The conclusion of Reference [3] that is relevant for us is that a background of 0.1 events/year
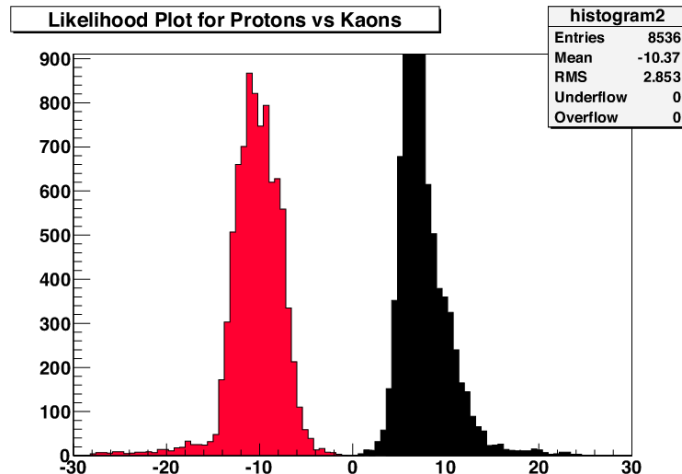
Figure 4–8: A likelihood distribution based on the ionization of a particle as measured in four range intervals, demonstrating the difference between protons (left red histogram) and K^+ (right black histogram).

is expected for the $\bar{\nu}K^+$ decay mode in a GLACIER-like detector if 1) it is located in an "under-the-hill" cavern with a minimum overburden of 158m, 2) it is surrounded by two levels of veto planes that extend 3m around the detector and 3) a 2.8m - 7.5m fiducial cut is made away from the detector walls. The fiducial cut range reflects the uncertainty between Fluka and GEANT4.

The fiducial cut in the LAr can be eliminated to a large extent by increasing the size of the surrounding veto. Fluka simulations show that the interaction length is 86cm for 500 MeV K^o's in LAr compared to the interaction length of 37cm in the Ellison rock formation on the 800L. Therefore, each meter of LAr provides shielding equivalent to 0.43m of rock. The required length of veto to largely eliminate the fiducial cut is therefore 3m + 0.43 x 7.5m = 6.2m. This is the basis for choosing the 7m veto length in the reference design.

Further studies using a cosmic ray generator implemented in LArSoft are in progress. In the near future, MicroBooNE and LAr1 will provide useful data to study cosmogenic K^+ background rejection more rigorously. The benefit of rejecting charged K's that have charged particles nearby will also be explored.

4.4.2 $N\bar{N}$ oscillation

$N\bar{N}$ oscillation will result in nearly 2 GeV of energy being released in the detector when the oscillated anti-nucleon annihilates with a nearby nucleon, typically producing a number of pions. Backgrounds arise mainly from atmospheric neutrino interactions which have multiple

pions in the final state. The significant energy release, together with its isotropic nature, will give strong kinematic constraints to help distinguish the signal from atmospheric backgrounds. In this search, the tracking capabilities of LAr again provide an advantage for signal identification and background reduction based on the event topology.

Initial studies to test the treatment of annihilations in LArSoft were done to compare the simulation of $p\bar{p}$ annihilations at rest with the existing body of experimental data; the characteristics of annihilation at rest are experimentally well-measured for anti-protons stopping in hydrogen. The average pion multiplicity of the LArSoft simulated events is shown in Figure 4–9, and an event display of a simulated event is shown in Figure 4–10. In the near-term, backgrounds will be investigated using LArSoft simulations of atmospheric neutrinos, and in the longer term, MicroBooNE will be a test bed for background studies using experimental data.
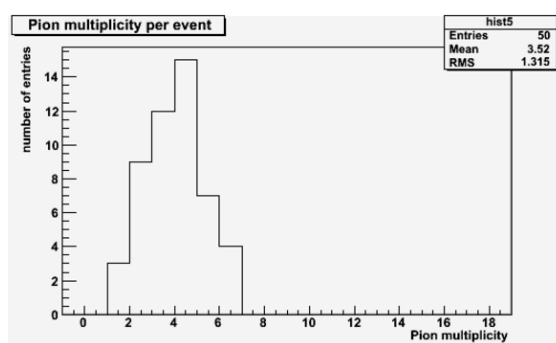

Figure 4–9: The pion (charged and neutral) multiplicity of $p\bar{p}$ annihilation events as simulated by LArSoft.
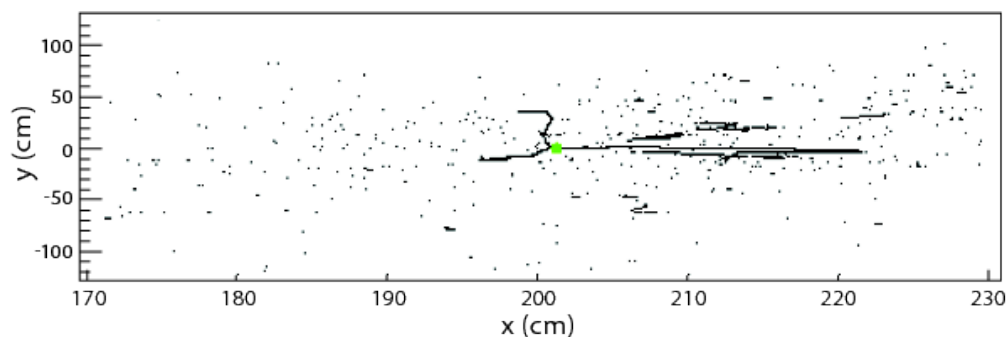
Figure 4–10: LArSoft simulated event, $p\bar{p}$ annihilation at rest.

4.4.3 Other decay modes

A LAr detector will also be sensitive to other nucleon decay modes that have not been discussed here. The detector's ability to discriminate electrons from photons will allow for excellent π^0 mass and energy reconstruction for decay modes with a π^0. The detection efficiencies for these modes are subject to an efficiency loss caused by nuclear effects that can absorb the pion or cause it to scatter or charge exchange.

4.4.4   Assumptions for Nucleon Decay Sensitivity

The sensitivity for a detector configuration is determined by the detector mass, efficiency, expected background, and running time. For the purpose of generating sensitivity curves in Section 5.8, we calculate the 90% C.L. lifetime limit one would publish after a given exposure under the assumption that the number of detected events exactly equals the number of background events, and the background is subtracted.

4.5   Performance Metrics for Supernova Burst

LAr detectors are primarily sensitive to electron neutrinos in a supernova burst. The sensitivity to physics associated with a supernova burst improves with larger active mass, and since "increasing exposure" is not possible because the burst is a one-time event, the total detector mass ultimately determines the sensitivity. At the moment we have very little information on the nature of spallation backgrounds in argon, on the potential quality of signal tagging in LAr using gammas, and on background reduction in a LAr detector. These issues may be relevant for low-statistics bursts resulting from core collapses beyond 10 kpc.

4.5.1   Assumptions for Supernova Burst Sensitivity

The event rate estimates for LAr discussed in Section 5.9 assume a detection threshold of 5 MeV. It is also assumed that a photon trigger is not required for detection of supernova events, i.e., that suitable triggering will be provided either from charge collection or from an external trigger. The energy resolution used is from Reference [8], $\sigma_E = 11\%/\sqrt{E} + 2\%$.

Bibliography

[1] [ICARUS Collaboration], NIM A 523 , 275 (2004)

[2] "Recommendations to the Department of Energy and the National Science Foundation on a Future U.S. Program in Neutrino Oscillations", submitted by the Neutrino Scientific Assesment Group, `http://www.science.doe.gov/hep/hepap_reports.shtm`.

[3] A. Bueno et al., JHEP 0704, 041 (2007).

[4] A. Ankowski *et al.* [ICARUS Collaboration], Acta Physica Polonica B 41, 103 (2010).

[5] M. Bass *et al.*, LBNE Physics Working Group Report, arXiv:1110.6249v1 [hep-ex]

[6] "A Large Liquid Argon Time Projection Chamber for Long-baseline Off-Axis Neutrino Oscillation Physics with the NuMI Beam", Submitted to the NuSAG committee, 2006, FERMILAB-FN-0776-E.

[7] "A Proposal for a Detector 2 km Away from the T2K Neutrino Source", `http://www.phy.duke.edu/~cwalter/nusag-members/`.

[8] S. Amoruso et al. [ICARUS Collaboration], Eur. Phys. J. C33, 233 (2004).

[9] A. Ankowski et al. [ICARUS Collaboration], Eur. Phys. J. C48, 667 (2006).

5   Physics Analysis

Liquid argon TPCs are ideally suited for studying neutrino interactions and probing new physics via detection of rare processes. The following sections detail the ability of a large-scale LAr TPC to reconstruct neutrino interactions, perform long-baseline oscillation physics, search for nucleon decay, and detect supernova neutrinos.

5.1   Analysis Tools

Understanding of the potential sensitivity of a large-scale Liquid Argon TPC to various physics signatures has been facilitated by the concurrent development of software tools as part of the overall U.S. LArTPC development program.

The LArSoft software package has been developed in this context, and is now being applied to the simulation, reconstruction, and analysis of data. LarSoft is a general purpose package for LAr TPC's and is currently in use by the ArgoNeuT and MicroBooNE collaborations. It was designed to ensure that any LArTPC could make use of its algorithms as long as each experiment supplied a properly formatted description of the detector geometry.

LArSoft is built on the Analysis and Reconstruction Toolkit (ART) framework designed and maintained by the Computing Enabling Technologies (CET) group of the Fermilab Computing Division. This framework is designed for use by Intensity Frontier experiments and the CET group is providing significant support to ensure the framework meets the needs of the client experiments: currently, mu2e, g-2, LArSoft and NOνA. Using this framework means that support for I/O, job configuration, and memory management is supplied by the CET group, freeing LArSoft developers to focus on simulation, reconstruction, and analysis. The Intensity Frontier experiments are in the process of developing an MOU with the Computing Division to formalize the support of the ART framework for the lifetime of the various experiments using it. A major benefit of using the ART framework is that it allows experimenters working on multiple Intensity Frontier experiments to learn a single software environment, making them more productive on each experiment.

The LArSoft simulation facilities interface with standard external packages for event generation and energy deposition. For example, the creation of neutrino interactions is done by GENIE while the simulation of cosmic rays is handled by CRY. The simulation of energy deposition by particles crossing the detector volume is done by Geant4. As the readout electronics are generally different for each experiment, each one must provide a detailed simulation of the electronics. At present, the complete simulation chain is available for both ArgoNeuT and Microboone. While the final development of the LBNE simulation chain is awaiting the detailed description of the LBNE geometry and readout electronics, interim code allows semi-realistic analyses to be carried out for now.

The reconstruction algorithms of LArSoft benefit from the experience of multiple experiments. Each LArTPC provides essentially the same basic information after accounting for small detector differences due to the readout electronics. Thus, algorithms developed for one experiment can be directly used by another, as long as the differences in geometry are properly accounted for in the algorithms. The reconstruction chain proceeds in the following steps: i) the raw energy depositions (digits) are calibrated, ii) hits are formed from the regions containing signal on each calibrated digit, iii) hits are grouped into clusters, iv) clusters are grouped into prongs and the prongs are determined to be either tracks or showers, v) vertices are located using the prongs, and finally, vi) vertices are associated into events. The analysis then proceeds using the reconstructed events. The LArSoft reconstruction chain is nearly complete through the stage of creating prongs.

The reconstruction algorithms in LArSoft are based on several aspects of photographic analysis developed over the past decade. The algorithm to cluster groups of energy depositions together is based on the point density scanning algorithm of Ester, Kriegel, Sander, & Xu, Proceedings of Second International Conference on Knowledge Discovery and Data Mining, Portland, OR (1996). Figure 5–1 shows the result of this algorithm for a pair of electromagnetic showers recorded with the collection plane of ArgoNeuT. The different colored regions correspond to distinct reconstructed clusters. As can be seen in the figure, the algorithm does a very good job of associating reconstructed hits together. Another algorithm borrowed from image processing techniques is the algorithms to find end points in each readout plane are based on the Harris corner finding technique (JINST 5, P07006 (2010)).

5.2   Neutrino Oscillations

Long-baseline neutrino oscillation physics is the primary focus of LBNE. Precise measurement of $\nu_\mu \rightarrow \nu_e$ and $\bar{\nu}_\mu \rightarrow \bar{\nu}_e$ oscillations over a large distance and wide energy range will allow:

- an unprecedented measurement of leptonic CP violation through measurement of the CP violating phase, δ_{CP} (assuming $\theta_{13} \neq 0$),
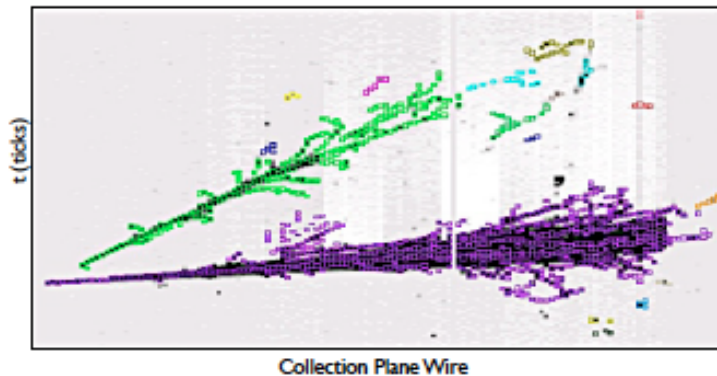
Figure 5–1: Collection plane view of a data event in ArgoNeuT with two electomagnetic showers, with colors depicting results from the energy cluster reconstruction algorithm.

- a determination of the neutrino mass hierarchy, i.e, whether the mass ordering is normal: $\Delta m_{31}^2 > 0$ or inverted: $\Delta m_{31}^2 < 0$ (assuming $\theta_{13} \neq 0$), and

- a more precise measurement of θ_{13} or extension of the limit in the case of non-observation.

Figure 5–2 shows the expected $\nu_\mu \rightarrow \nu_e$ oscillation probability over a 1300 km baseline for different values of θ_{13} and δ_{CP} and for both mass hierarchies. Shown in black is the un-oscillated spectrum of CC ν_μ events highlighting the wide energy range of the LBNE beam. The LBNE beam will include a new neutrino beamline located at Fermilab that utilizes a 700 kW 120 GeV proton source from the Fermilab Main Injector [1,3]. This beam was designed to maximize the number of oscillated ν_e events appearing at the 1st oscillation maximum and implies an overall beam delivery of 7.3×10^{20} POT per year.
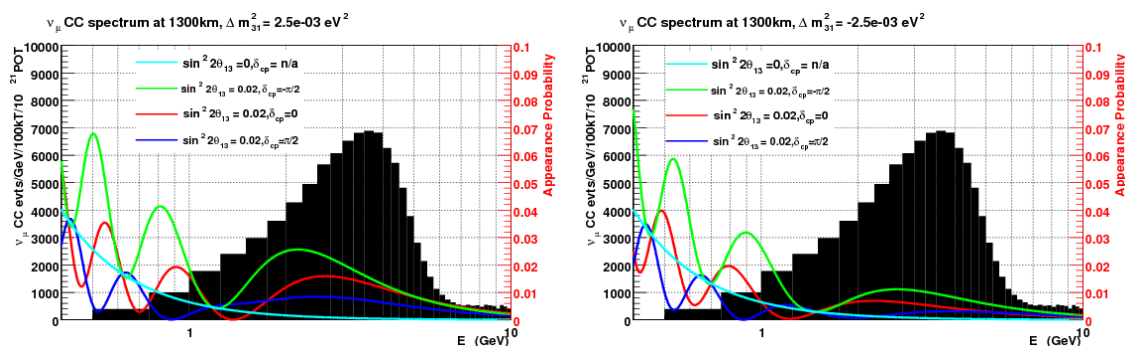

Figure 5–2: The $\nu_\mu \rightarrow \nu_e$ oscillation probability for the LBNE to Homestake baseline of 1300km for different mixing parameters with normal (left) and inverted (right) mass hierarchies. The un-oscillated CC ν_μ spectrum from a candidate LBNE beam is shown as the solid black histogram.

The following sections further detail the specific capabilities of an LBNE LAr TPC to measure $\sin^2 2\theta_{13} \neq 0$, the mass hierarchy, and CP violation with this candidate LBNE beam. The sensitivities are all estimated assuming a 1300 km baseline from Fermilab to Homestake. The detector performance parameters assumed for these calculations are detailed in Chapter 4 and were generated using GLoBES [2].

In addition to precision measurements of the unknown neutrino mixing parameters accessible through $\nu_\mu \to \nu_e$ oscillations (θ_{13}, the mass hierarchy and δ_{CP}), LBNE will enable precision measurements of the atmospheric neutrino oscillation parameters: Δm^2_{32} and θ_{23} for both neutrinos and anti-neutrinos with a precision that exceeds current experiments. LBNE is also uniquely suited to observe ν_τ appearance with sufficient statistics to test the 3-flavor model of neutrino oscillations and to extend the search for non-standard interactions. Such capabilities are also detailed below.

5.3 $\nu_\mu \to \nu_e$ Oscillations

A large LAr detector operating at a long baseline will be able to significantly extend the sensitivity to $\nu_\mu \to \nu_e$ oscillations. Such an experiment will be capable of improving the 3σ sensitivity to the mass hierarchy and CP violation by almost an order of magnitude beyond current neutrino oscillation experiments. Figure 5–3 and Table 5–1 give the expected event rates for ν_e appearance measurements in a 34-kt LAr detector for both normal and inverted mass hierarchies. The appearance rates are higher for the normal mass hierarchy in the case of neutrinos and for the inverted hierarchy in the case of anti-neutrinos. From Figure 5–3, we also see the effect of the δ_{CP} phase: larger neutrino rates are expected for negative phases (both normal and inverted hierarchies), while larger anti-neutrino rates are expected for positive phases. By exploiting the wide-band neutrino beam and the differences in the neutrino and anti-neutrino spectra observed at these large distances, oscillation parameter degeneracies can be uniquely resolved in LBNE and separate information on θ_{13}, the mass hierarchy, and CP violation can be obtained.

The sensitivities to determining θ_{13}, the neutrino mass hierarchy, and CP violation are summarized in the following sections. All projections assume the same 700 kW beam and a 1300 km baseline from the LBNE beam at Fermilab to the location of the Homestake mine.

5.3.1 Sensitivity to θ_{13}

Based on current projections, upcoming reactor and accelerator-based experiments should be able to distinguish θ_{13} from zero at the 3σ level for $\sin^2 2\theta_{13}$ values down to 0.02 before LBNE is in operation [4]. Figure 5–4 (left) shows the sensitivity of LBNE to $\theta_{13} \neq 0$. The results are dependent on both the value of δ_{CP} and the mass hierarchy. As can be seen, the sensitivity is better for normal mass hierarchy unless $\delta_{CP} = 45 - 180^o$, in which case the sensitivity is better for
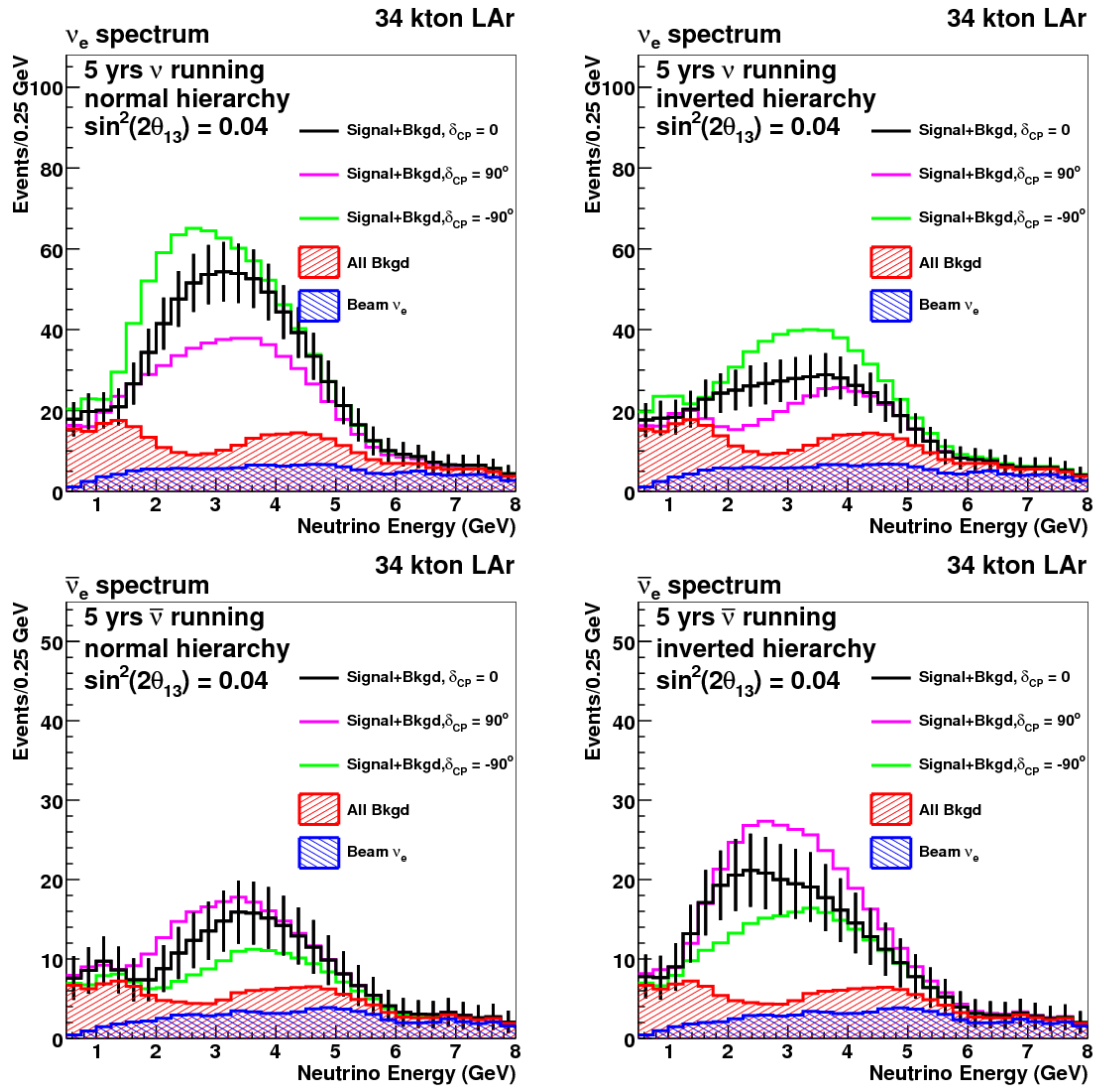
Figure 5–3: The expected ν_e spectra in a 34 kt LAr detector assuming $\sin^2 2\theta_{13} = 0.04$ and 5 years of neutrino (top) and anti-neutrino (bottom) running in a 700 kW beam [3] for normal (left) and inverted (right) mass hierarchies. The black points assume $\delta_{CP} = 0$ while the pink and green lines are for $\delta_{CP} = \pm 90^0$. The different background contributions are indicated by the hatched histograms with intrinsic ν_e events shown in blue and the total background contribution including intrinsic ν_e, NC, and mis-identified ν_μ CC events in red. In the case of anti-neutrino running, the signal and background distributions explicitly include an additional contribution from neutrinos in the beam.

	LAr (ν mode)	LAr ($\bar{\nu}$ mode)
Normal mass hierarchy:		
oscillated $\nu_e + \bar{\nu}_e$	497	112
beam $\nu_e + \bar{\nu}_e$	326	168
NC	81	34
mis-identified CC	162	52
Inverted mass hierarchy:		
oscillated $\nu_e + \bar{\nu}_e$	212	261
beam $\nu_e + \bar{\nu}_e$	329	167
NC	81	34
mis-identified CC	162	52

Table 5–1: Number of ν_e and $\bar{\nu}_e$ events expected in a 34-kt LAr detector at 1300 km in 5 years each of neutrino and anti-neutrino running in a 700 kW beam [3]. Rates have been integrated over the region from $0.5 - 60$ GeV. Like Figure 5–3, this assumes $\sin^2 2\theta_{13} = 0.04$ and $\delta_{CP} = 0$.

inverted mass hierarchy.

Of course, the sensitivity of LBNE to determining a non-zero value of θ_{13} also increases with longer exposure. Figure 5–4 (right) shows the sensitivity in a LAr detector as a function of exposure at the 3σ level for $\delta_{CP} = 0$. LBNE can probe $\sin^2 2\theta_{13}$ down to the 10^{-3} level with reasonable detector and beam assumptions. For example, with a standard 340 kt-yr exposure and normal mass hierarchy, a LAr detector is sensitive to $\sin^2 2\theta_{13} \neq 0$ at 3σ down to a $\sin^2 2\theta_{13}$ value of 0.008 for 100% of all possible δ_{CP} values (Figure 5–4 (left)). The sensitivity is slightly worse for an inverted mass hierarchy.

5.3.2   Mass Hierarchy

While the primary goal of upcoming neutrino oscillation experiments such as T2K and NoνA is discovery of θ_{13}, they may also provide information on the mass hierarchy (Figure 5–5 (right)) and CP violation (Figure 5–7 (right)) but only if θ_{13} is quite large. The results would not be compelling however even with a 2x - 3x increase in beam power. It is clear that an experiment like LBNE is needed to take the next step in physics reach [4]. Figure 5–5 (left) shows LBNE's projected sensitivity to the mass ordering as a function of θ_{13} and δ_{CP} for a 34-kt LAr detector at 1300 km.

To get a sense for how this changes with detector mass and/or beam power, Figure 5–5 (right) shows the sensitivity for resolving the mass hierarchy as a function of exposure. With an exposure of 340 kt-yrs, a LAr detector can resolve the mass hierarchy at 3σ for 100% of all δ_{CP} values for a $\sin^2 2\theta_{13}$ value down to 0.05. The sensitivity improves with larger exposures.
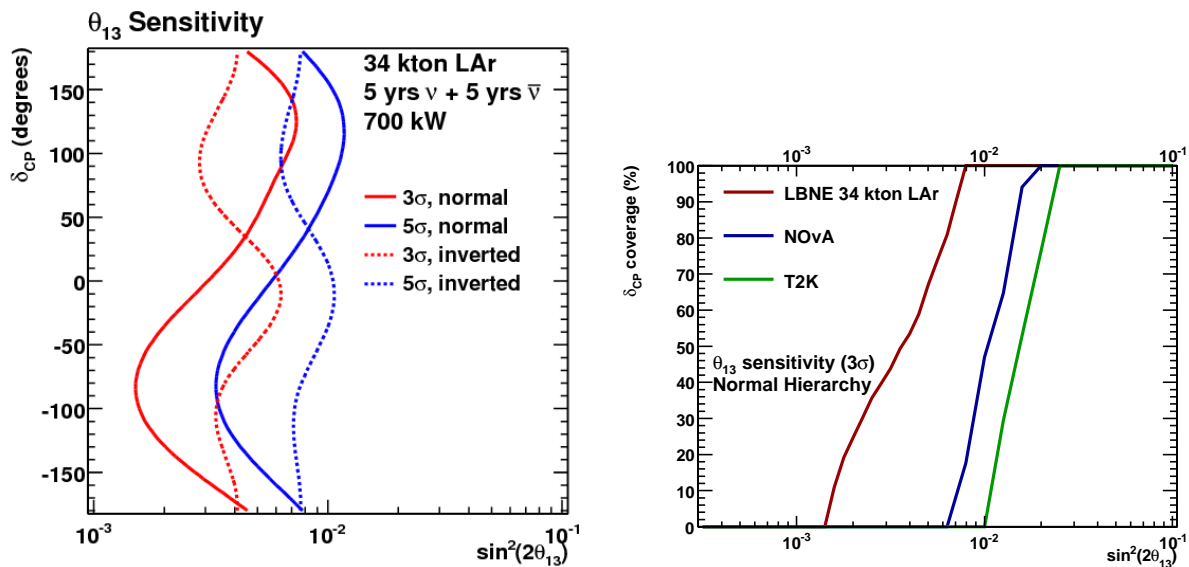
Figure 5–4: Left: 3σ (red) and 5σ (blue) sensitivity of LBNE to $\sin\theta_{13} \neq 0$ as a function of δ_{CP} for a 34 kt LAr detector assuming 5+5 years of ν and $\bar{\nu}$ running in a 700 kW beam [3]. Here, the discovery reach for $\sin^2 2\theta_{13}$ is defined as the minimum value of $\sin^2 2\theta_{13}$ for which LBNE can rule out $\sin^2 2\theta_{13} = 0$ at the 3σ and 5σ levels. Right: Sensitivity of LAr40 compared to NoνA (3+3 years of $\nu+\bar{\nu}$ running in a 700 kW beam) and T2K (3+3 years of $\nu+\bar{\nu}$ running in a 770 kW beam). T2K and NoνA curves are GLoBES model projections.

5.3.3   CP Violation

LBNE will have unrivaled sensitivity to determining whether or not CP is violated in the neutrino sector. Figure 5–6 (left) summarizes the CP violation reach of LBNE for a 700 kW beam and a 34-kt LaAr detector operating at 1300 km. A LAr detector can make a 3σ discovery of CP violation for 50% of all δ_{CP} values for $\sin^2 2\theta_{13}$ values down to 0.03 assuming an exposure of 340 kt-yrs. This reach increases substantially with exposure.

Figure 5–6 (right) shows the resolution on LBNE's ability to measure δ_{CP} as a function of exposure. Assuming a normal mass hierarchy, $\sin^2 2\theta_{13} = 0.01$, and $\delta_{CP} = 0$, a LAr detector can measure δ_{CP} to within $\pm 19°$ (at 1σ) in a 340 kt-yr exposure. From Figure 5–6 (right), we see that higher mass (or equivalently, higher beam power) provides a rapid improvement in resolution in the early years of running.

5.3.4   Summary of ν_e Appearance Capabilities

Figure 5–7 summarizes the overall discovery reach of LBNE to determine $\theta_{13} \neq 0$, the mass hierarchy, and CP violation as a fraction of δ_{CP} coverage for a 34-kt LAr detector in 5+5 years of combined neutrino and anti-neutrino running in a 700 kW beam [3].
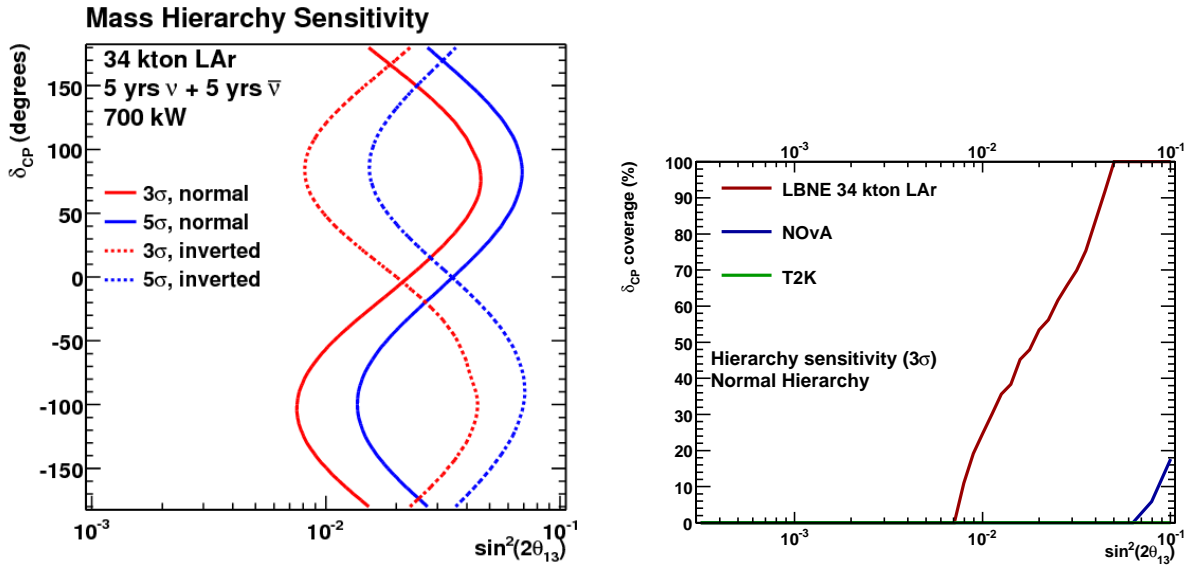
Figure 5–5: Left: resolution of the mass hierarchy for LAr40 assuming 5+5 years of ν and $\bar{\nu}$ running in a 700 kW beam [3]. To the right of the curves, the normal (solid) or inverted (dashed) mass hierarchy can be excluded at the 3σ (red) or 5σ (blue) level for the indicated values of true $\sin^2 2\theta_{13}$ and δ_{CP}. Here, the mass hierarchy discovery reach is defined as the minimum value of $\sin^2 2\theta_{13}$ for which the wrong hierarchy can be excluded for a given value of δ_{CP}. Right: Sensitivity of LAr40 compared to NoνA (3+3 years of $\nu+\bar{\nu}$ running in a 700 kW beam) and T2K (3+3 years of $\nu+\bar{\nu}$ running in a 770 kW beam). The NoνA curve is a GLoBES model projection. T2K has no sensitivity at 3σ this region of $\sin^2 2\theta_{13}$.

LBNE is sensitive to non-zero θ_{13} (at the 3σ level) down to $\sin^2 2\theta_{13} = 0.0044$ for a single 17-kt LAr module operating for 10 years (5+5 years $\nu+\bar{\nu}$) and down to $\sin^2 2\theta_{13} = 0.0030$ for 34 kt operating in this same time. This assumes $\delta_{CP} = 0$ and normal mass hierarchy. As one might expect, the 34 kt configuration reaches a sensitivity almost a factor of $\sqrt{2}$ higher than the 17 kt case; of course, higher beam power could also provide the same sensitivity in the case of a single module. Additionally, the 170 kt-yr exposure provides a 25° measurement of δ_{CP}, whereas an 18° accuracy can be achieved in 340 kt-yrs. This assumes normal mass hierarchy, $\sin^2 2\theta_{13} = 0.01$, and $\delta_{CP} = 0$.

Table 5–2 summarizes the sensitivity of a LAr detector in LBNE to measure non-zero $\sin^2 2\theta_{13}$, the mass hierarchy, and CP violation assuming a run time of 5 years each in neutrino and antineutrino modes at 700 kW for both one and two LAr modules.

5.3.5   Impact of Beam Upgrades

The possibility of a more intense beam, of up to 2.3 MW, could significantly improve the experiment's sensitivity to ν_e appearance physics, with no changes to the detector necessary.
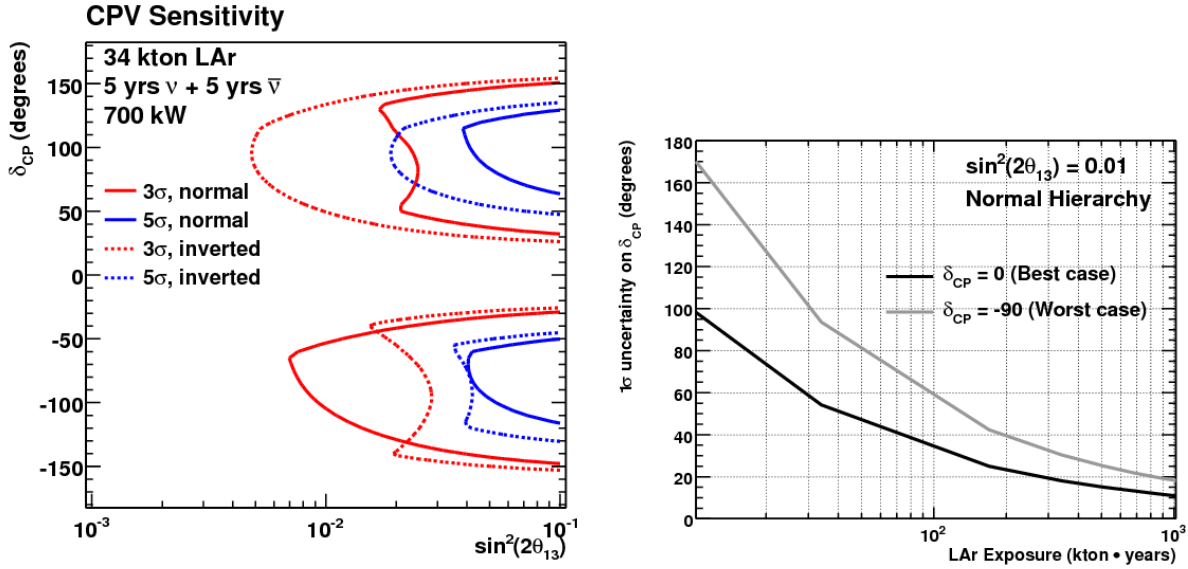
Figure 5–6: Left: 3σ (red) and 5σ (blue) sensitivity of LBNE to CP violation for a 34 kt LAr detector assuming 5+5 years of ν and $\bar{\nu}$ running in a 700 kW beam [3]. Curves are shown for both normal (solid) and inverted (dashed) mass hierarchies. Here, we define the CP violation discovery potential as the range of δ_{CP} values as a function of $\sin^2 2\theta_{13}$ for which one can exclude the CP conserving solutions for $\delta_{CP} = 0^o$ and $\delta_{CP} = 180^o$. Right: 1σ resolution on the measurement of δ_{CP} in a LAr detector assuming $\sin^2 2\theta_{13} = 0.01$ and normal mass hierarchy. Projections for both $\delta_{CP} = 0$ (black) and $\delta_{CP} = -90^0$ (gray) are separately shown.

In Figures 5–8 and 5–9, we show the improvements to θ_{13} sensitivity, the mass hierarchy sensitivity, and to CP violation coverage with a 2 MW beam. As can be seen, for CP violation, the 50% coverage point moves downward to near $\sin^2 2\theta_{13} \approx 0.01$ in this scenario.

5.4 ν_μ and $\bar{\nu}_\mu$ Disappearance

In addition to the ν_e appearance measurements, LBNE will also be able to provide precise measurement of the atmospheric oscillation parameters through observation of both ν_μ and $\bar{\nu}_\mu$ disappearance. The most precise constraints on the atmospheric mass splitting is currently set by the MINOS experiment while the most precise constraints on the atmospheric neutrino mixing angle is currently set by the Super-Kamiokande experiment.

In the coming years, next generation experiments, such as T2K and NOνA, will be able to push beyond the current values and obtain even more precise measurements of these parameters. For example, with an exposure of 3.75 MW $\times 10^7$ sec, T2K hopes to achieve a 1% (4%) measurement of $\sin^2 2\theta_{23}$ (Δm^2_{32}) [6]. For maximal mixing and after 6 years of $\nu + \bar{\nu}$ running, NOνA plans to measure $\sin^2 2\theta_{23}$ to $\sim 0.3\%$ and Δm^2_{32} to $\sim 1\%$ [7].
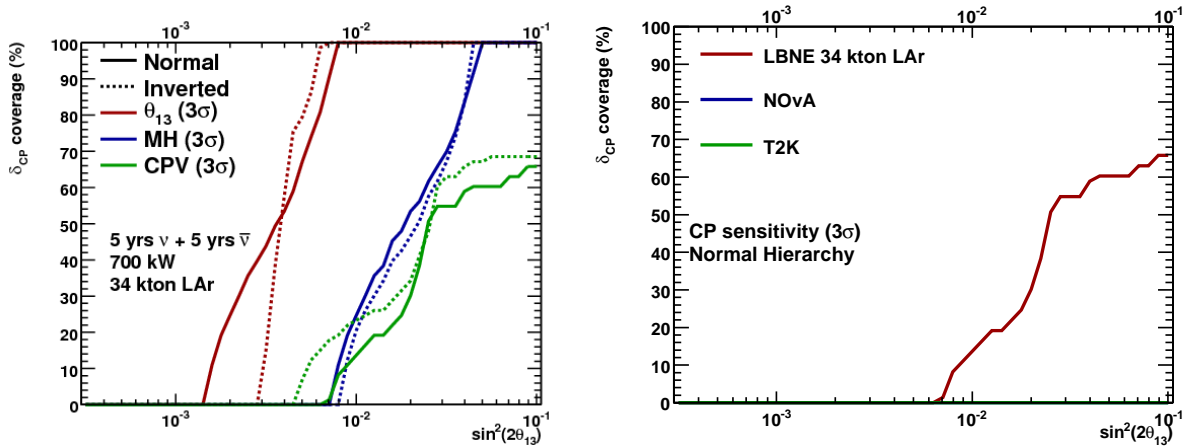
Figure 5–7: Left: 3σ discovery potential of LBNE for determining $\sin^2 2\theta_{13} \neq 0$ (red), the mass hierarchy (blue), and CP violation (green) as function of $\sin^2 2\theta_{13}$ and the fraction of δ_{CP} coverage. Here the fraction of δ_{CP} reflects the fraction of all true values of δ_{CP} for which the corresponding quantity can be measured. Sensitivities are shown for both normal (solid) and inverted (dashed) mass hierarchies for a 34-kt LAr detector in 5+5 years of $\nu+\bar{\nu}$ running in a 700 kW beam [3]. Right: 3σ discovery potential of LBNE, NoνA (3+3 years of $\nu+\bar{\nu}$ running in a 700 kW beam) and T2K (3+3 years of $\nu+\bar{\nu}$ running in a 770 kW beam). Note that Noνa and T2K have no sensitivity to CP violation at 3σ for this range of $\sin^2 2\theta_{13}$ using GLoBES model projections.

LBNE will also provide a sensitive test of the atmospheric oscillation parameters through its measurement of ν_μ and $\bar{\nu}_\mu$ disappearance. One advantage of the long baseline in LBNE is that the multiple oscillation pattern in the spectrum will be clearly detectable. This should offer some advantage when it comes to reducing systematics. Figure 5–10 and Table 5–3 show the expected ν_μ and $\bar{\nu}_\mu$ event rates at the LBNE far detector site for a 34 kt LAr detector. The statistics and the size of the expected signal are large.

Using the assumptions from Chapter 4, Figure 5–11 shows the expected resolutions on $\sin^2 2\theta_{23}$ and Δm^2_{32} achievable in LBNE as a function of exposure. As can be seen, rapid gains are made in the first years of running. In 5 years of neutrino running and for maximal mixing, sub-% level measurements of Δm^2_{32} and $\sin^2 2\theta_{23}$ are possible (at 1σ) with a 34 kt LAr detector. Unprecedented measurements of these parameters in the anti-neutrino disappearance channel are also possible at the 1% level assuming a similar exposure.

Table 5–4 summarizes the physics reach of an LBNE LAr detector to ν_μ and $\bar{\nu}_\mu$ disappearance parameters for exposures of both a single 17-kt module and two 17-kt modules to 5 years of 700 kW beam.

	$\sin^2 2\theta_{13} \neq 0$	Mass Hierarchy	CP violation
170 kt-yrs LAr	0.010	0.06	0.10
340 kt-yrs LAr	0.008	0.05	0.03

Table 5–2: Sensitivity comparisons for 170 kt-yr and 340 kt-yr exposures of a LAr detector (e.g., 17 kt and 34 kt of LAr in 5+5 years of $\nu + \bar{\nu}$ running at 700 kW). These numbers represent the value of $\sin^2 2\theta_{13}$ where a 3σ determination of $\sin^2 2\theta_{13} \neq 0$, the sign of Δm^2_{31}, and CP violation can be made for 100% of the possible values of δ_{CP}. For CP violation, the values are quoted for 50% of possible δ_{CP} values. All assume a normal mass hierarchy.
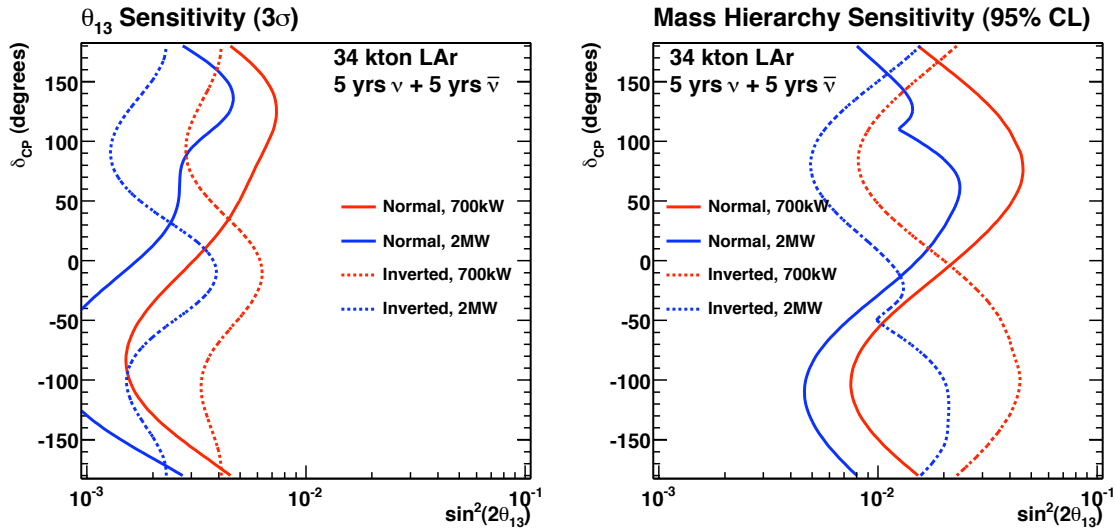

Figure 5–8: The 3σ discovery reach for $\sin^2 2\theta_{13}$ (left) and the 95% C.L. sensitivity to mass hierarchy (right), under the assumption of beam powers of 2MW (blue) and 700kW (red).

5.5 θ_{23} Octant

Current experimental results tell us that θ_{23} is near maximal ($\sin^2 2\theta_{23} > 0.96$ at 90% CL [9]); however, there exist two solutions of θ_{23} for a given set of measured oscillation parameters, known as the θ_{23} octant ambiguity. Determining whether θ_{23} is greater or less than $\pi/4$ will tell us whether the third neutrino mass eigenstate couples more strongly to ν_μ or ν_τ neutrinos. Figure 5–12 displays the capability of LBNE to resolve the θ_{23} octant with a 34-kt LAr detector. With a 700 kW beam, LBNE is able to resolve the θ_{23} octant degeneracy for $|\theta_{23}|$ values less than 40° at 90% CL and 90% of δ_{CP} values if $\sin^2 2\theta_{13}$ is greater than 0.075.
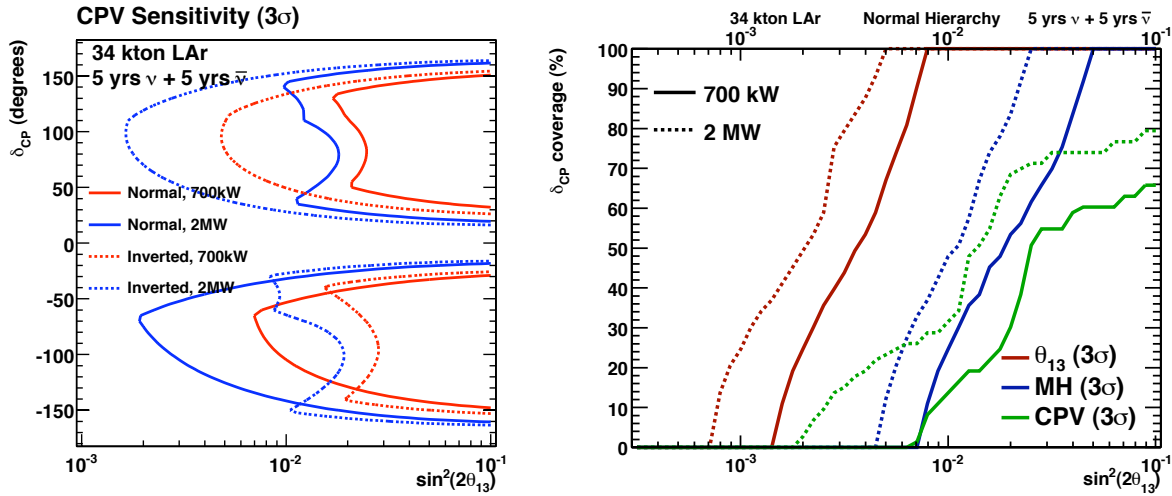
Figure 5–9: Left plot: Phase coverage for 3σ discovery of CP violation, under the assumption of beam powers of 2MW (blue) and 700kW (red). Right plot: a version of Figure 5–7 for the case of normal hierarchy, comparing sensitivities to θ_{13} (red), mass hierarchy (blue) and CP violation (green) for 2 MW (dashed) and 700 kW (solid) beam power scenarios.

5.6 ν_τ Appearance

The LBNE baseline of 1300 km will be longer than any long-baseline experiment in current operation. As a result, the oscillation probability occurs at higher energies which are favorable to $\nu_\mu \to \nu_\tau$ appearance. In this respect, LBNE has a unique ability to observe oscillations between all three neutrino flavors with significant statistics in a single experiment.

Observation of atmospheric neutrino oscillations consistent with ν_τ appearance have been previously reported by the Super-K collaboration [10]. We are currently estimating the significance with which ν_τ appearance can be established in LBNE. In a 34-kt LAr detector operating at 1300 km in the candidate 700 kW beam [3], LBNE expects to observe 189 ν_τ CC events resulting from $\nu_\mu \to \nu_\tau$ oscillations in 5 years of neutrino running. By comparison, OPERA expects to collect a total of 11 ν_τ CC events in 5 years of running in the CNGS beam [11]. Both assume a Δm^2 value of 2.5×10^{-3} eV^2.

LBNE will be able to collect sizable ν_τ samples in argon. For example, a 34-kt LBNE LAr detector expects to collect 3-6 times the annual rate of $\nu_\tau \to e^- \nu_\tau \bar{\nu}_e$ decays than ICARUS [12]. These ν_τ rates in LBNE could, of course, significantly improve with higher energy beam tunes. This can be accomplished, for example, by moving the proton target further upstream of the LBNE horn. However, even with the lower energy configuration most suitable for studying $\nu_\mu \to \nu_e$ oscillations, the ν_τ rates are competitive and complementary to what will be achieved in other experiments.

	LAr (ν mode)	LAr ($\bar{\nu}$ mode)
No oscillations:		
CC signal	26,040	10,248
NC background	51	23
wrong-sign background	–	3,110
With oscillations:		
CC signal	8,489	3,182
NC background	51	23
wrong-sign background	–	1,791

Table 5–3: Number of ν_μ and $\bar{\nu}_\mu$ events expected in a 34 kt LAr detector for 5 years each of neutrino and anti-neutrino running in a 700 kW beam [3]. Rates have been integrated over the region from $0 - 10$ GeV. The signal samples are assumed to be ν_μ ($\bar{\nu}_\mu$) CC events in the case of neutrino (anti-neutrino) mode running. Wrong-sign backgrounds refer to ν_μ events in the anti-neutrino mode beam.

	$\delta(\sin^2 2\theta_{23})$ (ν)	$\delta(\Delta m^2_{32})$ (ν)	$\delta(\sin^2 2\theta_{23})$ ($\bar{\nu}$)	$\delta(\Delta m^2_{32})$ ($\bar{\nu}$)
85 kt-yrs LAr	0.008	0.024×10^{-3} eV^2	0.012	0.035×10^{-3} eV^2
170 kt-yrs LAr	0.006	0.016×10^{-3} eV^2	0.009	0.025×10^{-3} eV^2

Table 5–4: 1σ resolution on the measurement of ν_μ (and $\bar{\nu}_\mu$) disappearance parameters in LBNE assuming an exposure of 85 and 170 kt-yrs of LAr (e.g., 17 kt or 34 kt of LAr in 5 years of ν (or $\bar{\nu}$) running at 700 kW). Values are quoted for $\sin^2 2\theta_{23} = 1.0$.

5.7   New Physics Searches

In addition to precision measurements of standard three-flavor neutrino oscillations, LBNE is also well-positioned for new physics searches in the neutrino sector. The experiment is sensitive to non-standard interactions and active-sterile neutrino mixing, provided that these effects are not too weak.

Theories beyond the standard model can induce new Lagrangian operators that couple neutrinos to normal matter in non-standard ways. These non-standard interactions (NSI) manifest themselves as 4-fermion operators, either of the charged current (CC) or neutral current (NC) type. NC NSI can be understood as non-standard matter effects that are visible only in a far detector operating at a sufficiently long baseline. This is where LBNE has a unique advantage compared to other neutrino experiments (except atmospheric neutrino experiments which are, however, limited by systematic effects).

Figure 5–13 shows the NSI discovery reach of LBNE. We conclude from the figure that LBNE will be able to improve model-independent bounds on NSI in the $e - \mu$ sector by a factor of 2, and in the $e - \tau$ sector by an order of magnitude. Bounds on non-standard effects in the $\mu - \tau$
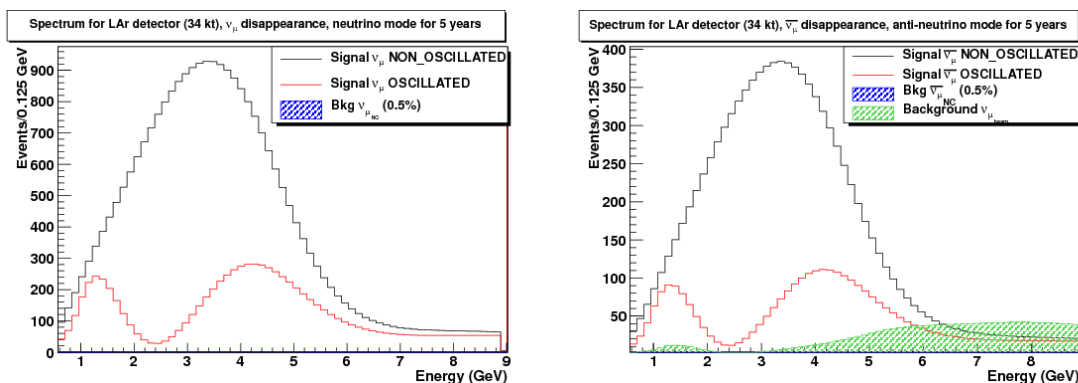
Figure 5–10: Number of events expected with (red) and without (black) oscillations as observed by a 34 kt LAr detector in 5 years of neutrino (left) and 5 years of anti-neutrino (right) running in a 120 GeV 700 kW beam [3]. In the current set of assumptions, a ν_μ CC sample is used for the signal channel. NC backgrounds are also plotted but are too small to be visible. In the case of anti-neutrino running, there is an additional contribution from ν_μ events which is taken into account and shown in green.

sector are already quite strong because of the sensitivity of atmospheric neutrino experiments, but LBNE may be able to also improve some of these bounds. In any case, the LBNE bounds will be more robust than the ones derived from atmospheric neutrinos.
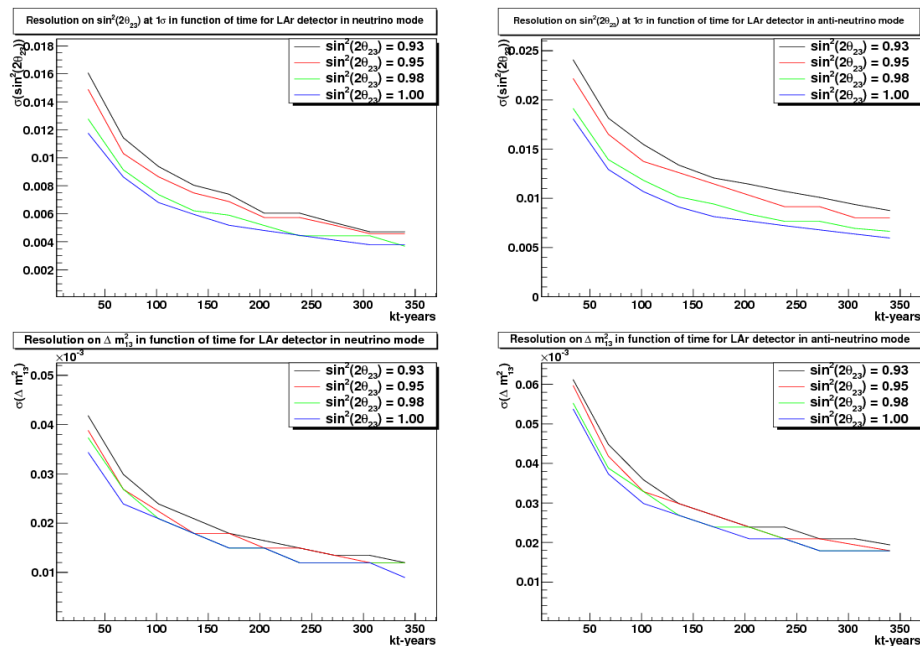
Figure 5–11: Resolution on $\sin^2\theta_{23}$ (top) and Δm^2_{13} (bottom) as a function of exposure that could be achieved in LBNE at the 1σ level for a LAr detector running in neutrino (left) and anti-neutrino (right) mode assuming a 700 kW beam [3].
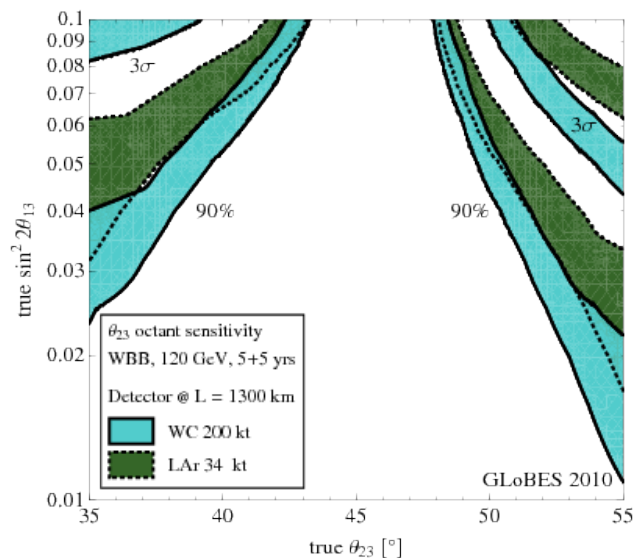

Figure 5–12: Sensitivity of LBNE to resolve the θ_{23} octant degeneracy for 5+5 years of $\nu+\bar{\nu}$ at 700 kW and normal mass hierarchy. The green band shows the results for a 34 kt LAr detector. The width of the bands corresponds to the impact of different true values for δ_{CP}, ranging from a 10% to 90% fraction of δ_{CP}. In the region above the bands, the determination of the θ_{23} octant is possible at 90% CL (lower bands) and 3σ (upper bands).
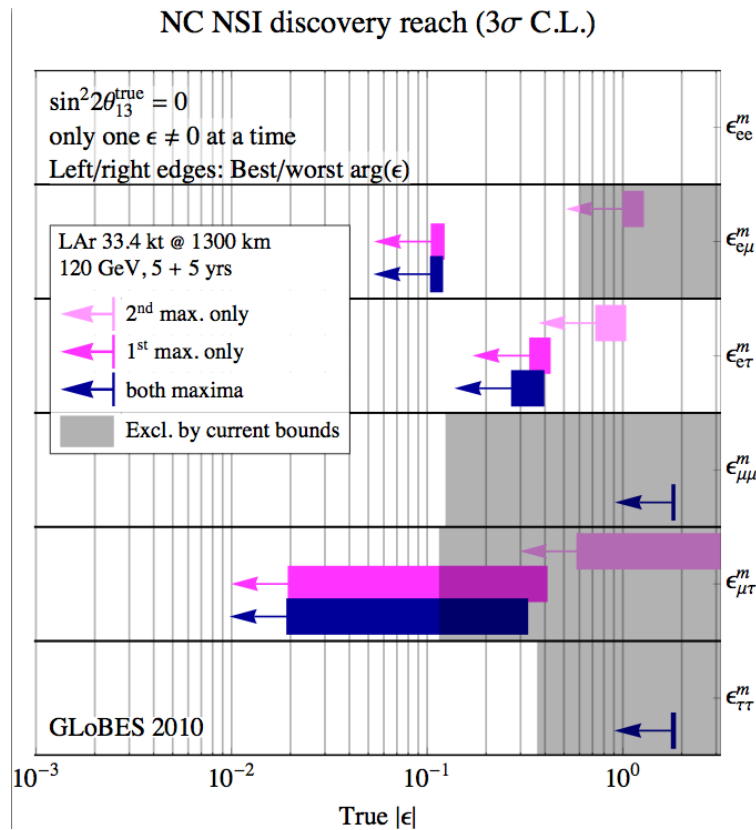
Figure 5–13: NSI discovery reach in a 34 kt LAr detector operating in a 700 kW beam at a baseline of 1300 km. The left and right edges of the error bars correspond to the most favorable and the most unfavorable values for the complex phase of the respective NSI parameters. The gray shaded regions indicate the current model-independent limits on the different parameters at $3\,\sigma$ [13,14,15]. For many of them, existing limits are extremely weak.

5.8   Nucleon Decay Physics

Proton decay, bound neutron decay, and similar processes such as di-nucleon decay and nucleon-antinucleon oscillation test the apparent but unexplained conservation law of baryon number. These decays are already known to be rare based on decades of prior searches, all of which have been negative. If measurable event rates or even single candidate events are found, one immediately concludes that they must have proceeded via unknown virtual processes based on physics beyond the standard model. The impact of demonstrating the existence of a baryon number violating process would be profound. Further motivation and the historical context of proton decay experiments is discussed in reference [1].

The search for $N\overline{N}$ oscillation is a compelling area of study that can address the question of whether the observed B-L symmetry is broken beyond the standard model. If it is broken, observation of $N\overline{N}$ oscillation would directly probe the mass scale of the symmetry breaking. Studies are underway to understand the sensitivity of a LAr detector to $N\overline{N}$ oscillations, but it is expected that the high pion multiplicity of these events will provide a strong handle for event identification.

From the body of literature, two nucleon decay modes emerge that dominate our experimental design: $p \rightarrow e^+\pi^0$ and $p \rightarrow K^+\bar{\nu}$. The second mode is dominant in most supersymmetric grand unified theories (SUSY GUTs), which also often favor several other modes involving kaons in the final state. The decay mode with a charged kaon is notable because it presents the unique opportunity for a liquid argon TPC to detect it with extremely high efficiency. This is because the momentum of the kaon will result in high ionization density which can be compared to the range of the kaon, not to mention the unique final states of K^+ decay that should be fully reconstructed. Although the $p \rightarrow e^+\pi^0$ mode can be detected in LAr with reasonable efficiency and low background (45% efficiency with a background rate of 0.1 events per 100 kt-years, according to Bueno et al. [16]), the resulting background subtracted limit at 90% CL is 2.6×10^{34} years for a 500 kt-year exposure. For a ten year run of a 51 kt LAr detector starting in 2020, the limit would not exceed the projected limit of 3×10^{34} years that will be achieved by continuing to run Super-K until 2030. There is no reason not to search for this mode if a LAr detector is built, but we do not consider $e^+\pi^0$ to be a critical physics topic for a 51 kt or smaller LAr detector; the remainder of this case study will therefore focus on the $p \rightarrow K^+\nu$ decay mode.

5.8.1   Sensitivity of Reference Configurations

The experimental requirements of the search for proton decay can be found in the basic formula for the partial lifetime τ for branching fraction B:

$$\frac{\tau}{B} = \frac{N_0\,\Delta t\,\epsilon}{n_{obs} - n_{bg}}, \tag{5.1}$$

where N_0 is the number of nucleons exposed, Δt is the exposure time, ϵ is the detection efficiency, n_{obs} is the observed number of events, and n_{bg} is the estimated number of background events. To measure τ/B, one would like the numerator to be as large as possible, which calls for the largest possible exposure of nucleons as well as the highest possible efficiency.

The sensitivity for a detector configuration is determined by the detector mass, efficiency, expected background, and running time, following Eq. 5.1. For the purpose of generating sensitivity curves, we calculate the 90% C.L. lifetime limit one would publish after a given exposure under the assumption that the number of detected events exactly equals the number of background events, and the background is subtracted. The efficiency and background estimates are shown in Table 5–5.

The lifetime limit is calculated for the 90% confidence level based on the Poisson processes with background method from the 1996 Review of Particle Properties [17]. This method does not take into account systematic uncertainty; doing so typically weakens these limits by 20%.

| Mode	Efficiency	Liquid Argon Background Rate (evts/100 kt-y)
$p \to e^+\pi^0$	45%	0.1
$p \to \nu K^+$	97%	0.1

Table 5–5: Efficiency and background numbers used for sensitivity calculations. The liquid argon numbers come from the paper by Bueno et al. [16].

Proton decay to $\bar{\nu}K^+$

Shown in Figure 5–15 is the projected sensitivity for a liquid argon TPC of various masses. The efficiency and background rates are taken from Bueno et al. [16]. The high efficiency for $p \to \nu K^+$ is a classic strong point in favor of liquid argon. Such a proton decay event signature would be highly described by such a detector, with a unique range and ionization level for the charged kaon.

The kaon has a momentum of 340 MeV neglecting nuclear effects and has a range of 14cm in LAr. The Fermi momentum, K_f, in the argon nucleus should be similar to that in Ca^{40} for which measurements have been made; $K_f = 250$ MeV. This is not significantly larger than K_f for an oxygen nucleus (225 MeV). The kaon will undergo only elastic collisions during its passage out of the argon nucleus since the momentum is less than ~800 MeV (see Figure 5–14).

The charged kaon will decay at rest to fully reconstructible final states, for example, a subsequent muon with no other particle, indicating $K^+ \to \mu^+\nu$ (predominant, with 65% branching fraction) should have a muon with momentum reconstructed at 236 MeV/c. Therefore a high efficiency in excess of 90%, with very low background, is quite plausible.

16   *41. Plots of cross sections and related quantities*
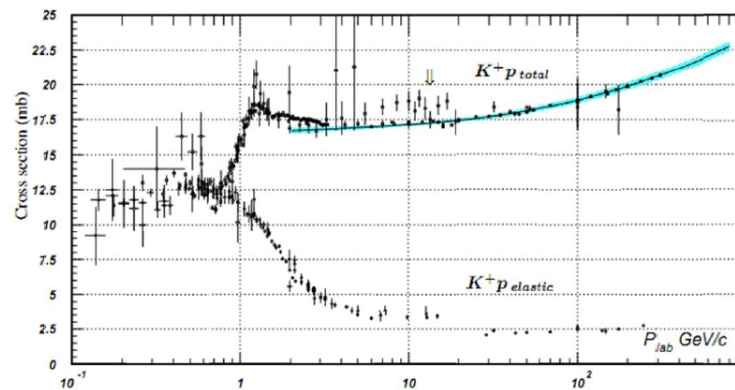
Figure 5–14: K^+p elastic and total cross section.

The most serious background is cosmogenic neutral kaons undergoing charge exchange in the sensitive volume. These could result in the appearance of a charged kaon, mimicking proton decay if the K^+ had the right momentum. This background process could be effectively studied by measuring the rate of such events in momentum sidebands. In any case, a fiducial mass reduction is anticipated to eliminate such events, by cutting out candidates near the side walls. In the Bueno et al. paper [16], several different overburden and active veto scenarios were considered, with fiducial cuts as much as 6 meters from the wall, resulting in fiducial mass reductions ranging from 66% to 90%. For the sensitivity curves plotted in Figure 5–15 we will take a generic value of 70%. This corresponds to a 2 meter cut from the sidewalls of the planned LBNE detector, reducing the volume from 14×15×71 meters^3 to 14×11×67 meters^3. At shallow depths, a key detector element required to allow this fiducial restriction is an active muon tracking veto that extends wider than the LAr detector itself. This is used to track nearby cosmic ray muons that could produce neutral kaons or neutrons.

One 21-kiloton (active mass) LAr module, having a 17 kt fiducial mass for long-baseline neutrinos, is taken to have a 14 kt fiducial mass for this proton decay mode if at shallow depth, but the full 17 kt at the 4850-ft level.

5.8.2   Conclusions

The case for nucleon decay rests on either discovering a small number of events or extending existing lifetime limits after an extensive search by Super-Kamiokande. To characterize the power of an additional search using LBNE detectors, we may look at the improvement factor in the lifetime limit after running for ten years.

The improvement factor in the lifetime limit is largest for the 33 kt LAr reference configuration, and of course improves with added detector mass. Assuming that the high performance
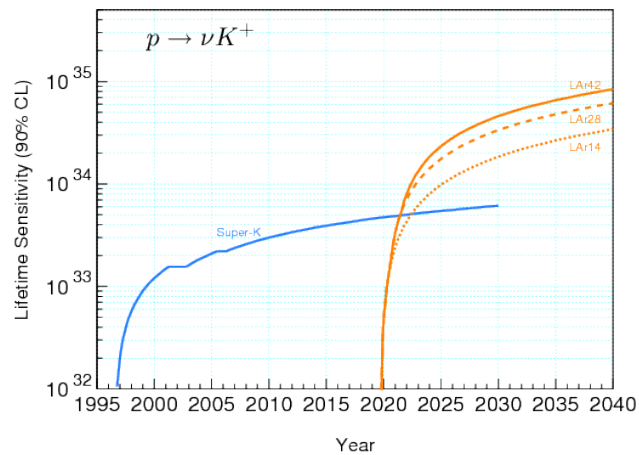
Figure 5–15: Proton decay lifetime limit for $p \to \nu K^+$ as a function of time for Super-Kamiokande compared to 60 kilotons total, 42 kt fiducial, of a LAr TPC starting in 2019. The LAr detector modules are assumed to commission 20 kt each year for the first three years; the limits from the partial detector fiducial masses of 14 and 28 kt (LAr40 reference design) are indicated with dashed lines. The limits are at the 90% C.L., calculated for a Poisson process including background assuming the detected events equals the expected background.

characteristics projected for a large LAr TPC are realized, LAr40 could achieve an improvement factor of 6 to 7 on the lifetime limit for $p \to K^+ \nu$ after 10 years and could continue to do well with further exposure, having accumulated a modest background estimate of less than one-half event after that time.

5.9 Supernova Neutrino Burst Detection

A nearby core collapse supernova will provide a wealth of information via its neutrino signal (see [18,19] for reviews). The neutrinos are emitted in a burst of a few tens of seconds duration, with about half in the first second. Energies are in the few tens of MeV range, and luminosity is divided roughly equally between flavors. An observed high-statistics core collapse neutrino signal will shed light on a variety of physics and astrophysics topics: from measuring the neutrino mass hierarchy and θ_{13} mixing angle, to observing the development of the explosion in the core of the star, to probing the equation of state of matter at nuclear densities, to constraining physics beyond the Standard Model.

In contrast to the SN1987A, for which only 19 neutrinos were observed, the detectors currently on the drawing board would register thousands or tens of thousands of interactions from the burst. The exact type of interactions depends on the detector technology: a water-Cherenkov detector would be primarily sensitive to the electron anti-neutrinos, while a liquid argon detector has an excellent sensitivity to electron neutrinos. It would be extremely valuable to detect both the neutrinos and anti-neutrinos with high statistics, as the oscillations occur very differently in the two channels.

5.9.1 Supernova Neutrino Interaction Rates

The predicted event rate from a supernova burst may be calculated by folding expected neutrino differential spectra with cross sections for the relevant channels, and with detector response. We have chosen to do the event rate calculation by using the GLoBES software [2]. We employ only the front-end rate engine part of GLoBES, and not the oscillation sensitivity part. GLoBES takes as input fluxes, cross sections, "smearing matrices," and post-smearing efficiencies. The smearing matrices incorporate both interaction product spectra and detector response.

We have examined several flux models. We assume fluxes at 10 kpc, which is just beyond the center of the Galaxy: event rates just scale as $1/R^2$, shown in Figure 5–16. We consider here the "Livermore" model [20], and the "GKVM" model [21], described in more detail in reference [1]. We consider also "Duan" fluxes [22,23], which represent only a single late time slice of the supernova burst and not the full flux.

The cross sections for interactions in argon are standard inputs to GLoBES; more details of the cross sections may be found in reference [1]. The uncertainties for the recent calculations are at around the 10-20% level. For the CC channels we have included energy deposition of the leading lepton; in the detector response, we also incorporate additional visible energy from de-excitation gammas (these gammas may also possibly help to tag the ν_e or $\bar{\nu}_e$ channels, although we made no assumptions about such tagging). We found no information in the literature about resulting excited levels for the NC interactions, so for the moment this channel is not included
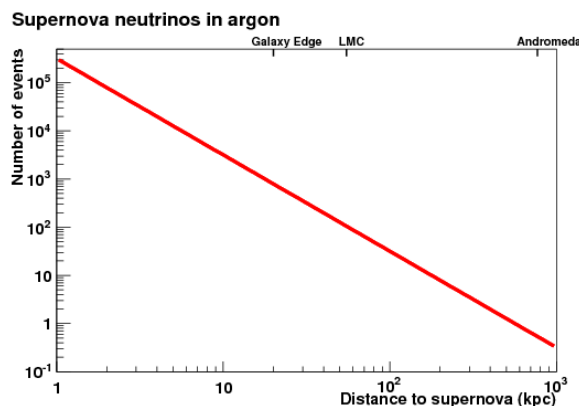
Figure 5–16: Approximate number of events detected in 30 seconds as a function of distance to the supernova in 34 kt of LAr.

in the study, even though event rates may be fairly large. Table 5–6 gives a table of event rates for two models. Note here that primary sensitivity is to the ν_e component of argon.

Channel	Events, "Livermore" model	Events, "GKVM" model
$\nu_e + {}^{40}\mathrm{Ar} \rightarrow e^- + {}^{40}\mathrm{K}^*$	2308	2848
$\bar{\nu}_e + {}^{40}\mathrm{Ar} \rightarrow e^+ + {}^{40}\mathrm{Cl}^*$	194	134
$\nu_x + e^- \rightarrow \nu_x + e^-$	296	178
Total	2798	3160

Table 5–6: Event rates for different models in two 17 kt modules of LAr.

5.9.2   Mass Hierarchy Sensitivity

There will likely be significant and observable imprints of oscillation parameters on the observed spectrum of burst supernova neutrino events. For oscillation sensitivity, ability to measure and tag the different flavor components of the spectrum is essential.

Figure 5–17 compares event rates for normal and inverted hierarchy in argon, for a particular spectrum (a late time slice, not the full flux). Although some information about the hierarchy is present in the water spectrum (see Ref. [25]), the difference between the hierarchies is quite dramatic in the observed mostly-ν_e argon spectrum.

In an attempt to understand the sensitivity of the LAr detector configuration to mass hierarchy, we have determined the minimum statistics for which normal hierarchy is distinguishable from inverted hierarchy. At this time, we cannot evaluate the full statistical sensitivity because the only available flux with oscillation signatures is the Duan multi-angle spectrum [22], which represents a late-time fraction of the total flux. We find that for a water Cherenkov detector, approximately 3500 events are required to distinguish the hierarchy at 3σ; for LAr, only 550
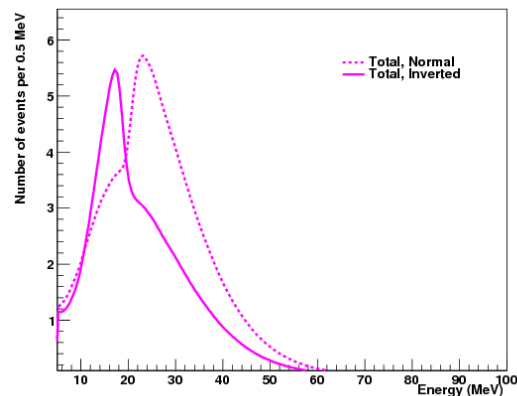
Figure 5–17: Comparison of total event rates for normal and inverted hierarchy, for the Duan flux (a late time slice, not the full flux) in a 17 kt LAr module, in events per 0.5 MeV.

events are required. Figure 5–18 shows examples of observed spectra for normal and inverted hierarchies in one 17 kt LAr module, for statistics near distinguishability. Although this study was done for a single model, we expect multiple signatures of oscillation physics in the full time and spectral structure of the flux.

5.9.3   Supernova Trigger and Background

Electrons from CC ν_e interactions have energies of 10 - 50 MeV and will be easily identified in the detector, as shown in Figure 5–19. Electrons of 10 MeV travel 25mm or about 5 wires in LAr40. The electron direction can be determined by fitting the first few hits on the track. These observations motivate the following simple trigger scheme:

1. Define a cluster to be a hit on 3 or more adjacent wires requiring the drift time difference be less than 1 μs

2. Count the number of clusters in the detector during successive 30 second time periods

3. A trigger occurs if the number of clusters in the most recent time period exceeds the running average of the previous time periods by a significant amount

Tracks will be reconstructed from all cluster hits logged during the time period. Approximately 3,000 neutrino interactions are expected in 30 seconds. The background due to atmospheric neutrino interactions will be non-existent ($\sim 10^{-5}$) in this time period given that 11,000 interactions are expected per year. The background due to cosmic rays is also negligible. The probability that a cosmic ray passes through any TPC drift volume during the 2.3ms drift time
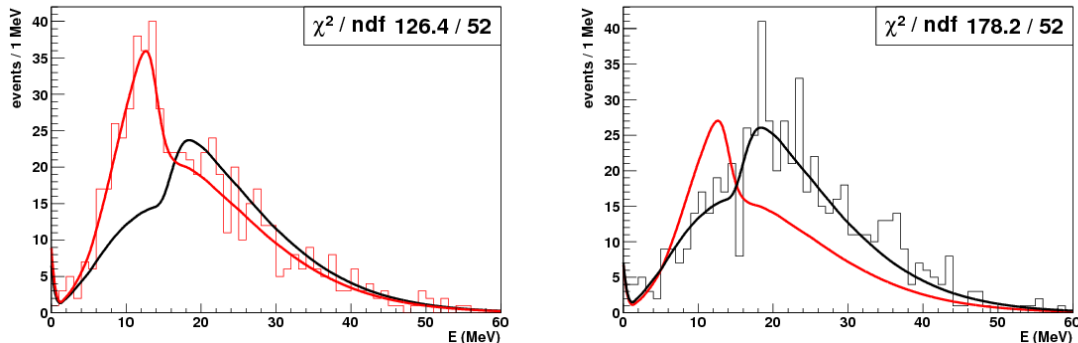
Figure 5–18: Example fits to the expected spectral shapes for normal and inverted hierarchies for the Duan model for one 17 kt LAr module, assuming 630 events observed. Left plot: true hierarchy is inverted. Right plot: true hierarchy is normal. The χ^2/dof is given for the fit to the "wrong" hierarchy.

in which a neutrino interaction occurs is ∼1%. δ-rays produced by cosmic rays would be a potential background but are readily removed using distance and angle cuts to cosmic ray tracks. Backgrounds due to cosmic ray spallation would be at least 4 orders of magnitude lower.

A study of supernova detection prospects in a LAr TPC detector was published in Reference [24]. The conclusions from this report are that the direction measurement accuracy of a supernova at 10 kps is 11° for a 3 kton detector for lepton energies greater than 5 MeV. The pointing accuracy will be much better for LAr40 since it scales like $1/\sqrt{N}$ where N ∼ 3,000.

5.9.4   Conclusions

Sensitivity to physics in a supernova burst is good for any of the possible detector configurations (WC only, LAr only, or the combination of WC and LAr); it improves with larger active mass. We can state with confidence that a combination of different detector types offers the best physics sensitivity, because of ability to distinguish different flavor components of the supernova burst flux.
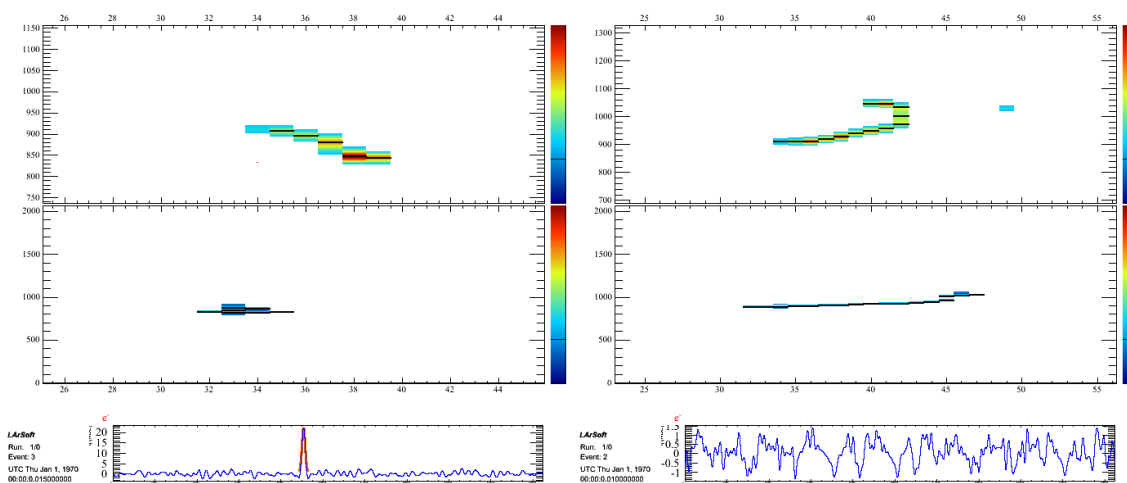
Figure 5–19: Simulated 10 MeV electron (left) in a LAr TPC with 4 mm wire spacing. A single hit was reconstructed on 5 adjacent wires in the collection plane view (top panel). Reconstructed hits appear as a narrow black band. Reconstruction of a simulated 20 MeV electron (right) finds 13 hits on 9 wires. The middle panel shows the induction plane view. The horizontal axis is wire number. The vertical axis is the drift time. The bottom left histogram shows the signal ADC waveform for wire 36 in the collection plane. The reconstructed hit position is found by fitting the ADC distribution in the time region spanned by the red fit curve. The bottom right histogram shows the simulated noise level (rms $\approx$ 1 ADC count) on a channel with no wire hit.

5.10   Additional Physics Capabilities

5.10.1   Atmospheric Neutrinos

The interaction rate for atmospheric neutrinos in LAr40 is expected to be approximately 11,000 per year [26]. With such a sample, it is possible to explore the fine structure of the distribution in energy versus distance through earth traveled. This will permit sensitivity to the neutrino mass hierarchy, provided θ_{13} is not too small. While a larger detector will have better statistics, it is expected that the exceptional event reconstruction capabilities of the LArTPC will lead to resolutions on neutrino energy direction that compensate in part for smaller statistics.

5.10.2   GUT Monopole Searches

Searches for massive, slow moving magnetic monopoles produced in the early universe continue to be of pressing interest. The MACRO experiment [27] has placed the most stringent direct search limits for GUT monopoles with velocities in the range $4 \times 10^{-5} < \beta < 1$, excluding fluxes at the level of $1.4 \times 10^{-16}\,cm^2\,s^{-1}\,sr^{-1}$ (90% C.L.). These limits probe the flux region just beyond that excluded by the existence of the galactic magnetic field (as characterized in variants of the Parker Bound).

Large-area neutrino telescopes in antarctic ice and under water also well-suited for monopole searches, but have best sensitivity for fast monopoles. Studies of data collected with the Amanda-II detector [28] have resulted in limits down to $3.8 \times 10^{-17}\,cm^2\,s^{-1}\,sr^{-1}$ for relativistic monopoles, and the RICE experiment [29] has obtained even more stringent limits for ultra-relativistic monopoles. The current generation of experiments will be able to extend the sensitivity of fast monopole searches.

The LBNE LArTPC Far detector option provides an opportunity to extend the reach for slow monopoles, thanks to excellent timing and ionization measurement capabilities. Quantitative studies of sensitivity have yet to be carried out, but it is likely that the LAr40 detector will exceed the $10,000\,m^2\,sr$ isotropic-flux acceptance of MACRO. It is also expected that NOvA will be able to search for monopoles; the considerably lower cosmic ray muon rate at LBNE may prove advantageous.

Bibliography

[1] M. Bass *et al.*, LBNE Physics Working Group Report, Fall 2010, LBNE-PWG-002, available at: `http://www.int.washington.edu/PROGRAMS/10-2b/LBNEPhysicsReport.pdf`

[2] `http://www.mpi-hd.mpg.de/lin/globes/`

[3] The long-baseline oscillation sensitivities are based on the August 2010 LBNE beam design, LBNE docdb # 2511, `http://www.phy.bnl.gov/~bishai/nwg/fluxes/`.

[4] EURONU WP6 2009 yearly report, J. Bernabeu *et al.*, arXiv:1005.3146 [hep-ph].

[5] P. Vahle, presentation at the XXIV International Conference on Neutrino Physics and Astrophysics (Neutrino 2010) in Athens, Greece; slides available at `http://www.neutrino2010.gr/`.

[6] T. Kobayashi, Neutrino 2010 presentation on the status of T2K.

[7] NOvA technical design report, `http://www-nova.fnal.gov/nova_cd2_review/tdr_oct_23/tdr.htm`

[8] B. Rebel, private communication.

[9] R. Wendell et al. (The Super-Kamiokande Collaboration, Phys. Rev. D 81, 092004 (2010).

[10] K. Abe *et al.*, Phys. Rev. Lett. 97, 171801 (2006).

[11] L. Patrizii presentation at the XIV International Workshop on Neutrino Telescopes, Venice, March 2011, `http://agenda.infn.it/conferenceOtherViews.py?view=standard&confId=3101`

[12] F. Pietropaolo presentation at the XIV International Workshop on Neutrino Telescopes, Venice, March 2011, `http://agenda.infn.it/conferenceOtherViews.py?view=standard&confId=3101`

[13] S. Davidson, C. Pena-Garay, N. Rius, and A. Santamaria, hep-ph/0302093.

[14] M.C. Gonzalez-Garcia, and M. Maltoni, Phys. Rept. 460, 1 (2008), arXiv:0704.1800 [hep-ph].

[15] C. Biggio, M. Blennow, and E. Fernandez-Martinez, arXiv:0907.0097 [hep-ph].

[16] A. Bueno et al., JHEP 0704, 041 (2007) [arXiv:hep-ph/0701101].

[17] R. M. Barnett et al. [Particle Data Group], Phys. Rev. D 54, 1 (1996).

[18] K. Scholberg, arXiv:astro-ph/0701081.

[19] A. Dighe, arXiv:0809.2977 [hep-ph].

[20] T. Totani, K. Sato, H. E. Dalhed and J. R. Wilson, Astrophys. J. 496, 216 (1998) [arXiv:astro-ph/9710203].

[21] J. Gava, J. Kneller, C. Volpe and G. C. McLaughlin, Phys. Rev. Lett. 103, 071101 (2009) [arXiv:0902.0317 [hep-ph]].

[22] H. Duan and A. Friedland, arXiv:1006.2359 [hep-ph].

[23] M. T. Keil, G. G. Raffelt and H. T. Janka, Astrophys. J. 590, 971 (2003) [arXiv:astro-ph/0208035].

[24] "Supernova Neutrino Detection in a Liquid Argon TPC", ICARUS-TM/03-02, February 2008

[25] The LBNE Collaboration, "LBNE Case Study Report: 200kTon Water Cherenkov Far Detector", LBNE docdb # 3495, April 2011.

[26] A. Blake, "Summary of Atmospheric Neutrino Sensitivity Studies," LBNE docdb # 3320, January 2011.

[27] M. Ambrosio et al. (the MACRO Collaboration), Eur. Phys. J. C 25, 511 (2002).

[28] R. Abbasi et al. (the IceCube Collaboration), Eur. Phys. J. C 69, 361 (2010).

[29] D.P. Hogan, D.Z. Besson, J.P. Ralston, I. Kravchenko, and D. Seckel, Phys. Rev. D 78, 075031 (2008).

6 Alternatives: Baseline, Depth and Detector

The reference configuration for LAr40 is a 33-kt fiducial volume detector located at the 800 ft level in the Homestake mine, 1290 km from Fermilab. This chapter considers alternatives, with respect to baseline, depth and detector design/size, and the impact of these choices on physics reach.

6.1   Baseline

LBNE will provide substantial improvements in sensitivity over the current program of long-baseline neutrino oscillation experiments. The longer baseline envisioned for LBNE ($\sim$ 1300 km to Homestake) with respect to NOvA (810 km) is a key factor in achieving this aim: determination of the neutrino mass hierarchy depends strongly on interactions of neutrinos with matter in the earth along their trajectory toward the Far Detector. In turn, the ability to resolve the mass hierarchy ambiguity helps with the determination of θ_{13} and the CP-violating phase δ. Figure 6–1 illustrates the baseline dependence for mass hierarchy (left) and θ_{13} (right). For both the θ_{13} and CP violation sensitivity, the 1290km baseline from Fermilab to Homestake is ideal. For the mass hierarchy, longer baselines are better, however the 1290 baseline still provides a large advantage over, for example, the 800km NOvA baseline. The corresponding sensitivities to CP violation are plotted in Fig. 6–2.

6.2   Depth

Three main options were considered for the depth of LAr40 at Homestake: the 4850L campus, a laboratory on 300L (capitalizing on an existing drive-in access location), and a laboratory on 800L (with new drive-in access capability).

The sensitivity to neutrino oscillation physics is expected to be the same for all three depths, as cosmic ray muons would not pose a significant background for ν_e appearance events. Given the $\sim 10^{-5}$ beam-spill duty factor, timing alone provides effective rejection of CR muons,
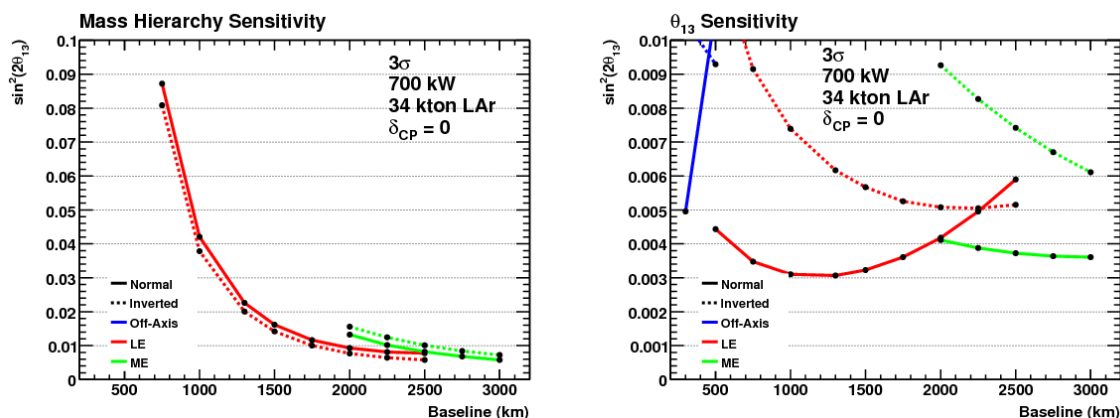
Figure 6–1: Sensitivity of LBNE to neutrino mass hierarchy (left) and θ_{13} (right) with the LAr40 Far Detector, as a function of baseline for on-axis "low" (red) and "medium" energy (green) beam configurations, as well as for an off-axis beam (blue).

even at 300L where the CR rate is ~ 800 Hz in one LAr TPC module. In addition, CR muons are dominantly down-going, fully penetrating the detector: these events can be clearly identified in most cases. Finally, even with a readout spanning 3ms – more than the maximum ionization electron drift time, the rate of overlap of signals from CR muons with those from beam-induced neutrino interactions will be negligible, since the CR rate in a single APA is only a few Hz at 300L.

For proton decay searches, the 4850L campus is well-shielded from CR muons. At the 800L location, a 21-kt (active volume) detector with a veto system, has a fiducial volume of 14 kt for proton decay, described in Sec. 5.8. The level of background at 300L will be significantly worse than at this location as described in [1]. Combining the cost difference to construct at 4850L, the ample capabilities for proton decay at 800L, and the less substantial cost increase to house the detector at 800L vs 300L, in 2010 the collaboration chose a Reference design for the detector housed at 800L.

It has recently been suggested that the cost of the 4850L option could be reduced significantly by upgrading the existing access shafts instead of sinking two new shafts to the LAr cavern as originally proposed. The loss of having an independent ventilation system at the 4850L would be compensated for by placing the cavern at the most downstream end of the air path on the 4850L and closest to the air exhaust shaft (the Oro Hondo). We have found that the ventilation requirements (flow rate and reliability) for the worst-case fire accident are compatible with the requirements for cryogenic safety. A second reason for re-considering the deep option is that the cost difference for selecting the shallow site assumed that a veto system would be required for one 17-kton module. The cost of the veto system for LAr40 is more than twice the original cost estimate. Underground excavation engineering is currently underway for both depth options. The revised 4850L cost estimate will be available in early November 2011 and a decision will be made with this new information.
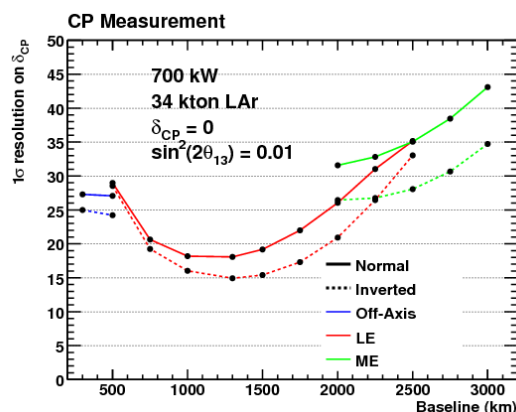
Figure 6–2: Sensitivity of LBNE to neutrino the CP-violating phase δ with the LAr40 Far Detector, as a function of baseline for on-axis "low" (red) and "medium" energy (green) beam configurations, as well as for an off-axis beam (blue).

6.3　Detector Reference Design Options

The LBNE project has costed three options for the LAr far detector. At the low end of the cost range is a 24-kt fiducial volume LAr TPC with 3.75m drift length, 3 wire planes, and 5mm wire pitch. The mid-range version has the same drift range and wire plane parameters but a larger overall fiducial volume of 33-kt. At the high end of the cost range is a 34-kt fiducial volume option with 2.5m drift, 3 wire planes, and 3mm wire spacing. The mid-range version is the the reference design option described in this Case Study document.

The difference between the low and mid-range options is only in overall fiducial mass. The primary differences which impact physics performance between the mid and high-range options are the drift distance and wire spacing.

The high-range option includes an additional LAr storage tank, to be located on the surface, that would shorten the schedule by ∼9 months.

The decreased drift distance at the high end ensures that the purity achievable with MicroBooNE's 2.5m drift is all that is needed here. The smaller wire pitch potentially allows for better spatial resolution which could help in differentiating signal from background for beam and non-beam physics in particular for low energy events.

Over the course of developing the conceptual design for LAr40, a free-standing cryostat constructed in the form of an array of internally supported TPC cells was considered in addition to the membrane cryostat described in this report. The membrane cryostat was selected for the reference design because of the strong record of construction and operation of such storage vessels in industry, and because initial studies indicate it would be less costly to build than the internally supported vessel. The ability to pull a hard vacuum in a membrane cryostat has now

been demonstrated, eliminating the rationale for maintaining the free-standing cryostat as an option.

6.4 Modularity and Scalability

LAr40's design makes use of modularized detection systems in as many ways as possible. This enables ease of scalability of this design both for LBNE and for possible upgrades beyond LBNE. The ways in which the detector design is modularized are the following:

- LAr40 is separated into two modules. With a phased construction, this leaves one not yet instrumented module free to hold the LAr in the case that the instrumented module must be emptied to correct a problem.

- The APAs and CPAs in LAr40 are 2.5m x 7m in size. They can be constructed above ground and hung into place below ground for ease of assembly and installation. Each module could be lengthened by simply hanging more APAs and CPAs if it was cost-effective to increase the detector mass of each module.

- If it is shown that purity can be achieved and maintained such that the drift distance can increase, the detector design can be easily adapted by increasing the distance between the APAs and CPAs and reducing the overall number of drift regions to accommodate.

The modular design features of LAr40 allow for ease of assembly underground, ability to modify detector design parameters easily, and ease of adding more detector mass by constructing new modules, as upgrades to LBNE in the future.

We have considered constructing more modules of smaller size. There is clearly great benefit to having two modules but the benefits of having more than two is not compelling. The cost would also be higher since cryostat construction and cryogenics operating costs scale by the combined surface area of all cryostats.

Bibliography

[1] A. Bueno et al., JHEP 0704, 041 (2007) [arXiv:hep-ph/0701101].

7 Detector Development Program

7.1 Introduction

This section of our case study describes the development program designed to ensure a successful and cost-effective construction and operation of the massive liquid argon TPC detectors proposed for the LBNE program and to investigate possibilities for enhancing the performance of the detector. The program for developing the reconstruction and analysis software, which we see as an equally important and critical component of a successful experiment, is described in Chapter 5. The feasibility of the LArTPC as a detector has been demonstrated most impressively by the current state of the ICARUS experiment currently taking data at Gran Sasso.

It is understood that for succesfull operation a LArTPC has stringent requirements on

- argon Purity which must be of order 200 ppt O_2 equivalent or better,

- the time projection chamber and field cage which must be extremely robust against wire-breakage and accept a cool-down of over 200K, and

- the front-end electronics which must achieve a noise level ENC of 1000e or better.

Within the LBNE collaboration, proponents of the LArTPC approach are developing a detailed design for detector modules of mass ~20 kilotons. The Reference design has instrumented TPC "ladders" hung inside a large "membrane style " cryostat, a technology now commonly in use for liquefied natural gas (LNG) transport ships and dozens of in-ground LNG storage facilities. It is not intended to evacuate the cryostat (although this is feasible at modest ~$10M cost); the insulation is provided by a 1m layer of polyurethane foam surrounding the membrane. The readout of signals from the TPC is accomplished with CMOS-based electronics immersed in the liquid argon. As well as improving the S/N by removing the capacitance of the cable from wire to amplifier, in-liquid electronics relax the constraint on the TPC geometry that all the wires have to be brought to the top and allow for multiplexing the data thus reducing the cable plant which is the major source of contamination.

The design of the LBNE LArTPC has evolved significantly from earlier concepts based on standard above ground upright cylindrical LNG storage tanks which envisioned single TPC sense and high-voltage planes spanning the full-width of the tank - essentially a direct scaling of previous detectors. Problems with the actual construction of such massive planes and with the logistics of being able to construct the TPC only after the cryostat was complete are avoided in the present design. In the present scheme, TPC 'panels' are fully assembled and tested - including the electronics - independent of the cryostat construction. This modular approach is a key feature of the design. It has the benefit not only of improving the logistics of detector construction but it makes the individual components of manageable size. It should also be noted that the cryostat itself is formed of modular panels designed for quick and convenient assembly.

7.2   Components of the Development Program

Programs of ongoing and planned development to allow the construction of massive LArTPC's in the U.S. have been developed and described in [4] and in the LBNE CDR. To advance the technology to the detectors proposed for LBNE, the U.S. program has three aspects:

- the demonstration that the U.S program can reproduce the essential elements of the existing technology of the ICARUS program.

- a program of development on individual elements to improve the technology and/or make it more cost effective.

- a program of development on how to apply the technology to a detector module.

A summary of the items in the program is given in the following tables. Table 7–1 lists the on-project activities described in this chapter, a short description of the information needed and the LBNE milestone when the information is required. Table 7–2 lists off-project activities, the aspect of these activities that is applicable to LAr40 and the LBNE milestone at which the information is required. These aspects will be described in more detail in the following sections. As will be explained below, these are not R&D activities but preliminary engineering design.

7.3   Scope and Status of individual components

7.3.1   Materials Test System

An area for liquid argon development, shown in Figure 7–1 has been established in the Proton Assembly Building at Fermilab. The Materials Test System has been developed to determine the effect on electron drift-lifetime of materials and components that are candidates for part of

Activity	LAr40 Information	Need by
In-liquid Electronics	Low noise readout, long lifetime	LAr1 construction
TPC Construction	Mechanical design	LAr1 construction
33 ton Prototype	Cryostat construction	LAr1 cryostat procurement
LAr1	detector integration	LBNE CD-2

Table 7–1: On-Project Activities

Activity	LAr40 Applicability	Status	Need by
Yale TPC	None	Completed	NA
Materials Test System	Define requirements	Completed	NA
	Materials testing	Operating	As Req'd
Electronics Test Stand	Electronics testing	Operating	As Req'd
LAPD	Purity w/o evac.	Early 2012	LBNE CD-2
	Convective flow	Early 2012	LBNE CD-2
Scintillator Development	Photon Det. Definition	Completed	LAr1 Construction
	Industrialization	Not started	LBNE CD-3
ArgoNeuT	Analysis tools	On-going	LBNE CD-2
MicroBooNE	Electronics tests	Construction	LBNE CD-3
	DAQ algorithms	In development	LBNE CD-3
	Analysis tools	In development	LBNE CD-2
	Lessons learned	Not started	LBNE CD-3

Table 7–2: Off-Project Activities

Figure 7–1: Liquid Argon Area at PAB

the LArTPC detector. The system consists in essence of a source of clean argon (< 30 ppt O_2 equivalent), a cryostat, a sample chamber which can be purged or evacuated, a mechanism for transferring a sample from the sample chamber into the cryostat, a mechanism for setting the sample height in the cryostat so that it can be either in the liquid or in the gas ullage above the liquid, a temperature probe to measure the temperature of the sample, and an electron life-time monitor. The system is fully automated and the life-time data are stored in a single data-base with the state of the cryogenic system. The source argon filters are home-made and are regenerated in place. A noteworthy feature is the novel bubble-pump filter inside the cryostat. This can filter the cryostat volume in a few hours thus allowing us to continue studies after the argon has been contaminated without having to refill. A schematic of the MTS is shown in Figure 7–2.

The major conclusions of our studies to date are given in [1] and are summarized here. We have found no material that affects the electron drift-lifetime when the material is immersed in liquid argon - this includes, for example, the common G-10 substitute, FR-4. On the other hand materials in the ullage can contaminate the liquid - this contamination is dominated by the water the materials outgas and as a result are strongly temperature dependent. Any convection currents that transport water-laden argon into the liquid and any cold surfaces on which water-laden Argon can condense will fall into the liquid and reduce the electron lifetime. Conversely, a steady flow of gaseous argon of a few ft/hr away from the liquid prevents any material in the gas volume from contaminating the liquid.

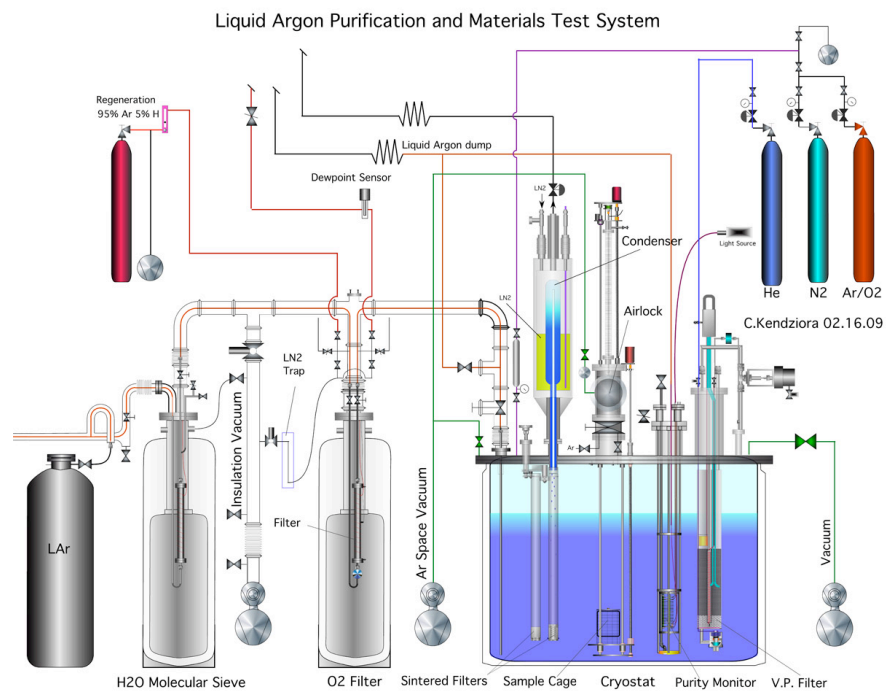These results are taken into account in the design of both MicroBooNE and LAr40. For

Figure 7–2: Schematic of the Materials Test System Cryostat

LBNE they have been cast as detector requirements. The MTS will continue to be used by MicroBooNE and LBNE to test detector materials such as cables that will reside in the ullage.

7.3.2 Electronics Test Stand

The Electronics Test Stand is also installed in the Proton Assembly Building at Fermilab. It consists of a cryostat, served by the same argon source as the Materials Test System, and a TPC with a 50 cm vertical drift terminating in three planes of 50 wires each, arranged at 120 degrees. Figure 7–3 shows the TPC being inserted into the cryostat. Two sets of small scintillation counters outside the cryostat are used to trigger the system on cosmic rays. The data from this system provide a crucial check of simulations of the electron drift and the signals induced on the wires.

The front-end electronics and the crucial shaping filters for the ArgoNeuT experiment were developed on this system from the sort of data shown in Figure 7–4. These data also led to the development of the FFT technique for reconstructing track hits. A hybrid pre-amplifier has been successfully tested in liquid and has demonstrated excellent noise performance.

The ASIC front-end amplifiers for LBNE will also be tested, providing assurance that bench measurements are reproducible in a functional TPC.

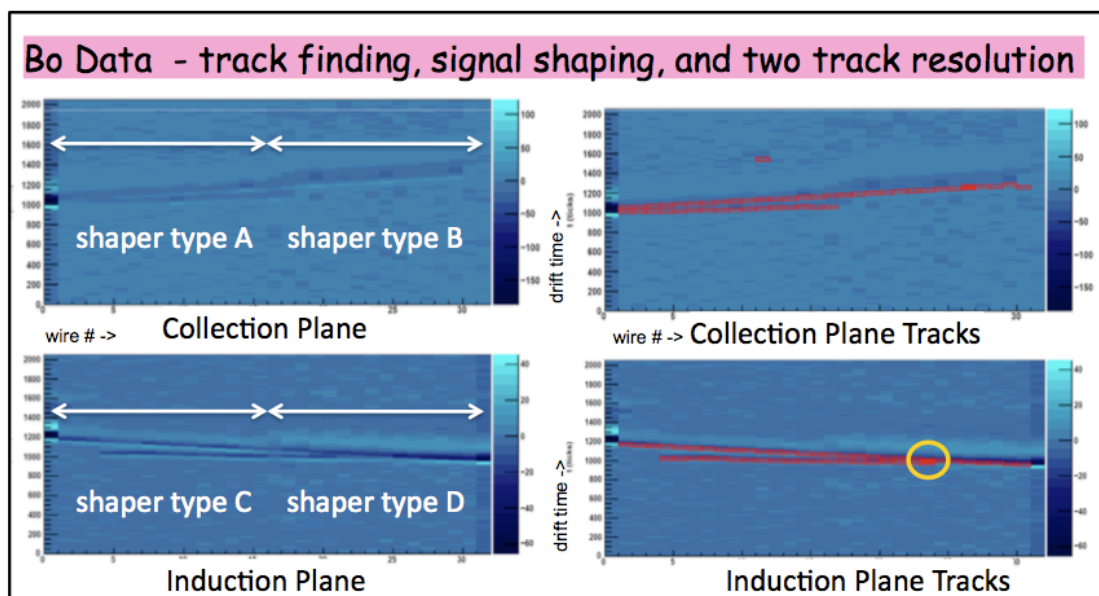Figure 7–3: Electronics Test TPC insertion into cryostat, Bo

Figure 7–4: A cosmic ray with a delta electron as seen in the Electronics Test Stand TPC. Note the different width of the shaded portions along the tracks in the left panels. These are due to the two shaping circuits being tested. The readout scheme for MicroBooNE and LBNE uses digital signal processing and has minimal filtering before the ADC.

7.3.3   Liquid Argon Purity Demonstration, LAPD

The LAPD is a significant scale (30 tons) system which contains a vessel to be filled with liquid argon with purity adequate for a LArTPC without evacuation. While large cryogenic systems have been built by US groups, it is also the first significant size cryogenic and purification system for a LArTPC to be built in the U.S., and as such is providing valuable experience and data for the construction of future systems. Figure 7–5 shows the filtration system and the LAPD tank.

The tank is instrumented with a system of sniffers to measure the oxygen concentration at 6 heights during the gas-purge, a system of temperature monitors which can be lowered and raised inside the tank to measure temperature gradients, an ICARUS style purity monitor in the input line to the tank, and four ICARUS style purity monitors to measure electron drift-lifetime within the tank. Analytic instrumentation includes a water meter and an oxygen meter both with ppb sensitivity, and a nitrogen meter with 10 ppb sensitivity installed to be able to take measurements throughout the system. The scheme for going from atmosphere to clean liquid involves a gas purge with argon, gas recirculation with purification, a liquid fill while venting, to drive out any contaminants remaining in the gas, followed by liquid recirculation through the purification system.

The primary motivation is to demonstrate an electron drift-lifetime of several milliseconds. If this is achieved, the effect of varying the conditions (gas and/or liquid recirculation, different recirculation rates, no recirculation) will be investigated. The size of this tank also allows us to use the measurements from the temperature monitor system to check the accuracy of the ANSYS simulations of temperatures within the tank. This will check the simulations and confirm the small temperature gradients and consequently low velocities of the convection flows predicted in large LArTPCs.

Once these tests have been performed the tank will be emptied and a second phase of studies will begin. A 2m long drift version of the TPC shown in Figure 7–3 will be installed in the LAPD tank. The TPC will be read out using cold electronics. The LAr purity tests will be repeated and the results compared with the first phase. The second phase of studies will be completed in early March 2012. At this time, LAPD management and operations will be transferred to LBNE to support the 33 ton membrane cryostat prototype described below.

LAPD began purging with argon gas on September 23, 2011. As of this writing, nine volume changes of argon gas have been flushed through the tank and the atmosphere inside contains <1ppm of water and a few ppm of oxygen.

As described in section 3.5, the achievement of good LAr purity without evacuation in LAPD is a desirable, but not prerequisite, outcome for LAr40 since vacuum pumping of the LAr40 membrane cryostat is feasible. Confirmation of the computational fluid dynamics modeling in ANSYS is also not a prerequisite, but would indicate that further analysis may be necessary

Figure 7–5: Liquid Argon Purity Demonstration Filtration and Tank

if the simulations and measurements disagree.

7.3.4   Photon Detection R&D

The R&D program for Photon Detection is based on a promising new, cost-effective scheme for light collection in LArTPCs as described in [2]. The design is based upon light-guides fabricated from extruded or cast acrylic and coated with a wavelength shifter doped skin. Multiple acrylic bars are then bent to guide light adiabatically to a single cryogenic PMT. Prototypes of the basic detector elements have been shown to perform well [2]. These lightguides have a thinner profile than the usual TPB-coated PMT based system, occupying less space in an an LAr vessel and resulting in more fiducial volume. Another advantage of this system is that the bars are inexpensive to produce. The most convenient place for the paddles is between the wire planes that wrap around the APAs.

Lightguide R&D has advanced rapidly since the initial publication resulting in ∼3x higher light yields [3]. The R&D is now advanced sufficiently to provide a technical basis for the LAr40 reference design. On-going design efforts at MIT, Indiana University, and Fermilab are directed to industrial scale production and the evaluation of lower cost fluors that are effective in converting VUV photons. The goal is to extrude acrylic bars along with a co-extruded layer of TPB doped acrylic. This work is being done at Dr. Anna Pla-Dalmau's extrusion facility at Fermilab. This group is also investigating PMTs with increased quantum efficiency, as well as other efficient light collection technologies, such as silicon photomultipliers.

7.3.5   TPC Design

The design for LBNE has adopted the basic ICARUS multi-plane single-phase TPC concept and has incorporated new features suitable for a very large detector. The main emphasis of the development program is to develop a TPC design that is highly modular, low cost, robust and easily installed inside a finished cryostat.

A significant effort has been focused on minimizing the dead space between detector modules to improve the fiducial vs. total LAr volume ratio. The APA reference design accomplishes this goal but requires making ∼2M high quality wire terminations. The wire termination scheme used by ICARUS has been proven to be very reliable but it is too labor intensive to fabricate for a million channel detector system. We have adopted the wire-solder + wire-epoxy termination scheme that has been used for decades on drift chambers and proportional wire chambers to mount Cu-Be wires. The termination scheme was used to terminate 2.5M anode wires in the CMS end cap muon system. Cu-Be wires have excellent mechanical properties and the advantage of low resistance compared to stainless steel. A study is currently underway within the LAr40 project to identify the optimum wire bonding parameters. The focus is currently on finding a

commercial epoxy that provides the best qualities of bond strength, cure time and low temperature operation.

7.3.6   Electronics Development

The work to date on cold electronics has established that there are no show-stoppers. The remaining activities outlined here concerns optimization of performance of the CMOS ASICs, the evaluation of several widely available CMOS technologies, and the development of readout architectures appropriate and timely for various scenarios of very large detector development.

7.3.6.1   CMOS transistors: lifetime verification and technology evaluation

The results of the design of the CMOS electronics for operation at LAr temperature (89K), performed so far by the MicroBooNE and LBNE collaborations, as well as by a large collaboration led by Georgia Inst. of Technology, are summarized in Section 3.7.

Briefly, the fundamentals are: charge carrier mobility in silicon increases at 89K, thermal fluctuations decrease with kT/e, resulting in a higher gain (transconductance/current ratio $= g_m/i$), higher speed and lower noise. For a given drain current density the same degree of impact ionization (measured by the transistor substrate current) occurs at a somewhat lower drain-source voltage at 89K than at 300K. The charge trapped in the gate oxide and its interface with the channel causes degradation in the transconductance (gain) of the transistor and a threshold shift. The former is of major consequence as it limits the effective lifetime of the device (defined in industry and the literature as 10% degradation in transconductance). Thus an MOS transistor has equal lifetime due to impact ionization at 89K and at 300K at different drain-source voltages. This is illustrated in Figure 7–6. This feature offers a tool for accelerated lifetime testing by stressing the transistor with both increased current and increased voltage, and monitoring the substrate current and the change in g_m due to impact ionization. In these conditions, the lifetime can be reduced arbitrarily by many orders of magnitude, and the limiting operating conditions for a lifetime in excess of 20 years can be determined. With this foundation, more conservative design rules (lower current densities and voltages) can be derived and applied in the ASIC design, as has been done for the ASIC described in Section 3. The goal of this part of the program is to verify by accelerated testing the expected lifetimes for the several widely available CMOS technologies under consideration (TSMC, IBM, AMS). It should be noted that this is a standard test method used by the semiconductor industry. These methods are used to qualify electronics for deep space NASA missions as well as commerical PCs.
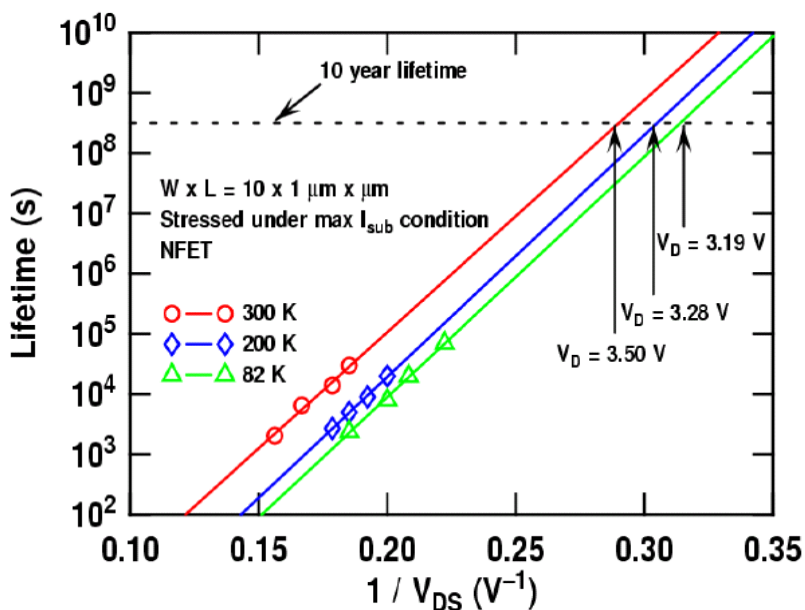
Figure 7–6: Lifetime at different temperatures vs V_{DS}

7.3.6.2   Readout architectures, multiplexing and redundancy

A high degree of multiplexing after digitization of signals is essential for a TPC with 0.5 million wires, in order to reduce the cable plant and the attendant outgassing. Just how high a multiplexing factor should be chosen is a matter of study, considering the risk of losing one output data link. A part of the program will include system designs with redundant links and redundant final multiplexing stages to minimize the risk of losing the data from a significant fraction of the TPC (note that even with a multiplexing factor of 1/1024 and no redundancy, one failed link would result in a loss of 0.2%). The link technology (copper wire vs optical) will be studied in the context of the detector site depth. Near the surface, optical links will be needed (assuming a high degree of multiplexing) for the higher data rates due to cosmic muons. At the 800L, copper links would be sufficient and the choice can be made based on other considerations.

7.3.7   Cryostat Development - 33 ton Prototype

In principle, a thin-walled membrane cryostat is as suitable as a thick-walled cryostat for use with high purity LAr. Both would be constructed with 304 stainless steel with a polished surface finish. Both would use passive insulation. The total length of interior welds required for construction would be similar in both cases. The leak checking procedure would be the same in both cases. Two membrane cryostat vendors are being considered. GTT supplies SS membranes

1.2mm thick x 1m x 3m. A second vendor, IHI in Japan, supplies SS membranes 2mm thick x 3m x 8m. The significant difference between membrane cryostats and thick-walled cryostats is the depth of the welds used to construct the vessel. The majority of membrane welds are completed in one or two passes with automatic welding machines. A second difference, and a major advantage, is that the membrane cryostat is a standard industrial design that has been in use for over 40 years. A thick-walled cryostat vessel would be custom designed and would require significant engineering and testing. A third difference, and another major advantage, is the ability to purge the membrane cryostat insulation space with argon gas so that a leak cannot affect the purity if it escapes detection and repair. The use of two detector cryostats further mitigates this concern as described in section 3.10.

A 3m x 3m wall panel shown in Figure 7–7 was constructed at Fermilab using materials and technical guidance from GTT. The labor hours used in construction are consistent with the vendor estimates. The wall panel was leak tested (none were found) and vacuum tests were performed on the insulation system. We found that the insulation system is designed to allow vacuum pumping of the main cryostat volume to a hard vacuum. This result demonstrates that vacuum pumping of a membrane cryostat is feasible, if it is found to be required. No modifications to the vendor supplied components are required to accomplish this.

The next step in the cryostat prototype program is intended to address project-related issues: 1) to gain detailed construction experience, 2) to develop the procurement and contracting model for LAr40 and 3) to incorporate the design and approval mechanism in the Fermilab ES&H manual. (Membrane cryostats are designed in accordance with European and Japanese standards.)

At present, we are in the process of procuring the cryostat components for a 33 ton membrane cryostat from IHI. This is similar in size to the LAPD cryostat and will use much of the cryogenic equipment, purification equipment and instrumentation from LAPD. Cryostat construction will occur in Spring 2012 and the prototype will operate in September 2012. We will also investigate the use of an internal liquid circulation pump as provisionally planned for LAr40. Figure 7–8 shows a drawing of the 33 ton prototype sitting next to LAPD.

7.3.8   1 kt Engineering Prototype - LAr1

The last major project of the development program is the construction of a 1 kt cryostat to be equipped with proposed TPC and electronics - LAr1. This prototype will serve to incorporate and test all the major components of LAr40:

- Gain further experience in cryostat construction and procurement

- Exercise the assembly and testing procedures for all the individual components,

Assembly of first membrane panel showing: delivery crate, (from Korea to Fermilab), insulation backing, weld between two overlapping panes, and 3 panel section ready for leak testing.

Figure 7–7: Membrane panel assembly and components
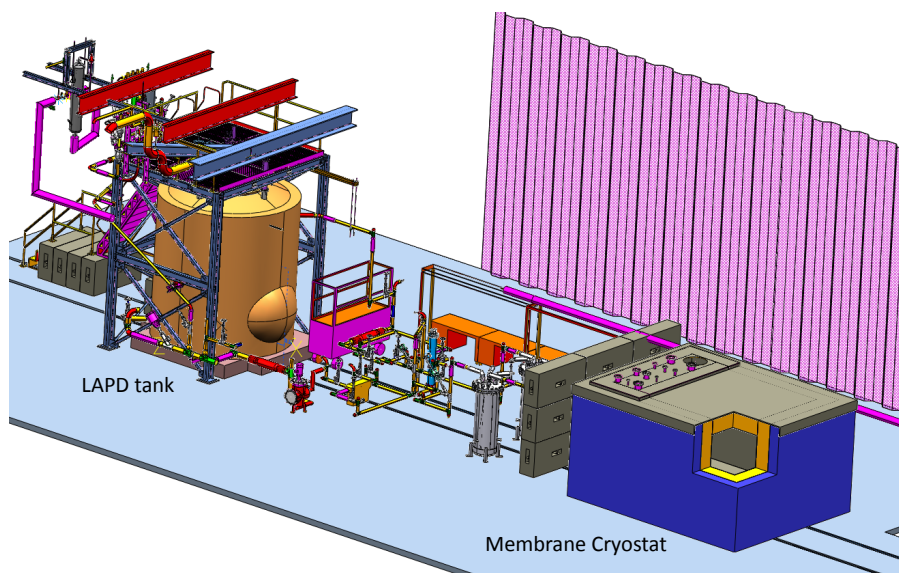

LAPD tank

Membrane Cryostat

Figure 7–8: 33 ton Membrane Cryostat in PC4

- Test the integration features of the detector design including:

    the TPC supports,

    the cold electronics, signal feedthroughs and power feedthroughs,

    the grounding scheme and control of electrical noise,

    the purification system,

    the cryogenic system and the cryogenic control system

- Exercise the installation procedure.

The means of demonstrating that these goals have been met is by acquiring and reconstructing a sample of through-going cosmic rays. Figure 7–9 shows the LAr1 cryostat in the pit of the DZero building. LAr1 is being managed as a semi-independent sub-project. The sub-project was subjected to a CD-1 style technical, cost, schedule and management review in August 2011. The sub-project presented a technically driven schedule since there is currently a significant funding uncertainty. LAr1 construction could be completed in early 2014 in this admittedly optimistic scenario in which both funding and resources are available when needed.

An attractive extension of the LAr1 goals would be to measure the cosmic ray spallation backgrounds rates expected in LAr40. A sample of cosmic ray spallation interactions in the LAr1 volume could be acquired in a relatively short period of time. Charged kaons associated with the interaction could be identified and their momentum measured. Charged K's produced by K^o charge exchange could also be identified and their rate and angular distribution measured. These measurements would then be applied to refine the design of the LAr40 veto system.

A second speculative extension would be to acquire a sample of atmospheric neutrinos. For example, 100 - 200 atmospheric neutrinos would interact in LAr1 if it operated for one year with 100% efficiency. Extracting these events from a 5 kHz background rate of cosmic rays would be extremely challenging however.

7.3.9   Physics Experiments with associated detector development goals

Two projects, ArgoNeuT and MicroBooNE, which are physics experiments in their own right, are also contributing to the development of the LBNE experiment. Their most important role is in providing data and motivation for the development of event reconstruction and indentification software.

7.3.9.1   ArgoNeuT - T962

The Argon Neutrino Test is a 175 liter LArTPC which completed a run in the NuMI neutrino beam (see http://t962.fnal.gov). The 0.5m x 0.5m x 1m TPC was positioned directly
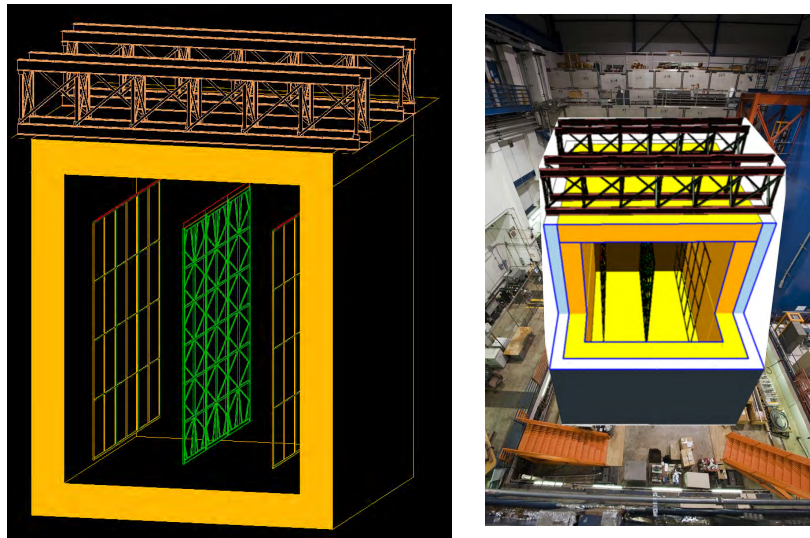
Figure 7–9: Schematic of the LAr1 detector and a cartoon of its setting in the DZero pit.

upstream of the MINOS near detector; which served as a muon catcher for neutrino interactions occurring in ArgoNeuT. ArgoNeuT began collecting data using the NuMI anti-muon neutrino beam in October 2009 and ran until March 1, 2010. ArgoNeuT's ~10k events motivate the development of analysis tools, and are the basis for the first measurements of neutrino cross sections on argon. An event with two π^0 decays is shown in Figure 7–10. ArgoNeuT was also the first LArTPC to be exposed to a low energy neutrino beam and only the 2nd worldwide to observe beam neutrino interactions. The ArgoNeuT collaboration is currently preparing 1) a NIM paper that documents the detector performance using NuMI beam muons and 2) the first physics paper on muon neutrino charged current differential cross sections on argon.

A deconvolution scheme using a FFT has been applied to the ArgoNeuT data. This procedure eliminates a problem with the ArgoNeuT electronics (which were DZero spares and could not be modified for ArgoNeuT). Another more significant benefit of deconvolution is that bi-polar induction plane signals can be transformed into uni-polar collection plane signals. An example of this is shown in Figure 7–11. A selection of figures from the draft NIM paper are reproduced below.

The applicability to ArgoNeuT is that it provides a set of data in the same range of energy for the LBNE neutrino beam, enabling the development of analysis algorithms that can be utilized for LAr40 physics analysis with little or no modification.
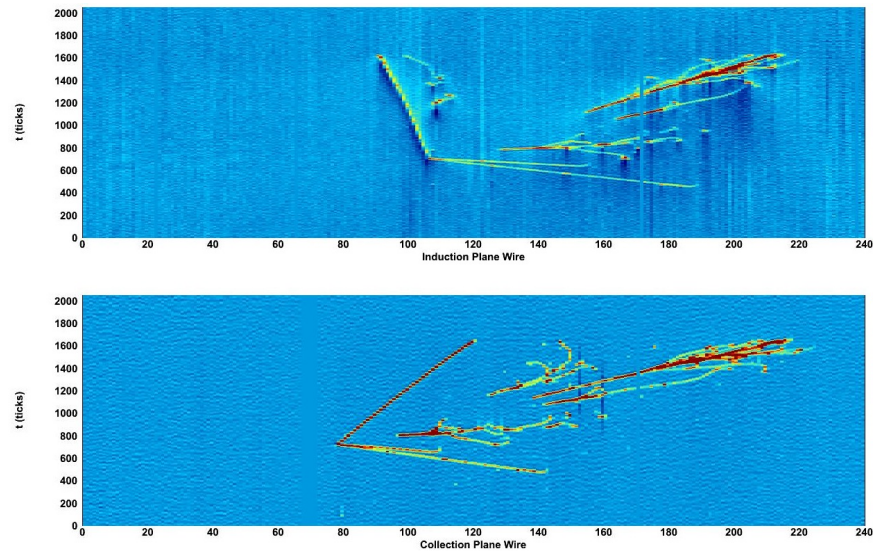
Figure 7–10: A neutrino event with 4 photon conversions in the ArgoNeuT detector. The top (bottom) panel shows data from the induction (collection) plane after deconvolution.
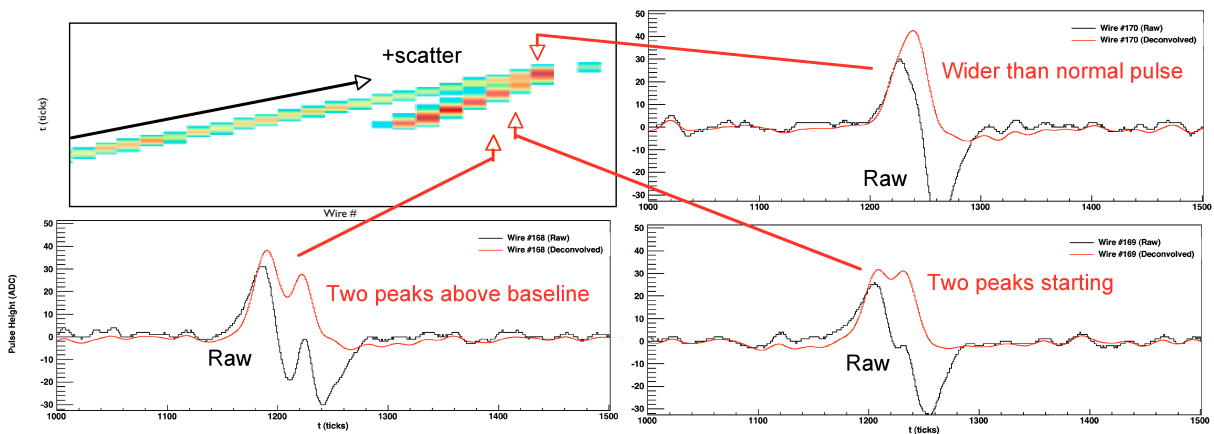

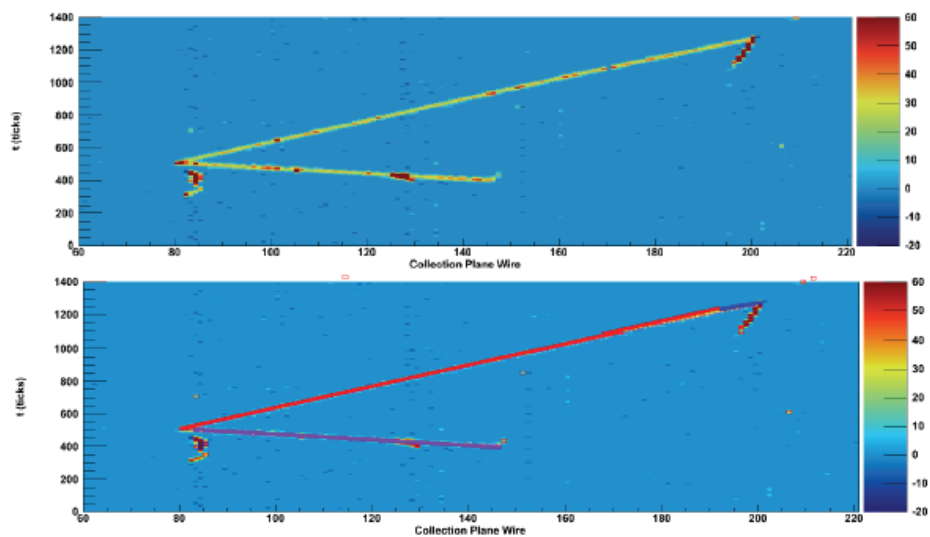Figure 7–11: Figure from the ArgoNeuT draft NIM paper.

Figure 6: (Top) A neutrino candidate in ArgoNeuT as seen on the collection plane. (Bottom) The Hough lines found with the line-finding algorithm overlaid on the particle tracks.
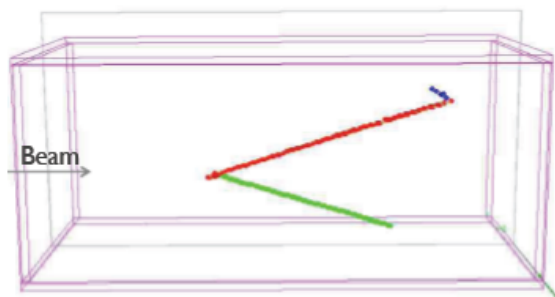

Figure 7: The neutrino event shown in Figure 6 reconstructed in three dimensions.

Figure 7–12: Figure from the ArgoNeuT draft NIM paper showing the status of 3D reconstruction.
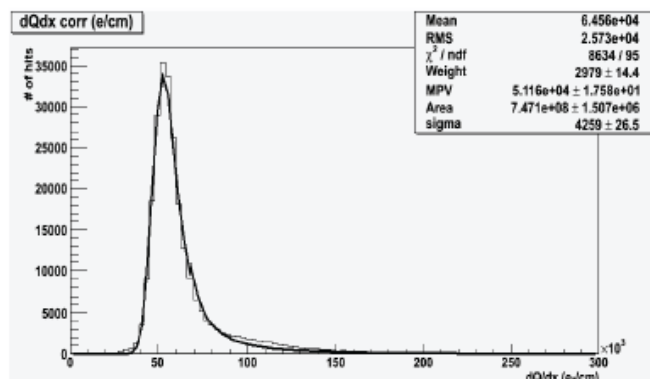
Figure 13: dQ_0/dx distribution (in ADC/cm) obtained for the through-going muon data sample having corrected for the electron lifetime and quenching effect on the ionization charge and properly taken into account the contribution due to δ-rays, as reported in the previous Section. A Landau-Gaussian fit is also reported.

Figure 7–13: Figure from the ArgoNeuT draft NIM paper showing the status of calorimetric reconstruction.

7.3.9.2   MicroBooNE E-974

The MicroBooNE experiment is a 86 ton active mass LArTPC, (170 ton argon mass) in the construction phase. It has both a physics program and LArTPC Development goals. Micro-BooNE received stage 1 approval from the Fermilab director in 2008 and partial funding through an NSF MRI in 2008 and an NSF proposal in 2009. MicroBooNE received DOE CD-0 Mission need in 2009 and CD-1 in 2010 and successfully passed the CD-2/3a review in August 2011. It plans to start running in early 2014.

As well as pursuing its own physics program, MicroBooNE will collect a large sample (∼ 100k) of low energy neutrino events which will serve as a library for the understanding of neutrino interactions in liquid argon. Because MicroBooNE is at the surface, it will also have a large sample of cosmic rays with which it can study potential backgrounds to rare physics. The process of designing MicroBooNE has naturally stimulated several developments helpful to the LBNE program. Studies of wire material, comparing Be-Cu with gold-plated stainless steel in terms of their electrical and mechanical properties at room and liquid argon temperatures, and techniques for wire tension measurement are immediately relevant. Expertise has been developed generating simulations of electrostatic drift-fields as well as simulations of temperature and flow distributions in liquid argon cryostats which is being applied to the LBNE TPC and cryostat. MicroBooNE will use the front-end of the proposed in-liquid electronics as the wire-signal amplifiers and the DAQ developed for MicroBooNE will exploit compression and data reduction techniques to record data with 100% livetime.

In summary, MicroBooNE's LArTPC development goals that are pertinent to LAr40 are

- large scale testing of LBNE front end electronics; similar in scale to LAr1,

- test continuous data acquisition algorithms,

- refine the analysis tools developed in ArgoNeuT, and

- provide costing and construction lessons-learned.

7.4 Summary

Impressive progress has been made in the development of LAr TPC technology over the last few years. All elements of the development program have completed the R&D phase. Credible conceptual designs exist for all systems in LAr40. The technical activities described in this chapter are properly characterized as preliminary engineering design.

The most significant deficiency is the lack of fully automated event reconstruction. Algorithms have been developed within the LAr community and are being successfully applied to ArgoNeuT data as well as simulated MicroBooNE data. The algorithms have individually shown that the high efficiency and excellent background rejection capabilities of a LAr TPC are achievable. The task ahead is to combine them into a single package.

Bibliography

[1] Andrews, R. et al. "A system to test the effects of materials on the electron drift lifetime in liquid argon and observations on the effect of water." *Nuclear Inst. and Methods in Physics Research, A* , 608:251-258, 2009.

[2] Bugel, L.. et al., "Demonstration of a Lightguide Detector for Liquid Argon TPCs", *Nuclear Inst. and Methods in Physics Research, A* , in press (2011).

[3] Janet Conrad, private communication

[4] Baller, B., Fleming, B. eds "Integrated Plan for LArTPC neutrino detectors in the US." Fermilab FN-0917-E